FACULTY OF ENGINEERING
AND ARCHITECTURE

Highly Efficient, Ultra-Wideband, Air-Filled Substrate-Integrated-Waveguide Antenna Technology for Next-Generation Wireless Systems

Quinten Van den Brande

Doctoral dissertation submitted to obtain the academic degree of
Doctor of Electrical Engineering

Supervisors

Prof. Hendrik Rogier, PhD - Prof. Sam Lemey, PhD

Department of Information Technology
Faculty of Engineering and Architecture, Ghent University

October 2021

GHENT
UNIVERSITY

FACULTY OF ENGINEERING AND ARCHITECTURE

Highly Efficient, Ultra-Wideband, Air-Filled Substrate-Integrated-Waveguide Antenna Technology for Next-Generation Wireless Systems

Quinten Van den Brande

Doctoral dissertation submitted to obtain the academic degree of
Doctor of Electrical Engineering

Supervisors
Prof. Hendrik Rogier, PhD - Prof. Sam Lemey, PhD

Department of Information Technology
Faculty of Engineering and Architecture, Ghent University

October 2021

GHENT UNIVERSITY

ISBN 978-94-6355-527-2
NUR 959
Wettelijk depot: D/2021/10.500/75

Members of the Examination Board

Chair

Prof. Em. Daniël De Zutter, PhD, Ghent University

Other members entitled to vote

Prof. Guillaume Ducournau, PhD, Université de Lille, France
Prof. Anthony Ghiotto, PhD, Bordeaux INP, France
Prof. Günther Roelkens, PhD, Ghent University
Prof. Patrick Van Torre, PhD, Ghent University

Supervisors

Prof. Hendrik Rogier, PhD, Ghent University
Prof. Sam Lemey, PhD, Ghent University

Acknowledgment

I cannot help but to feel a bit nostalgic about my years at the electromagnetics group, as I am writing my final words PhD dissertation (yes, as a true Quentin Tarantino fan I am required to place the chapter I wrote last as the first chapter in my book). The obvious page-turner that you are holding in your hands, is not only a representation of a five-year long exciting research adventure, but it is also the result of one of the most transformative periods in my life thus far. It has been a Herculean task, but as the expression loosely translated from Dutch says: many hands make light work. That is why I want to take this opportunity to thank everyone that has been involved in my PhD, both in and out off the office, for their insights, effort and patience.

First of all, I would like to express my gratitude towards both of my promoters, prof. Hendrik Rogier en prof. Sam Lemey. Both of them have been in my corner 24/7 and I cannot thank them enough for their continuous support and assistance. Hendrik, thank you for taking a chance on me. I still remember the moment when prof. Van Torre brought me to present my master thesis in a small room in the Technicum, hoping you would take me under your wing as a PhD student. Not only is it because of you that I could pursue a PhD, but your advice and critical sense towards my research have significantly enhanced the quality of this dissertation. Sam, I don't even know where to begin. My professional successes can be largely attributed to our intense collaboration, where ideas became concepts and concepts became reality. Together we pushed the boundaries of the state-of-the-art and I am truly honored to have been part of that process. I have an enormous amount of respect for you, both professionally and personally, and I can't wait to see what the future holds for you. Furthermore, if you ever find yourself in the vicinity of Rozebeke city, you and your offspring are always welcome for a drink and/or BBQ!

Next, I would like to thank prof. Piet Demeester, director of the IDLab-department, for providing a research environment where not only excellence is promoted and pursued, but also facilitates and encourages entrepreneurship and ambition. Furthermore, I would like to express my gratitude towards the full examination board for meticulously reading my dissertation and providing me with apt and challenging questions during my defense: prof. Guillaume Ducournau, prof. Anthony Ghiotto, prof. Günter Roelkens, prof. Patrick Van Torre.

Part of what made my research journey so exciting can be attributed to the amount of multi-disciplinary work and, as such, I would like to thank certain people within IDLab for their efforts. First of all, a big thank you to prof. Bart Kuyken and Steven Verstuyft of the Photonics Research Group who enabled me to extend my research to mmWave and THz frequencies by educating me on clean room processes and

providing me with access to the Ghent University clean room facility. Furthermore, I would like to thank prof. Guy Torfs, Joris Van Kerrebrouck and Laurens Bogaert for their support and counsel during the increasing number of joint theses and research projects. I would also like to thank prof. Eli De Poorter, Jen Rossey, Bart Jooris and Ben Van Herbruggen for the fruitful collaboration over the years, resulting in multiple joint publications. Finally, prof. Bart Smolders and dr. Ad C. F. Reiniers of TU Eindhoven receive my gratitude for their contributions in the publication on the hybrid on-chip antenna technology.

Many hands make light work. I said it before and I will say it again. If not for the efforts and enthusiasm of my colleagues in the electromagnetics group and QUEST, the insights presented in this work may not have been up to the required quality standard and the acknowledgment section would have been like my antennas: highly efficient and compact. First of all, I would like to thank prof. Patrick Van Torre. Patrick, I don't think you realize the magnitude of the impact you have had on my career... Your passion for electronics is more infectious than COVID-19 and it radiates during your lectures. You are the reason I became passionate about electronics and you enabled me to pursue that passion on a higher level by recommending me to Hendrik for a PhD position. I am eternally grateful for that, so wherever I go, you are always welcome for a drink and a talk about whatever crazy story you have from your last conference. *Sé que tienes muchos historias, porque sé que eres un hombre muy aventurero.* I would also like to take this opportunity to thank prof. Dries Vande Ginste. I thoroughly enjoyed working with you and relying on your expertise of coupled oscillators and other obscure EMC phenomena. Other than that, your vigorous and recalcitrant personality was a true delight and brought about several intriguing lunch/coffee break discussions.

And now, the moment every PhD student and recent post-doc (yes you, Olivier and Martijn) have been waiting for: it's time for your appraisal! First of all, to the old guard: Simon and Michiel, putting two evil geniuses in the same office is always a recipe for entertainment and you guys didn't disappoint. Also Michiel, I'm sorry for any long term damage that resulted from my 'Michieeeeeeeeel'-shenanigans. Arne, I think it's time to bury the hatchet and move on... Let's forget that time I stabbed you in the back during the Game of Thrones board game and give the game one more chance. I PROMISE I WON'T DO IT AGAIN! Martijn, I think back fondly on our many awkward hallway encounters, absurd lunch conversations and zingers that fly around at random times. But what still astonishes me to this day is your ability to memorize anything for an indefinite amount of time... So let's make a deal: if you can remember the color of my left shoe lace in ten years, I'll get you a leather bound first edition *Harry Potter and the Philosopher's Stone*. En dan nu in het Vlaams: Olivier. Ik herinner me nog de eerste dag toen ik op de bureau binnenkwam en je mij meteen herkende van ingenieursproject in het eerste jaar burgerlijk ingenieur. Je klonk zo overtuigend, dat ik het meteen voor de waarheid aannam en er sinds dien nooit meer aan getwijfeld heb! Jokes aside, ik heb mij de afgelopen jaren kostelijk geamuseerd met u (zowel op het werk als op CSGO) en ik kijk met trots terug de vele meesterwerken die we samen hebben neergezet.

Now, back to English to give some praise for my disciples in office 210.031. Igor, your enthusiasm and inexhaustible amount of energy were an utter delight when working together. Also, I've never had anyone do random cartwheels in the office and just going on without any explanation... Amazing! Laura, you are for sure the weirdest girl in the office, but the fact our sense of humor is exactly the same made you the perfect desk neighbor. Thanks for enduring me with such grace, it made my day more than once! Bye Felicia! Seppe, unfortunately my mission of reverting you into an omnivore failed and, in fact, backfired slightly. But next time I'm eating a hummus-based vegetarian dish, I will think back fondly on our in-office banter. Nicolas, the new and improved office-representative, as your predecessor I can only give you one advice: Don't listen to my advice when it comes to being the office-representative, as you already accomplished more in four months than I did in four years. Speaking of office representatives, Thomas Ameloot, you did a fine job keeping 'the other office' in check. Having a hardware engineer infiltrate the computational office and rising to a position of power surpassed my wildest dreams, great job! Arno, I know I truly enjoyed your presence in the group, but right now everything is being overshadowed by the footage you showed me of the Sami. Thank you for that. Moreover, I would like to thank the rest the EM colleagues for the enjoyable hallway encounters and lunchtime discussions: Gert-Jan, Jelle, Dries, Pieter and Duygu.

In particular, I would like to thank a special group of 'colleagues': Thomas Deckmyn, Kamil, Alessandro and Nick. The many whiskey tastings, barbecues, birthday parties, weddings, etc... we shared over the last couple of years have truly shaped a friendship that will last a lifetime! Thomas, although we initially bonded over the forbidden delight that is nicotine, it was the many nights we spent (drinking, smoking and gossiping) in your house, in Ghent and later in Eernegem that consolidated the friendship. You always made me feel welcome in your home and I truly appreciate being a part of your life. I would also like to thank you to give me the push to finally buy my motorcycle. Several years later, I stand before you, ready to fulfill my duties to the Sons of Maxwell MC. Kamil, I treasure your friendship with all my heart. Your kindness and support know no bounds and I cannot thank you enough for it. You are a big part of my life and it truly is an honor to call you my brother! Alessandro, I don't know why but every time we are together we start acting like crazy pubescent teenagers. Honestly, I love your 'in the face' attitude and your energy gets me hyped up every time we meet. More of that please! And last, but certainly not least... Nick. A dirty mind is a joy forever. That might be the motto that brought Nick and me together many years ago and still provides us with plenty of laughter to this day. Some might think that one day we will grow up, but we know better. Nick, you are an amazing friend that is always there when you were needed. Let's drink to our past years and the many years to come, sláinte!

As the saying goes: behind every strong researcher, there is an even stronger group of friends. Spending quality time with amazing people was imperative for maintaining a decent level of sanity and, as such, I would like to take the opportunity to thank my friends. First of all, *Magic más duro*. Tomas, Jelle, Jamin and Geoffrey,

you guys for sure know what a big part you are of my life, but still I want to thank you all for everything you did. You pick me up when I'm in pieces, you remind me of my priorities and keep me in check if I tend to go in overdrive (once again). You guys are amazing and I am eternally grateful for your support and love. Laurence, you also get a special place in this acknowledgment as you have been a life long rock in my life. You have been around for almost every important milestone in my life and I hope we can still share many more in the future. Thanks for everything Lau! The same can be said from my boys from the hood: Diederik, Bastiaan, Egon, Jan-Bart, Tim, Louis, Bram, Edward, Kevin, Lukas, Arnaut, Daan, Mart and Matthias. Although these last years I haven't been as involved with you guys as I would like, you always made me feel welcome and appreciated (no matter how many 'closets I was assembling'). The vergaringen and bachelor parties are signatures for how epic our friend group is and I cannot wait until we conquer the next city during my own bachelor party! I would also like to thank the 'Dining club', as they provided me with abundant entertainment on many occasions. Thomas V, Bernard, Nadine and Nick (again), thanks for all those tasty dishes and drinks afterwards! Finally, I would like to thank the RNX9600 clan for the 1333 hours of online fun. Sanders, James, El Jefe, Arno, Beno, Melvin and Brambo, thanks boosting my rank on CSGO and the amazing LAN events.

Now a small intermezzo in Dutch. Mijn doorzettingsvermogen, successen en persoonlijke groei heb ik grotendeels te danken aan de onvoorwaardelijke steun van mijn familie. In het bijzonder wil ik graag mijn ouders bedanken om steeds in mij te blijven geloven, ook als ik jullie daar niet altijd evenveel reden toe gaf. Ik ben jullie niet alleen eeuwig dankbaar voor alles wat jullie voor mij gedaan hebben, maar ook voor het voorbeeld en de waarden die jullie ons hebben meegegeven. Ook mijn zussen zou ik graag willen bedanken om niet steeds weg te lopen als ik mijn onderzoek probeerde uit te leggen. Ik hoop dat jullie dit keer na mijn presentatie toch iets zullen begrepen hebben. De rest van mijn familie zou ik ook graag willen bedanken: Maggie, Jan, Kim, Sam, Iza en kleine Flo. Ook mijn meter en peter wil ik expliciet bedanken om steeds met grote interesse te blijven vragen: "*Hoe is 't op 't school?*". Meter en peter, het is eindelijk gedaan met 't school!

And finally, I would like to dedicate this last paragraph to my special person: Laura Sofia Parejo Ruiz (or mi amor, as everyone knows her). Three years ago we met each other on a crazy night in Budapest and ever since I have been madly in love with you. Against all odds, we made the long distance relationship work and now I am happier than ever knowing that we will spend our lives together in marriage. I owe you everlasting gratitude for bringing me closer to my family and friends, your unconditional love and honesty and your relentless support when it comes to my ambition. Like we say in Dutch, *I fell with my butt in the butter*! Mi amor, de verdad eres el amor de mi vida y no puedo esperar para comenzar el resto de mi vida contigo. El matrimonio, la casa y los niños... Eres mi futuro!

Gent, October 2021
Quinten Van den Brande

The biggest fight you'll ever have is between who you are now and who you are capable of becoming.

JAX TELLER

Contents

Samenvatting

De samenleving staat aan de vooravond van een nieuwe industriële revolutie, waar zelforganiserende fabrieken autonoom zullen draaien met minimale menselijke tussenkomst en waar producten hun eigen productiecyclus zullen optimaliseren op basis van realtime klantvraag. Dit concept, genaamd Industrie 4.0 (Engels: Industry 4.0), mogelijk gemaakt door een combinatie van belangrijke technologische ontwikkelingen zoals het Internet der Dingen (Engels: Internet of Things, IoT), cyber-fysieke systemen (Engels: Cyber Physical Systems, CPS) en big data-analyse, revolutioneert het industriële landschap wereldwijd. Het zal niet alleen de operationele efficiëntie maximaliseren, afvalproductie minimaliseren en productietransparantie verbeteren, maar het zal gepersonaliseerde producten in een oogwenk beschikbaar maken tegen een betaalbare prijs.

Dit complexe technologische Industrie 4.0-ecosysteem wordt gevoed door een enorme hoeveelheid aan sensorgegevens, waardoor professionals kritieke situaties efficiënter en nauwkeuriger kunnen interpreteren en erop kunnen reageren. Deze enorme hoeveelheid data en de uitgebreide netwerken van CPSen stellen hoge eisen aan de volgende generatie van industriële draadloze netwerken (Engels: Industrial Wireless Networks, IWN). Communicatiekanalen met een korte vertraging en een hoge datasnelheid met een linkbetrouwbaarheid tot 99,999% zullen essentieel worden voor het succes van veel Industrie 4.0-toepassingen. Om volledig autonome herconfiguratie van slimme fabrieken mogelijk te maken, wordt nauwkeurige en realtime tracking van activa een noodzakelijke functie. In deze context is ultrabreedbandtechnologie geïdentificeerd als een belangrijke factor voor het succes en de wijdverspreide acceptatie van Industrie 4.0. Enerzijds zorgt het gebruik van pulsgebaseerde-ultrabreedbandtechnologie (Engels: Impulse-Radio Ultra-Wideband technology, IR-UWB technology) niet alleen voor robuuste en snelle communicatie, maar het laat ook de ontwikkeling toe van zeer nauwkeurige realtime lokalisatiesystemen (Engels: Real-Time Location Systems, RTLS). Het maakt autonome drone- en voertuigtoepassingen mogelijk vanwege de lokalisatienauwkeurigheden tot 15 cm, zelfs in dichte en ongunstige slimme fabrieksomgevingen die vaak onderhevig zijn aan sterke multipadeffecten en interferentie. Anderzijds kunnen multi-antenne communicatiesystemen op zowel millimetergolf (Engels: Millimeter-Wave, mmWave) als terahertz (Engels: Terahertz, THz) frequenties voldoen aan de reeks strikte, heterogene vereisten, dankzij de grote beschikbare bandbreedte op deze frequentiebanden. Vooral met de komst van toekomstige toepassingen die aangevulde en virtuele realiteit (Engels: Augmented and Virtual Reality, AR/VR) implementeren, zal deze volgende generatie van draadloze systemen een pijler worden voor het harmoniseren van de interactie tussen mens en machine, waardoor het volledige potentieel van Industrie 4.0 wordt ontgrendeld.

In dit werk wordt het potentieel van luchtgevulde substraatgeïntegreerde golfgeleidertechnologie (Engels: Air-Filled Substrate-Integrated-Waveguide technology, AFSIW technology) geanalyseerd voor zeer efficiënte ultrabreedbandantennes (Engels: Ultra-Wideband antennas, UWB antennas) in de context van twee technologische pijlers van Industrie 4.0. Deel I richt zich op robuuste en zeer efficiënte UWB-antennes voor betrouwbare en nauwkeurige IR-UWB RTLSen in Industrie 4.0-toepassingen. Het gebruik van zeer korte pulsen in IR-UWB technologie vereist de simulatie van parameters op systeemniveau, eigen aan de beoogde toepassing, naast de traditionele optimalisatie van de antenne in het frequentiedomein. Om een robuuste antennewerking te garanderen in een heterogene IoT omgeving, die we ook tegenkomen in de fabriek van de toekomst, is er speciale aandacht besteed aan het antenne-integratieplatform.

In Hoofdstuk 2 bespreken we het belang van optimalisatie op systeemniveau bij IR-UWB antenneontwerp en de directe implicaties daarvan op de prestaties van het RTLS met betrekking tot nauwkeurigheid en betrouwbaarheid. Om de invloed van het IR-UWB antennesysteem op deze parameters op systeemniveau te analyseren, is een modulair, systeemgericht full-wave/circuit IR-UWB co-optimalisatieraamwerk ontwikkeld, dat het antennesysteem in het frequentie-, het tijds- en het ruimtelijk domein optimaliseert. Eerst wordt een circuitmodelrepresentatie van een IR-UWB systeem gepresenteerd, waarmee simulatie op systeemniveau voor één specifieke antenneconfiguratie mogelijk is. Concreet betekent dit dat voor elke variatie in zend- of ontvangstantenne, of het nu antenne-oriëntatie of -topologie is, de volledige IR-UWB link opnieuw moet worden gesimuleerd. Om de berekening van de overdrachtsfunctie van de ultrabreedbandige antenneverbinding mogelijk te maken op basis van de full-wave simulatieresultaten van de individuele antennes, wordt deze daarom ontbonden en worden nauwkeurige simulaties mogelijk met aanzienlijk verminderde rekenkracht. Vervolgens wordt de verkregen IR-UWB antennesysteemkarakterisering in de frequentie, de tijd en het ruimtelijke domein gecombineerd door de parameters op systeemniveau, zoals de systeemgetrouwheidsfactor (Engels: System Fidelity Factor, SFF) en de afstandsinschattingsfout (Engels: Distance Estimation Error, DEE) te berekenen. In de context van RTLSen, karakteriseren de SFF en de DEE respectievelijk de hoeveelheid oriëntatie-specifieke pulsvervorming en afstandsbias die door het antennesysteem wordt geïntroduceerd, wat respectievelijk de betrouwbaarheid en nauwkeurigheid van het RTLS specifieert. Bovendien wordt het voorgestelde raamwerk gevalideerd door een uitgebreide meetcampagne, die een zeer goede overeenkomst tussen simulaties en metingen laat zien. Ten slotte worden de prestaties van het raamwerk vergeleken met een commerciële full-wave solver, die een verbetering van de simulatietijd laat zien van meerdere grootte-ordes, vooral bij het simuleren van meerdere antenne-oriëntaties.

Het voorgestelde simulatieraamwerk wordt gebruikt in Hoofdstuk 3 om een robuuste en zeer efficiënte IR-UWB antenne in AFSIW technologie te ontwikkelen, gericht op optimalisatie van de SFF voor zeer betrouwbare RTLSen. Om aan de opgelegde ontwerpeisen te voldoen, is gekozen voor een slotantenne met achter-

liggende caviteit, omdat deze gunstige stralingseigenschappen vertoont die ongewenste straling aan de achterkant minimaliseren en daarom een robuuste en platformonafhankelijke antennewerking garanderen. Om het inherente smalbandgedrag van een slotantenne met achterliggende caviteit te verhelpen, wordt modebifurcatie toegepast op een luchtgevulde caviteit door halfmodekoppeling te implementeren in gestapelde AFSIW technologie, waardoor een ultrahoge efficiëntie over een ultrabrede frequentie band bekomen wordt. Met behulp van het voorgestelde simulatieraamwerk in Hoofdstuk 2, wordt een grondige optimalisatie op systeemniveau uitgevoerd van het antennesysteem, waardoor uitstekende IR-UWB prestaties worden gegarandeerd binnen de half-vermogen bundelbreedte (Engels: Half-Power Beamwidth, HPBW) van de antenne. Meer specifiek wordt een SFF groter dan 98% en een relatieve groepsvertraging kleiner dan 100 ps verkregen. Hierdoor voldoet de antenne aan de eisen voor een betrouwbaar en nauwkeurig IR-UWB RTLS, aangezien de pulsvervorming en variaties in de aankomsttijd tot een minimum worden beperkt. De antenneprestaties worden gevalideerd door metingen uit te voeren in twee scenario's. Eerst wordt de prestatie in de vrije ruimte geanalyseerd door het opmeten van de frequentie- en tijdsdomeineigenschappen in een volledig anechoische kamer. Vervolgens wordt de antenne gevalideerd in een realistisch worst-case implementatiescenario. Deze metingen bewijzen dat de antenneprestaties onaangetast blijven op een grote verscheidenheid aan integratieplatformen. Ten slotte, om het voordeel van AFSIW technologie ten opzichte van dielektrisch-gevulde substraatgeïntegreerde golfgeleidertechnologie (Engels: Dielectric-Filled Substrate-Integrated-Waveguide technology, DFSIW technology) te illustreren, wordt een vergelijkende analyse uitgevoerd met betrekking tot de vormfactor, de bandbreedte en de stralingsefficiëntie. Deze observaties leiden tot de conclusie dat de DFSIW technologie het volledige potentieel van de substraatgeïntegreerde golfgeleidertechnologie (Engels: Substrate-Integrated-Waveguide technology, SIW technology) voor de beoogde toepassing van een betrouwbare en nauwkeurige IR-UWB RTLS tegenhoudt.

Uiteindelijk analyseert en behandelt Hoofdstuk 4 het probleem van oriëntatiespecifieke fouten bij het schatten van afstanden, geïntroduceerd door het antennesysteem, voor zeer nauwkeurige IR-UWB RTLSen. Aangezien dit probleem zich vaak voordoet bij sectorantennes, wordt een vlakke sectorantenne voorgesteld voor IR-UWB lokalisatie met minimale fouten bij het schatten van de afstand . Een grote HPBW en een minimale DEE binnen die HPBW worden verkregen door oordeelkundig twee vlakke omgekeerde-F antennes (Engels: Planar Inverted-F Antennas, PIFA) te combineren in één antennevoetafdruk, gevolgd door een rigoureuze optimalisatie op systeemniveau. Simulaties van het geoptimaliseerde antennesysteem vertoont een minimale SFF van ten minste 90% en een maximale DEE van 10 mm, binnen de volledige HPBW van 120°. De antenneprestaties zijn gevalideerd door middel van uitgebreide metingen in zowel het frequentie- als het tijdsdomein, waarbij een SFF groter dan 90% en een DEE kleiner dan 4 mm binnen de HPBW van de antenne worden aangetoond.

Deel II van dit proefschrift gaat dieper in op het potentieel van AFSIW technologie

bij on-chip antennes, bedoeld voor draadloze systemen van de volgende generatie. Het lost de kritieke problemen van de huidige mmWave en THz on-chip antennes op, waardoor een hoge antenne-efficiëntie mogelijk wordt over een grote impedantiebandbreedte, en dit binnen een compacte footprint. Bovendien wordt speciale aandacht besteed aan de ontwikkeling van fabricagetechnologieën die compatibel zijn met bestaande silicium bewerkingstechnologieën, om de toepassing ervan in cleanroom-omgevingen op industriële schaal te bevorderen.

In Hoofdstuk 5 richten we ons op de technologische uitdagingen die samenhangen met sterk geïntegreerde millimetergolf on-chip antennesystemen, om zeer efficiënte multi-antennesystemen met adaptieve bundelsturing mogelijk te maken. De huidige integratiestrategieën, zijnde antenne op chip (Engels: Antenna-on-Chip, AoC) en antenne in verpakking (Engels: Antenna-in-Package, AiP), worden respectievelijk typisch gekenmerkt door een slechte stralingsefficiëntie, vanwege de ongunstige elektromagnetische materiaaleigenschappen in siliciumsubstraten, en de hoge interconnectieverliezen die meer uitgesproken worden bij hogere frequenties. Hiertoe wordt een hybride integratiestrategie voorgesteld voor compacte, breedbandige en zeer efficiënte millimetergolf on-chip antennes, gebaseerd op AFSIW technologie. Een hoogfrequent laminaat implementeert een gestapelde patchconfiguratie en ondersteunt een chip. De chip zelf implementeert een gemetalliseerde, lucht-gevulde caviteit, micromachinaal gemaakt direct boven de gestapelde patchantennes, en een apertuurgekoppelde antennevoeding. Deze laatstgenoemde wordt geïmplementeerd op de achterzijde van de caviteit en voedt de gestapelde patchantennes via een opening in de lucht-gevulde caviteit. Hierdoor wordt het grootste deel van de elektromagnetische golven afgeschermd van het verlieshebbende siliciumsubstraat, terwijl interconnectie verliezen worden vermeden. Dit resulteert in een gemeten totale antenne-efficiëntie van meer dan 90% over de volledige beoogde millimetergolf frequentieband. Gecombineerd met de compacte antenne-voetafdruk van $0.49\,\lambda_{min} \times 0.49\,\lambda_{min}$, is dit een veelbelovend antenne-element voor de constructie van breedbandige antenneroosters met een breed stuurbereik.

Ten slotte bespreekt Hoofdstuk 6 een nieuwe polymeer-gebaseerde AFSIW technologie voor zeer efficiënte breedbandige on-chip THz antennesystemen. De opkomst van deze nieuwe technologie maakt de weg vrij voor traditionele fasegestuurde antenneroosters op THz frequenties, waardoor een goedkope en schaalbare oplossing wordt geboden voor bundelsturing in THz communicatietoepassingen. Een slotantenne met achterliggende caviteit, een exponentieel toelopende voeding en gemodificeerd slot is ontworpen om het technologische potentieel te demonstreren. Een dun, verliesarm polymeersuperstraat, die de antennevoeding en het stralingselement ondersteunt, wordt gespannen over een AFSIW caviteit die micromachinaal wordt gemaakt in een goedkoop, standaard siliciumsubstraat. Door gebruik te maken van mode-bifurcatie in de slotantenne bovenop een lucht-gevulde caviteit, wordt een frequentie-onafhankelijke antenne-efficiëntie van meer dan 90% verkregen over een grote bandbreedte. Bovendien verkleint de geoptimaliseerde vorm van het stralend slot de antennevoetafdruk aanzienlijk, wat absoluut noodzake-

lijk is voor toepassingen met een groot bundelstuurbereik. Naast radiofrequentieoptimalisatie (Engels: Radio Frequency optimization, RF optimization) worden zowel mechanische als thermische belasting onderzocht om robuuste antenneprestaties te garanderen onder verschillende werkingsomstandigheden. De alleenstaande antenne is geoptimaliseerd voor gebruik in de $[252.72 - 321.84]$ GHz-frequentieband van de IEEE 802.15.3d-2017-standaard, en vertoont een antenne-efficiëntie van meer dan 88% in de volledige frequentieband binnen een voetafdruk van 500 $\mu m \times 500$ μm. Daarnaast werd ook een 1x4 lineair antennerooster, geïmplementeerd door vier van de gerealiseerde eenheidsantenne-elementen 560 μm uit elkaar te plaatsen, ontworpen. Dit rooster heeft een bundelstuurbereik van 60° met een antennewinst groter dan 11,54 dBi. Bovendien blijft de onderlinge koppeling onder -15 dB in de volledige frequentieband, wat het immense potentieel van dit ontwerp en zijn technologie aantoont voor een goedkoop en sterk geïntegreerd systeem-op-chipraamwerk (Engels: System-on-Chip framework, SoC framework) voor THz communicatie.

Summary

Society is on the verge of a new industrial revolution, where self-organizing factories will run autonomously with minimal human interference and where products will optimize their own production cycle based on real-time customer demand. This concept, dubbed Industry 4.0, facilitated by a combination of major technological advancements such as the Internet-of-Things (IoT), Cyber-Physical Systems (CPSs) and big data analytics, is disrupting the industrial landscape worldwide. Not only will it improve operational efficiency, minimize waste production and enhance production transparency, it will also make personalized products available in the blink of an eye at an affordable price.

This complex technological Industry 4.0 ecosystem is fed by an enormous amount of sensory data, enabling professionals to interpret and react to critical situations more efficiently and accurately. This enormous amount of data and the extensive networks of CPSs are imposing stringent requirements on next generation Industrial Wireless Networks (IWNs). Low-latency, high data-rate communication channels with a link reliability up to 99.999% will become imperative for the success of many Industry 4.0 applications. Furthermore, to facilitate fully autonomous reconfiguration of smart factories, accurate and real-time asset tracking is becoming an imperative feature. In this context, ultra-wideband technology has been identified as a key enabler for the success and widespread adoption of Industry 4.0. On the one hand, the use of Impulse Radio Ultra-Wideband (IR-UWB) technology provides not only robust and high-speed communication, but it facilitates the development of highly accurate Real-Time Locating Systems (RTLSs). It enables autonomous drone and vehicle applications because of its localization accuracies up to 15 cm, even in dense and unfavorable smart factory environments, commonly subjected to strong multipath effects and interference. On the other hand, multi-antenna communication systems at both Milimeter-Wave (mmWave) and Terahertz (THz) frequencies are able to address the set of stringent heterogeneous requirements, owing to the large available bandwidth at these frequency bands. Especially with the advent of future applications that incorporate Augmented/Virtual Reality (AR/VR), these next-generation wireless systems will become a pillar for harmonizing the interaction between man and machine, thereby unlocking the full potential of Industry 4.0.

In this work, the potential of Air-Filled Substrate-Integrated-Waveguide (AFSIW) technology is elucidated for highly efficient ultra-wideband antennas in the context of two technological facilitators of Industry 4.0. Part I focuses on robust and highly efficient Ultra-Wideband (UWB) antennas for reliable and precise IR-UWB RTLSs in Industry 4.0 applications. The use of sub-nanosecond duration pulses in IR-UWB technology requires the simulation of system-level parameters, propri-

etary to the envisioned application, in addition to traditional frequency-domain antenna optimization. Furthermore, to guarantee robust antenna operation in a heterogeneous IoT environment, as encountered in the factory of the future, special care was given to take into account the antenna integration platform.

In Chapter 2, we discuss the importance of system-level optimization in IR-UWB antenna design and its direct implications on RTLS performance, with regard to accuracy and reliability. To analyze the IR-UWB antenna system's influence on these system-level parameters, a modular, system-oriented full-wave/circuit IR-UWB co-optimization framework is developed, characterizing the antenna system in the frequency, the time and the spatial domain. First, a circuit model representation of an IR-UWB system is presented, enabling the system-level simulation for one specific antenna configuration. More specifically, this means that for every variation in transmit or receive antenna, being antenna orientation or topology, the complete IR-UWB-link must be simulated again. To this end, the antenna link is decomposed to allow the calculation of the antenna link transfer function based on the full-wave simulation results of standalone antennas, thereby enabling highly accurate simulations with significantly reduced computational resources. Next, the obtained IR-UWB antenna system characterization in the frequency, the time and the spatial domain are combined by computing system-level metrics, such as the System Fidelity Factor (SFF) and Distance Estimation Error (DEE). In the context of RTLSs, the SFF and the DEE characterize the amount of orientation-specific pulse distortion and ranging bias introduced by the antenna system, respectively, thereby representing the reliability and accuracy of the RTLS, respectively. Furthermore, the proposed framework is validated by an extensive dedicated time-domain measurement campaign, showing very good agreement between simulations and measurements. Finally, the framework performance is benchmarked against a commercial full-wave solver, exhibiting an improvement in simulation time by orders of magnitude, especially when simulating multiple antenna orientations.

The proposed simulation framework is leveraged in Chapter 3 to develop a robust, highly-efficient, IR-UWB antenna in AFSIW technology, focused on optimization of the SFF for highly reliable RTLSs. To satisfy the imposed design requirements, a cavity-backed slot antenna topology is selected, as it exhibits favorable radiation properties that minimize undesired backside radiation and, therefore, guarantees robust and integration-platform-independent antenna operation. To mitigate the inherent narrowband behavior of a cavity-backed slot antenna, mode-bifurcation is leveraged on an air-substrate by implementing half-mode coupling in stacked AFSIW technology, enabling an ultra-high efficiency over an ultra-wide frequency band. Using the proposed simulation framework in Chapter 2, a thorough system-level optimization is performed of the antenna system, comprising two of the antennas proposed in this chapter, guaranteeing outstanding IR-UWB performance within the antenna's Half-Power Beamwidth (HPBW). More specifically, an SFF larger than 98% and a relative group delay smaller than 100 ps are obtained. As a result, the antenna complies with the requirements for a reliable and precision IR-UWB RTLS, as the amount of pulse distortion and time-of-arrival variations are

minimized. The antenna performance is validated by performing measurements in two scenarios. Initially, the free-space performance is characterized by measuring the frequency- and time-domain properties in a fully anechoic chamber. Additionally, the antenna is validated in a real-life worst-case deployment scenario, proving that its antenna performance remains unaffected on a large variety of integration platforms. Finally, to illustrate the advantage of AFSIW technology over Dielectric-Filled Substrate-Integrated-Waveguide (DFSIW) technology, a comparative analysis is performed on the form factor, the bandwidth and the radiation efficiency. These observations lead to the conclusion that DFSIW technology inhibits the full potential of Substrate-Integrated-Waveguide (SIW) technology for the envisaged application of a highly reliable and precision IR-UWB RTLS.

Ultimately, Chapter 4 analyzes and addresses the issue of orientation-specific distance estimation biasing errors, introduced by the antenna system, for highly precise IR-UWB RTLSs. As this problem is commonly encountered in sectoral antennas, a planar sectoral antenna is proposed for IR-UWB localization with minimal distance estimation biasing errors. A large HPBW and a minimal DEE within that HPBW are obtained by judiciously combining two Planar Inverted-F Antennas (PIFAs) into one antenna footprint and rigorous system-level optimization. The optimized antenna system, comprised of the antenna proposed in this Chapter and Chapter 3, exhibits a minimal simulated SFF of at least 90% and a maximal simulated DEE of 10 mm, within the complete HPBW of 120°. The antenna performance is validated by means of extensive measurements in both the frequency and time-domain, showing an SFF larger than 90% and a DEE lower than 4 mm within the antenna's HPBW.

Part II of this dissertation elaborates on the potential of AFSIW technology in on-chip antennas, intended for (beyond) 5G wireless systems. It addresses the critical drawbacks of current mmWave and THz on-chip antennas, thereby enabling high antenna efficiencies over a large impedance bandwidth, within a compact footprint. Furthermore, special attention was devoted to develop fabrication technologies that are compatible with existing silicon process technology, to promote their adoption in industrial scale clean room environments.

In Chapter 5, we focus on the technological challenges associated with highly integrated mmWave on-chip antenna systems, to enable highly efficient multi-antenna systems with adaptive beamforming capabilities. The current integration strategies, being Antenna-on-Chip (AoC) and Antenna-in-Package (AiP), typically suffer from poor radiation efficiency, due to the unfavorable electromagnetic material properties of bulk silicon substrates and high interconnect losses that become more pronounced at higher frequencies, respectively. To this end, a hybrid integration strategy is proposed for compact, broadband and highly-efficient mmWave on-chip antennas, based on AFSIW technology. A high-frequency laminate implements a stacked patch configuration and supports a chip. The chip itself implements a metallized air-filled cavity, micromachined directly above the stacked patches, and an aperture-coupled antenna feed. The latter is implemented at the cavity backside,

exciting the stacked patch antennas through an aperture in the air-filled cavity. By doing so, the majority of the electromagnetic waves are shielded from the lossy silicon substrate while avoiding any interconnect losses. This results in a measured total antenna efficiency above 90% over the complete targeted mmWave frequency band. Combined with the compact antenna footprint of $0.49\,\lambda_{min} \times 0.49\,\lambda_{min}$, this antenna element shows great promise towards the construction of broadband antenna arrays with a broad steering range.

Finally, Chapter 6 discusses a novel polymer-enabled AFSIW technology for highly efficient broadband on-chip THz antenna systems. The emergence of this novel technology paves the way for traditional phased array topologies at THz frequencies, thereby providing a low-cost and scalable solution for beamsteering in THz communication applications. A cavity-backed slot antenna with exponentially tapered feed and modified slot is designed, both in a stand-alone and a 1x4 linear array configuration, in an effort to demonstrate the technological potential. A thin, low-loss polymer superstrate, supporting the antenna feed and radiating element, is suspended on top of an AFSIW cavity that is micromachined into a low-cost, standard silicon substrate. Leveraging mode-bifurcation in the cavity-backed slot antenna, on top of an air-filled cavity, provides a frequency-independent antenna efficiency larger than 90% over a very large bandwidth. Furthermore, manipulating the radiating slot significantly reduces the antenna footprint, imperative for grating-lobe free beamsteering applications. In addition to Radio Frequency (RF) optimization, both mechanical and thermal stress are investigated to guarantee robust antenna performance under different operating conditions. The stand-alone antenna is optimized for operation in the $[252.72 - 321.84]$ GHz frequency band of the IEEE 802.15.3d-2017 standard, exhibiting an antenna efficiency above 88% in the complete frequency band within a footprint of 500 $\mu m \times 500\ \mu m$. The 1x4 linear array, implemented by spacing four of the realized unit antenna elements 560 μm apart, shows grating-lobe free beamsteering capabilities up to 30° with a gain larger than 11.54 dBi. Moreover, mutual coupling remains below -15 dB and a Front-to-Back Ratio (FTBR) above 16.8 dB is obtained in the complete frequency band, demonstrating the immense potential of this design and its technology for a low-cost and highly-integrated System-on-Chip (SoC) framework for THz communication.

List of Abbreviations

AC Alternating Current
ADS Advanced Design System
AFSIW Air-Filled Substrate-Integrated-Waveguide
AiP Antenna-in-Package
AoC Antenna-on-Chip
AP Access Point
AR/VR Augmented/Virtual Reality
AUT Antenna Under Test
AWG Arbitrary Waveform Generator
BCB Benzocyclobutene
CMOS Complementary Metal Oxide Semiconductor
CPS Cyber-Physical System
CPPS Cyber-Physical Production Systems
C-RAN Cloud Radio Access Network
DAS Distributed Antenna System
DEE Distance Estimation Error
DFSIW Dielectric-Filled Substrate-Integrated-Waveguide
EMI Electromagnetic Interference
FTBR Front-to-Back Ratio
GCPW Grounded Co-Planar Waveguide
GPS Global Positioning System
GSG Ground-Signal-Ground
HPBW Half-Power Beamwidth
ICP Inductively Coupled Plasma
IoT Internet-of-Things
IR-UWB Impulse Radio Ultra-Wideband
IWN Industrial Wireless Network
M2M Machine-to-Machine
MEMS Microelectromechanical Systems

mmWave Milimeter-Wave
PCB Printed Circuit Board
PECVD Plasma Enhanced Chemical Vapor Deposition
PIFA Planar Inverted-F Antenna
RF Radio Frequency
QoS Quality of Service
RIE Reactive Ion Etching
RTLS Real-Time Locating System
RTO Real-Time Oscilloscope
SIW Substrate-Integrated-Waveguide
SFF System Fidelity Factor
SoC System-on-Chip
TDoA Time Difference of Arrival
THz Terahertz
ToA Time of Arrival
UTC-PD Uni-Traveling-Carrier Photodiode
UWB Ultra-Wideband
WLAN Wireless Local Area Network
WPAN Wireless Personal Area Network

List of Symbols

Mathematical symbols

$\|.\|$	Magnitude of a complex or real number
$.^*$	Complex conjugate
$\circ$	Vector inner product
$*$	Convolution
$\hat{.}$	Unit vector
j	Imaginary unit, with $j^2 = -1$
$\mathcal{H}$	Hilbert transform
$\mathbf{a}$	Vector a
$\mathbf{u_0}$	Direction vector
θ	Elevation angle
ϕ	Azimuth angle

Electromagnetic symbols

c	Speed of light, $c = 299792458$ [m/s]
t	Time, δt indicates a time step [s]
f	Frequency, δf indicates a frequency step [Hz]
λ	Wavelength [m]
ω	Angular frequency [rad/s]
k	Wave number, $k = 2\pi/\lambda$ [rad/m]
ϵ_r	Relative permittivity of a medium
μ_r	Relative permeability of a medium
$\tan\delta$	Loss tangent
Z_c	Free-space wave impedance, $Z_c = 376.7$ [Ω]
$\mathbf{E^{inc}}$	Electric field [V/m]
V	Voltage [V]
I	Current [A]

Symbols specific to IR-UWB (part I)

Z_L	Load impedance [Ω]
Z_s	Source impedance [Ω]
Z_0	Reference impedance [Ω]

S	Scattering parameters
H_{sys}	System transfer function
h_{sys}	System impulse response
s	Input pulse
x	Output pulse
SFF	System fidelity factor
$d_{est,e}$	Distance estimation error [m]
t_{max}	Depending on the context, t_{max} is either the time where the SFF becomes maximum, or the maximum time in an IR-UWB system level simulation [s]
$t_{p,max}$	Input pulse duration [s]
f_s	Sampling frequency [Hz]
r	Maximal path length [m]
v	Wave speed [m/s]
r	Distance between two antennas
$\mathbf{F}$	Radiation vector of an antenna [V/m]
F_θ	Radiation pattern θ-component [V/m]
F_ϕ	Radiation pattern ϕ-component [V/m]
$\mathbf{S}$	S parameter matrix
T_p	Pulse width [s]
B_{sig}	Significant bandwidth of the input pulse [Hz]
s_{sig}	Windowed input pulse
S_{sig}	Windowed spectrum of the input pulse
$\tau_{g,r}$	Relative group delay
μ_{SFF}	Mean system fidelity factor
BW	Bandwidth [Hz]

Symbols specific to on-chip antennas (part II)

η	Antenna efficiency
A	Antenna footprint [m^2]
g	Acceleration due to gravity, $g = 9.8$ m/s^2
ρ	Specific mass of material [kg/m^3]
ν	Poisson's ratio of material
E	Young's modulus of material [Pa]
σ_{th}	Thermal stress [N/m^2]
α	Thermal expansion coefficient [ppm/K]

List of Publications

Articles in international journals

- Q. Van den Brande, S. Lemey, J. Vanfleteren, and H. Rogier, "Highly Efficient Impulse-Radio Ultra-Wideband Cavity-Backed Slot Antenna in Stacked Air-Filled Substrate Integrated Waveguide Technology", *IEEE Transactions on Antennas and Propagation*, vol. 66, no. 5, pp. 2199–2209, 2018
- K. Minne, N. Macoir, J. Rossey, Q. Van den Brande, S. Lemey, J. Hoebeke, and E. De Poorter, "Experimental Evaluation of UWB Indoor Positioning for Indoor Track Cycling", *Sensors*, vol. 19, no. 9, 2019
- B. Van Herbruggen, B. Jooris, J. Rossey, M. Ridolfi, N. Macoir, Q. Van den Brande, S. Lemey, and E. De Poorter, "Wi-PoS: A Low-Cost, Open Source Ultra-Wideband (UWB) Hardware Platform with Long Range Sub-GHz Backbone", *Sensors*, vol. 19, no. 7, 2019
- Q. Van den Brande, S. Lemey, S. Cuyvers, S. Poelman, L. De Brabander, O. Caytan, L. Bogaert, I. Lima De Paula, S. Verstuyft, A. C. F. Reniers, B. Smolders, B. Kuyken, D. Vande Ginste, and H. Rogier, "A Hybrid Integration Strategy for Compact, Broadband, and Highly Efficient Millimeter-Wave On-Chip Antennas", *IEEE Antennas and Wireless Propagation Letters*, vol. 18, no. 11, pp. 2424–2428, 2019
- D. Van Baelen, Q. Van den Brande, S. Lemey, J. Verhaevert, and H. Rogier, "Foldable All-Textile Cavity-Backed Slot Antennas for Personal UWB Localization", *Radio Science*, vol. 55, no. 3, e2019RS006990, 2020, e2019RS006990 10.1029/2019RS006990
- Q. Van den Brande, S. Lemey, and H. Rogier, "Planar Sectoral Antenna for IR-UWB Localization With Minimal Range Estimation Biasing", *IEEE Antennas and Wireless Propagation Letters*, vol. 20, no. 2, pp. 135–139, 2021
- I. Lima de Paula, S. Lemey, D. Bosman, Q. Van den Brande, O. Caytan, J. Lambrecht, M. Cauwe, G. Torfs, and H. Rogier, "Cost-Effective High-Performance Air-Filled SIW Antenna Array for the Global 5G 26 GHz and 28 GHz Bands", *IEEE Antennas and Wireless Propagation Letters*, vol. 20, no. 2, pp. 194–198, 2021
- D. Van Baelen, N. Macoir, Q. Van den Brande, E. De Poorter, S. Lemey, J. Verhaevert, and H. Rogier, "Fully Flexible Textile Antenna-Backed Sensor Node for Body-Worn UWB Localization", *Sensors*, vol. 21, no. 5, 2021

Articles in conference proceedings

- P. Van Torre, Q. Van den Brande, J. Verhaevert, J. Vanfleteren, and H. Rogier, "Key Generation based on Fast Reciprocal Channel Estimation for Body-Worn Sensor Nodes", in *2017 11th European Conference on Antennas and Propagation (EUCAP)*, 2017, pp. 293–297
- Q. Van den Brande, P. Van Torre, J. Verhaevert, J. Vanfleteren, and H. Rogier, "Modular Transmitter and Receiver for Space-Time Coding", in *2017 11th European Conference on Antennas and Propagation (EUCAP)*, 2017, pp. 3305–3309
- Q. Van den Brande, S. Lemey, H. Rogier, and J. Vanfleteren, "Coupled Half-Mode Cavity-Backed Slot Antenna for IR-UWB in Air-Filled SIW Technology", in *2018 IEEE International Symposium on Antennas and Propagation USNC/URSI National Radio Science Meeting*, 2018, pp. 1269–1270
- A. Deroo, M. Huynen, H. Rogier, Q. Van den Brande, D. Vande Ginste, H.-W. Chan, and R.-B. Wu, "Reduction of Common-Mode Noise in Bent Differential Interconnects for PAM4 Signaling", in *2019 Electrical Design of Advanced Packaging and Systems (EDAPS)*, 2019, pp. 1–3
- S. Lemey, O. Caytan, Q. Van den Brande, I. L. d. Paula, L. Bogaert, H. Li, J. V. Kerrebrouck, A. C. F. Reniers, B. Smolders, J. Bauwelinck, P. Demeester, G. Torfs, D. Vande Ginste, S. Verstuyft, B. Kuyken, and H. Rogier, "Air-filled Substrate-Integrated Waveguide Technology for Broadband and Highly-Efficient Photonic-Enabled Antenna Systems", in *2020 XXXIIIrd General Assembly and Scientific Symposium of the International Union of Radio Science*, 2020, pp. 1–4

1 Introduction

1.1 Context

Throughout history, a number of key technologies have revolutionized society in such a profound way that mankind became dependent on it for continuous prosperity and economic growth. In 1765, the first industrial revolution was accelerated by James Watt and his invention of the Watt steam engine, thereby replacing agriculture with industry as the backbone of societal economy. At the end of the 19th century, the emergence of electricity was one of the key enablers for the massive amount of imperative inventions during the second industrial revolution, paving the way for innovations such as the telephone, the light bulb and the Alternating Current (AC) motor. By the second half of the 20th century, the conception of the transistor brought forth the development of integrated circuits, giving rise to an era of high-level automation during the third industrial revolution. Currently, the combination of the Internet-of-Things (IoT), Cyber-Physical Systems (CPSs) and big data analytics is disrupting the industrial landscape worldwide and, hence, these technologies are considered the primary facilitators of the next industrial revolution: Industry 4.0.

The integration of these technologies in existing industrial infrastructures brings into existence the concept of industrial CPSs or smart artifacts: products or machines that not only have the abilities to compute, communicate and control, but also have autonomy and sociality [1]. Leveraging large networks of CPSs, Cyber-Physical Production Systems (CPPS) will then enable smart products to organize, control and optimize their own production processes with minimal human interventions [2], thereby significantly enhancing transparency, productivity and efficiency of production processes [3]. In laymen terms: Industry 4.0 enables a world in which personalization and customization of any product is accessible to every customer, available in the blink of an eye and offered at an affordable price. Fur-

thermore, because the manufacturer can monitor and analyze the smart products throughout its complete life cycle, supply chain and production optimization can be automated, providing an unforeseen level of flexibility and adaptability. To put this into context: During the first lock-down of the COVID-19 pandemic, stores experienced an irrational demand for toilet paper, which manufacturers could not satisfy without major changes in their production process. Although a global toilet paper shortage was experienced, a framework for customer behavior analysis combined with flexible CPPS would have easily averted this issue.

With this convergence of the physical and virtual world in the form of CPPS, real-time asset tracking is imperative to realize a fully automated and reconfigurable smart factory [4]–[7]. Especially with the deployment of moving robots, drones and other autonomous vehicles [8], [9], highly accurate indoor Real-Time Locating System (RTLS) are becoming indispensable for the implementation of Industry 4.0. As satellite signals are attenuated and scattered by roofs, walls and other objects, indoor RTLS require alternative technological solutions to the widely adopted satellite-based Global Positioning System (GPS). Although many attempts have been made [4], [6], only the recent advancements in Impulse Radio Ultra-Wideband (IR-UWB) technology have accelerated the adoption of indoor RTLS by industry [6], [10]–[12]. The use of sub-nanosecond duration pulses in IR-UWB RTLS provides cm-level positional accuracy while featuring a high immunity to multipath effects and interference, commonly found in challenging IoT and Industry 4.0 environments [11]. As a result, novel applications emerge, such as, collision avoidance [13], automated production line optimization [14]–[16], material/component and production tracking [17], [18] and contact tracing [19] (currently more relevant than ever in the context of the ongoing COVID-19 pandemic).

Next, the explosive growth of industrial IoT devices, forming extensive networks of CPSs, imposes unseen requirements on the next generation Industrial Wireless Networks (IWNs). Especially applications as mobile assistance systems for human-machine-interaction, require these IWNs to satisfy a heterogeneous set of requirements, ranging from guaranteed Quality of Service (QoS), low end-to-end latency and high data-rate communication [8]. In terms of numbers, this translates to a reliability up to 99.999%, extremely low latencies below 1 ms and data rates up to 10 Gbps [20]. Furthermore, the virtualization of the physical factory in Industry 4.0 requires IWNs to be dynamically programmable for providing separate layers for different applications [20]. This is where 5G is considered to save the day [8], [20], [21]. Especially the Milimeter-Wave (mmWave) 5G frequency bands offer data rates up to several Gbps with high reliability, because of the available bandwidth and dense small cell networks, respectively [20], [22], [23]. As these mmWave networks can be managed by a Cloud Radio Access Network (C-RAN), dynamic network programming happens effortlessly [24]. Yet, although 5G is forming an adequate backbone for current Industry 4.0 applications, the envisioned bandwidth-hungry applications facilitated by Augmented/Virtual Reality (AR/VR) technology require data rates up to 100 Gbps, thereby pushing researchers to investigate possible technologies for next generation wireless sys-

tems [25]–[31].

1.2 Motivation

While the groundwork for fully-automated smart factories has been laid out, several technological challenges still prevent unleashing the full potential of Industry 4.0 and its impact on society [1], [21], [32]. This dissertation strives to address two critical physical layer challenges that inhibit the short-term advancement and the long-term potential of Industry 4.0. First, a system-oriented optimization framework is proposed to (1) investigate the impact of antennas in IR-UWB RTLS and (2) to realize robust and high-performance antenna systems for high-accuracy IR-UWB RTLS in an efficient and first-time-right manner. Second, novel highly efficient on-chip antenna technologies for 5G and beyond 5G applications have been analyzed. Moreover, in both cases, the potential of standard fabrication processes to realize highly efficient antennas is analyzed and discussed.

First, the development and optimization of robust and highly accurate IR-UWB RTLS are vital to promote adoption and to advance the further development of existing CPS applications [6]. Demonstrating the potential of industrial IoT in smart factories with these pilot application scenarios will usher in a true transformation of the industrial landscape where the paradigm shift of the fourth industrial revolution is embraced by both existing and new businesses [1]. However, the use of sub-nanosecond pulses in IR-UWB RTLS imposes a different set of design challenges compared to conventional narrowband RF-based RTLS. The Ultra-Wideband (UWB) spectrum of the pulses implies specific radiowave propagation characteristics, requiring the IR-UWB hardware to exhibit excellent performance in both the frequency and time domain [33]–[37]. Moreover, recent research has demonstrated the IR-UWB RTLS performance is not only influenced by the active electronics. The orientation specific pulse distortion and phase-center variations, induced by non-ideal space-, frequency- and time-domain characteristics of the transmit and receive antennas significantly impact the system accuracy and robustness [34], [38]–[41]. As a result, substantially different antenna topologies [42] demand dedicated system-level simulations to guarantee excellent RTLS performance. Furthermore, antenna design in harsh IoT and Industry 4.0 environments requires antenna optimization in the envisioned deployment scenarios, rather than in stand-alone free-space environments [43], [44]. To this end, two dedicated system-level metrics are defined: the System Fidelity Factor (SFF) and the Distance Estimation Error (DEE). The SFF characterizes the pulse distortion introduced by the antenna system [33], whereas the DEE quantifies the amount of ranging bias for different antenna orientations. A multi-objective optimization in which the SFF is maximized while minimizing the DEE and satisfying the imposed frequency-domain requirements then guarantees optimal IR-UWB RTLS performance in realistic deployment scenarios, imperative for current- and next-generation Industry 4.0 applications.

Second, to accommodate the need for extremely reliable, low-latency and high data-rate communication systems, next-generation wireless systems are considered key for the success of Industry 4.0. Specifically, the available bandwidth in the mmWave frequency bands of fifth-generation wireless networks (5G) is able to facilitate the high data-rate requirements of massive CPS networks for the coming years. However, to resolve the inherent drawback of mmWave communication, such as exceedingly unfavorable propagation characteristics [45], multi-antenna systems with adaptive beamforming will be indispensable [46], [47]. Fortunately, the reduced wavelength at those frequencies gives rise to smaller antenna footprints, facilitating highly integrated radio units containing both the RF front-end and the antenna on chip, thereby enhancing production yield and mitigating the large interconnect losses [48]–[55]. Nonetheless, the adverse electromagnetic material properties of bulk silicon substrates significantly inhibit the Antenna-on-Chip (AoC) efficiency and performance [51]. Furthermore, utmost care should be taken to prevent Electromagnetic Interference (EMI) issues, due to inadequate shielding of the mmWave front-end module [51]. When considering next-generation Industry 4.0 applications, such as mobile assistance systems for human-machine-interaction facilitated by AR/VR technology, beyond 5G wireless systems will be required to enable 100 Gbps wireless links. To this end, opportunities in the unlicensed THz frequency band are investigated. The available bandwidth (69 GHz) at 287 GHz is reported to support data rates of 100 Gbps and higher for distances up to a few hundred meters [56]. Similar to the mmWave frequency band, the signal experiences substantial frequency dependent atmospheric attenuation [30], [31], making high-gain or multi-antenna systems crucial. Moreover, poor microwave component performance and high interconnect, packaging and assembly losses [29], [57], [58] make the integration of the THz transceiver, beamforming networks and antenna array into a highly-integrated System-on-Chip (SoC) one of the most promising solutions for THz communication. However, the low radiation efficiency and narrowband behavior of on-chip antennas still impose significant limitations on the viability of on-chip antennas in THz SoC applications [58].

Finally, the virtualization of the physical factory requires an "always-on" user experience, providing non-stop connectivity to a massive network of CPSs [20]. As a result, energy efficiency is an essential part in any Industry 4.0 application [1], [20], [21]. Especially with the massive deployment of industrial IoT devices inside smart factories, marginal increases in energy efficiency result in large economic benefits. Furthermore, in the context of (beyond) 5G communication systems, energy efficiency optimization is critical to mitigate heat dissipation issues that are commonly encountered in highly-integrated SoCs [59]. Hence, the development of highly efficient antenna technologies for both IR-UWB RTLSs and mmWave/THz wireless communication applications is not only essential for Industry 4.0, but for the IoT in general [60], [61]. Yet, providing a high antenna efficiency over an ultra-wide bandwidth requires thoughtful operation principles, as most efficiency enhancing antenna technologies exhibit strictly narrowband behavior [62]. Additionally, the massive deployment of IoT devices in Industry 4.0 demands cost-effective fabrica-

tion technologies, such as standard Printed Circuit Board (PCB) and silicon process technology, while guaranteeing excellent antenna performance [60], [61].

1.3 Current state-of-the-art

The immense potential of Industry 4.0, both from an economical and societal perspective, has led to a joint effort of researchers worldwide to tackle the technical challenges described in Section 1.2. This section outlines the principal research results with respect to, on the one hand, highly-efficient IR-UWB antennas, optimized for precise indoor localization and, on the other hand, highly-efficient on-chip antenna technologies for 5G and beyond 5G wireless systems.

1.3.1 Robust and Highly-Efficient Antenna Systems for IR-UWB Localization in Industry 4.0 Applications

In order to develop highly-efficient antenna systems for precise IR-UWB localization, system-level performance needs to be assessed and optimized for metrics as the SFF and the DEE. However, no commercial tools currently exist to efficiently perform sytem-level simulations, which makes accurate and complete IR-UWB RTLS simulation very challenging. As a result, researchers have proposed dedicated simulation frameworks that facilitate system-level simulation of either the active electronics [35], [36] or the antenna link [38]–[41]. In [35] and [36], an UWB simulation framework is described that models the complete IR-UWB link in Agilent Advanced Design System (ADS). Although this provides a powerful tool for system-level hardware design, it fails to incorporate the effect of orientation specific antenna effects and, as such, is inadequate to design highly accurate IR-UWB RTLS. In [38]–[41], dedicated frameworks are proposed that jointly characterize the frequency, time and space domain of IR-UWB antenna systems. However, the frameworks don't specify the possibility to incorporate circuit simulations or measurements results to enable full-wave/circuit co-optimization and, thus, fail to accurately calculate system-level parameters.

Nevertheless, a plethora of antennas for IR-UWB RTLS have been proposed in literature [63]–[66]. Antenna systems simulated and measured in stand-alone free-space conditions easily demonstrate SFF values up to 90% [63], [64], [67]–[69]. However, the design of robust IR-UWB antennas with a high SFF in realistic deployment scenario's require significantly different antenna topologies [70]. In this regard, Substrate-Integrated-Waveguide (SIW) technology [71], [72] provides excellent features that enable outstanding antenna performance regardless of the integration platform. Yet, the inherent narrowband characteristics and limited energy efficiency of SIW structures still inhibit their potential for high-performance IR-UWB RTLSs [65], [72]–[74]. To address this issue, Air-Filled Substrate-Integrated-Waveguide (AFSIW) technology is often proposed as a scalable alternative to the conventional Dielectric-Filled Substrate-Integrated-Waveguide (DFSIW) technol-

ogy for next-generation antenna systems [75]–[85]. To implement AFSIW structures, several standard, low-cost fabrication technologies are available, such as PCB, bulk silicon and additive manufacturing technology. In [75]–[79], [81], [82], numerous AFSIW filters, phase shifters and antennas have been proposed, implemented in multilayer PCB technology. In [80], micromachining techniques of bulk silicon substrates are leveraged to implement an AFSIW slotted G-band horn antenna. Furthermore, recent advancements in additive manufacturing have shown great promise for 3-D printed AFSIW antennas, facilitating cost-effective and accessible fabrication technology while exhibiting excellent antenna performance [86]–[89]. In conclusion, AFSIW antennas outperform their DFSIW counterparts not only in terms of antenna efficiency and impedance bandwidth [83], [84], but also in cost effectiveness. Unfortunately, the system-level performance of AFSIW antennas for IR-UWB RTLSs found in literature is not yet assessed.

Next to minimizing the pulse distortion in a IR-UWB localization system by maximizing the SFF, antenna orientation induced ranging bias should be minimized to guarantee highly accurate RTLS performance. More specifically, the development of sector antennas with a minimal DEE over a sufficiently large Half-Power Beamwidth (HPBW) are vital to the success of IR-UWB RTLS in Industry 4.0. In [90], a hemispherical antenna is presented, achieving a HPBW larger than 90° and showing a fidelity factor of 80% in broadside. Unfortunately, a gain as low as -15 dBi is reported, rendering it unsuitable for the envisioned application scenario. In [91] and [92], SFFs up to 91% and 95% are reported, respectively. Furthermore, Van Baelen et. al. reports a DEE of 50 mm in [92], proving that a high SFF does not guarantee a low ranging estimation bias and that specific system-level optimization is required to optimize this parameter.

1.3.2 Highly Efficient On-Chip Antenna Technology for (beyond) 5G Wireless Systems

As stated in Section 1.2, the unfavorable electromagnetic material properties of bulk silicon substrates pose a critical threat on the viability of AoC technology for 5G mmWave antenna systems. Alternatively, the Antenna-in-Package (AiP) technology that is proposed to mitigate the aforementioned substrate losses by integrating the radiating antenna elements in low-loss packaging materials, still suffers from increased interconnect losses. Researchers have proposed a myriad of solutions to increase antenna efficiency, both for AoC [93]–[103] and AiP strategies [53], [55], [97]. Specifically for AoC, micromachined patch antennas show a lot of promise, reaching antenna efficiencies up to 95 % [50], [94], [95], [98]–[100], [104]. However, locally thinning the silicon substrate under the patch usually results in a larger antenna footprint. Furthermore, insufficient shielding [95] and/or susceptibility to EMI issues [93] were present as the micromachined cavities were not metallized. Another technique is the use of superstrates, enabling easy integration with 0.13 µm SiGe or Complementary Metal Oxide Semiconductor (CMOS) Radio Frequency (RF) front-ends [101]–[103]. However, reported antenna effi-

ciencies lower than 50 % render this technique ineffective for 5G mmWave antenna systems. As a result, AoC technology typically leads to a trade-off between antenna efficiency, bandwidth and antenna footprint. This is where AiP technology shows great promise to provide high antenna efficiencies over a ultra-wide bandwidth within a small antenna footprint [53], [55], [97]. Nonetheless, the high losses associated with long interconnects in AiP technology, inhibit its full adoption as a viable solution for highly-integrated mmWave antenna systems. As a result, the best of both integration strategies are combined in hybrid integration strategies, yielding high performance integrated antennas [52], [54] within a compact footprint. By implementing part of the antenna as an AoC and the other part with AiP technology, substrate losses are mitigated while eliminating the need for interconnects and, hence, significantly reducing overall losses.

When investigating next-generation on-chip antenna systems at Terahertz (THz) frequencies, the same challenges persist as in mmWave AoC. Moreover, because wavelengths are an order of magnitude smaller than at mmWave frequencies, interconnect losses are significantly higher and render AiP technology unsuitable at THz frequencies. To this end, several techniques have been proposed in literature to resolve the low efficiency and narrowband issues [29], [57], [105]. First, lens loaded antennas exhibit a large antenna gain, low side lobe levels and minimal cross polarization [105]. Nevertheless, the complex fabrication methods, large antenna footprint and even radiation pattern distortion due to temperature fluctuations, limit their value in steerable multi-antenna systems [106]. Next, the high efficiency associated with dielectric-resonator-based systems, which achieve an antenna efficiency of 80% and a gain of 10 dBi at 340 GHz, shows great promise [58]. Unfortunately, their use in THz on-chip antenna systems is compromised by their narrowband behavior and added fabrication complexity. CMOS THz antennas have been explored as well [107], [108], but they exhibit radiation efficiencies of maximally 54%. Finally, similar to mmWave AoC technology, micro-machining techniques have been used to realize SIW on-chip antennas by filling metalized cavities with low-loss material to enhance radiation efficiency and impedance bandwidth simultaneously [109], [110]. In [109], a patch antenna and 1x4 linear array are reported, fabricated using Benzocyclobutene (BCB)-filled cavities, showing an impedance bandwidth of 2.8 GHz at 100 GHz, a maximum radiation efficiency of 79.6% and a gain of 6.7 dBi and 13 dBi for single antenna and array implementations, respectively. Similarly, in [110] an impedance bandwidth of 4.5% and a gain of 6.4 dBi are obtained at 135 GHz.

1.4 Own contributions and outline

This dissertation focuses on resolving two critical physical-layer inhibitors of the large-scale acceleration of Industry 4.0. In the first part, highly efficient, robust IR-UWB antennas in AFSIW technology are investigated for indoor RTLS applications. By leveraging an in-house developed system-oriented full-wave/circuit

co-optimization framework, orientation-specific pulse distortion and ranging bias errors are minimized, even in realistic Industry 4.0 deployment scenarios. In the second part, novel AFSIW technologies are proposed to mitigate the critical drawbacks of mmWave and THz on-chip antennas, thereby facilitating extremely high antenna efficiencies over a large impedance bandwidth, within a compact footprint.

1.4.1 Robust and Highly-Efficient Antenna Systems for IR-UWB Localization in Industry 4.0 Applications

The first part is divided into three chapters. Chapter 2 describes a novel, modular full-wave/circuit IR-UWB co-optimization framework that facilitates highly accurate and efficient system-level optimization of IR-UWB systems. The framework allows to efficiently integrate the standalone simulation results of each IR-UWB component in the RF link to characterize the complete IR-UWB system performance, thereby obtaining a modular architecture that facilitates light-weight simulations with great design flexibility. This strategy also enables measurement results to be included in the co-optimization framework. Furthermore, the framework proposed in [37] is extended to allow system-level optimization, based on time-domain results. Hence, the IR-UWB RTLS performance can be assessed in terms of the SFF and the DEE. A series of dedicated time-domain measurements in an anechoic chamber are performed to validate the obtained simulation results, showing a good agreement between simulations and measurements. Additionally, its performance is benchmarked against commercial solvers, showing a significant improvement in computing time and required memory.

In Chapter 3, a highly efficient IR-UWB coupled half-mode cavity-backed slot antenna in stacked AFSIW technology is reported. The required antenna characteristics are obtained by leveraging the coupled half-mode technique in a cavity-backed slot antenna topology [111]. Furthermore, to cater to the demands for precision IR-UWB localization in Industry 4.0, the antenna is realized in AFSIW technology. An AFSIW cavity is realized by sandwiching two milled FR-4 substrates between two *RO*4350*B*® laminates, containing the slot and ground plane, respectively. The cavity sidewalls are fully metalized by means of edge plating, thereby shielding the electromagnetic fields from the low-cost and lossy FR-4 substrates. A multi-objective optimization, performed in both the frequency and time domains, is used to obtain outstanding IR-UWB characteristics, such as a very high SFF and a minimal relative group delay. As a result, pulse distortion is minimized and time-of-arrival variations satisfy the requirements for precision IR-UWB RTLS. Moreover, the antenna is measured in a realistic hostile environment to validate robust ranging performance. Furthermore, owing to its low-cost fabrication process and its topology, which allows for seamless integration with the active IR-UWB electronics, the proposed antenna is suitable for cost-effective mass production.

Chapter 4 describes a planar sectoral coupled Planar Inverted-F Antenna (PIFA) for IR-UWB localization, operating in the [3.2448 – 4.7424] GHz band. It com-

fortably covers channels 1 through 4 of the IEEE 802.15.4a-2011 standard [112], thereby facilitating a wide range of Industry 4.0 applications. Rigorous system-level optimization, in both the frequency and time domains, results in an UWB coupled PIFA antenna, similar to the narrowband antenna in [113], exhibiting a large HPBW and a minimal DEE within that HPBW. The antenna performance is validated by both frequency- and time-domain measurements, thereby confirming the potential of the proposed antenna for IR-UWB indoor localization systems.

1.4.2 Highly-Efficient On-Chip Antenna Technology for 5G and beyond 5G Wireless Systems

The second part is divided into two chapters. In Chapter 5, a novel hybrid integration strategy for compact, broadband and highly efficient mmWave on-chip antennas is demonstrated. A highly-efficient hybrid on-chip antenna is realized, operating in the [27.5-29.5] GHz band, implementing a cavity-backed stacked patch antenna topology in AFSIW technology. A hybrid on-chip approach is obtained by placing the radiating stacked patch elements on a *RO*4350*B*® laminate, supporting the chip which implements the antenna feed and a metallized air-filled cavity. By exciting the antenna via an aperture in the cavity ground plane, the antenna feed can be integrated with the active electronics, while the radiating elements can be implemented on low-loss substrates without any interconnect losses. As a result, unprecedented overall AoC/AiP performance is achieved, showing a measured -10 dB-bandwidth of 3.7 GHz, a maximal gain of 7.3 dBi at 28.5 GHz and a total antenna efficiency larger than 90 % in the complete [27.5-29.5] GHz frequency band. Moreover, an antenna footprint of 5.0 mm × 5.0 mm is obtained by leveraging mode-bifurcation in a stacked-patch configuration. Furthermore, EMI issues and mutual coupling between neighboring antenna elements in multi-antenna systems are reduced because the air-filled cavity sidewalls are metallized.

In Chapter 6, a polymer-enabled AFSIW technology for highly-efficient, broadband on-chip THz antenna systems is presented, as a key enabler towards a low-cost and highly-integrated SoC framework for THz communication. A thin, low-loss polymer superstrate is suspended on top of an AFSIW cavity, implemented in a standard, low-cost silicon substrate, thereby obtaining frequency-independent antenna efficiencies over 90%. Again, mode-bifurcation is leveraged to achieve an ultra-wide impedance bandwidth in a compact antenna footprint. However, as a stacked-patch topology is not feasible in the proposed antenna technology, a coupled cavity-backed slot antenna with exponentially tapered feed and modified slot is utilized. As a result, a unit antenna element is realized, exhibiting an impedance bandwidth of 107 GHz at 300 GHz, a maximal gain of 5.79 dBi at 321.84 GHz and a HPBW higher than 75° over the complete frequency band of interest. Finally, the array performance is demonstrated by means of a 1x4 linear antenna array, implemented using the realized unit antenna element, and shows grating-lobe free beam-steering capabilities up to 30°.

References

[1] S. Wang, J. Wan, D. Li, and C. Zhang, "Implementing Smart Factory of Industrie 4.0: An Outlook", *International Journal of Distributed Sensor Networks*, vol. 12, no. 1, p. 3 159 805, 2016.

[2] D. Preuveneers and E. Ilie-Zudor, "The Intelligent Industry of the Future: A Survey on Emerging Trends, Research Challenges and Opportunities in Industry 4.0", *Journal of Ambient Intelligence and Smart Environments*, vol. 9, no. 3, pp. 287–298, 2017.

[3] E. Ilie-Zudor, A. Ekárt, Z. Kemeny, C. Buckingham, P. Welch, and L. Monostori, "Advanced Predictive-Analysis-Based Decision Support for Collaborative Logistics Networks", *Supply Chain Management: An International Journal*, 2015.

[4] A. Franko, G. Vida, and P. Varga, "Reliable Identification Schemes for Asset and Production Tracking in Industry 4.0", *Sensors*, vol. 20, no. 13, 2020.

[5] C. Hegedus, A. Franko, and P. Varga, "Asset and Production Tracking through Value Chains for Industry 4.0 using the Arrowhead Framework", in *2019 IEEE International Conference on Industrial Cyber Physical Systems (ICPS)*, 2019, pp. 655–660.

[6] A. Racz-Szabo, T. Ruppert, L. Bantay, A. Locklin, L. Jakab, and J. Abonyi, "Real-Time Locating System in Production Management", *Sensors*, vol. 20, no. 23, 2020.

[7] B. J. Silva and G. P. Hancke, "Practical Challenges of IR-UWB based Ranging in Harsh Industrial Environments", in *2015 IEEE 13th International Conference on Industrial Informatics (INDIN)*, 2015, pp. 618–623.

[8] M. Gundall, M. Strufe, H. D. Schotten, P. Rost, C. Markwart, R. Blunk, A. Neumann, J. GrieSSbach, M. Aleksy, and D. Wübben, "Introduction of a 5G-Enabled Architecture for the Realization of Industry 4.0 Use Cases", *IEEE Access*, vol. 9, pp. 25 508–25 521, 2021.

[9] R. Sell, A. Rassolkin, R. Wang, and T. Otto, "Integration of Autonomous Vehicles and Industry 4.0", *Proceedings of the Estonian Academy of Sciences*, vol. 68, pp. 389–394, Dec. 2019.

[10] A. D. Preter, G. Goysens, J. Anthonis, J. Swevers, and G. Pipeleers, "Range Bias Modeling and Autocalibration of an UWB Positioning System", in *2019 International Conference on Indoor Positioning and Indoor Navigation (IPIN)*, 2019, pp. 1–8.

[11] S. Jiang, M. J. Skibniewski, Y. Yuan, C. Sun, and Y. Lu, "Ultra-Wide Band Applications in Industry: A Critical Review", *Journal of Civil Engineering and Management*, vol. 17, no. 3, pp. 437–444, 2011.

[12] S. Novoselov and O. Sychova, “Using Wireless Technology for Managing Distributed Industrial Automation Objects within the Concept of Industry 4.0”, in *2019 IEEE International Scientific-Practical Conference Problems of Infocommunications, Science and Technology (PIC S T)*, 2019, pp. 580–584.

[13] C. Zhang and A. Hammad, “Multiagent Approach for Real-Time Collision Avoidance and Path Replanning for Cranes”, *Journal of Computing in Civil Engineering*, vol. 26, Nov. 2012.

[14] T. Ruppert and J. Abonyi, “Industrial Internet of Things based cycle time control of assembly lines”, Jan. 2018, pp. 1–4.

[15] ——, “Software Sensor for Activity-Time Monitoring and Fault Detection in Production Lines”, *Sensors*, vol. 18, no. 7, 2018.

[16] D. Gyulai, A. Pfeiffer, and J. Bergmann, “Analysis of Asset Location Data to Support Decisions in Production Management and Control”, *Procedia CIRP*, vol. 88, pp. 197–202, Jan. 2020.

[17] V. Barral, P. Suarez-Casal, C. J. Escudero, and J. A. Garcia-Naya, “Multi-Sensor Accurate Forklift Location and Tracking Simulation in Industrial Indoor Environments”, *Electronics*, vol. 8, no. 10, 2019.

[18] Z. Silvia, C. Martina, S. Fabio, and P. Alessandro, “Ultra Wide Band Indoor Positioning System: Analysis and Testing of an IPS Technology”, *IFAC-PapersOnLine*, vol. 51, no. 11, pp. 1488–1492, 2018, 16th IFAC Symposium on Information Control Problems in Manufacturing INCOM 2018.

[19] T. R. Hellmich, C. M. Clements, N. El-Sherif, K. S. Pasupathy, D. M. Nestler, A. Boggust, V. K. Ernste, G. Marisamy, K. R. Koenig, and M. S. Hallbeck, “Contact Tracing with a Real-Time Location System: A Case Study of Increasing Relative Effectiveness in an Emergency Department”, *American journal of infection control*, vol. 45, no. 12, pp. 1308–1311, 2017.

[20] S. K. Rao and R. Prasad, “Impact of 5G Technologies on Industry 4.0”, *Wireless personal communications*, vol. 100, no. 1, pp. 145–159, 2018.

[21] D. Sinha and R. Roy, “Reviewing Cyber-Physical System as a Part of Smart Factory in Industry 4.0”, *IEEE Engineering Management Review*, vol. 48, no. 2, pp. 103–117, 2020.

[22] A. Gupta and R. K. Jha, “A Survey of 5G Network: Architecture and Emerging Technologies”, *IEEE Access*, vol. 3, 2015.

[23] Z. Pi, J. Choi, and R. Heath, “Millimeter-Wave Gigabit Broadband Evolution toward 5G: Fixed Access and Backhaul”, *IEEE Communications Magazine*, vol. 54, no. 4, pp. 138–144, 2016.

[24] P. Rost, C. J. Bernardos, A. De Domenico, M. Di Girolamo, M. Lalam, A. Maeder, D. Sabella, and D. Wübben, “Cloud Technologies for Flexible 5G Radio Access Networks”, *IEEE Communications Magazine*, vol. 52, no. 5, pp. 68–76, 2014.

[25] G. Berardinelli, N. H. Mahmood, I. Rodriguez, and P. Mogensen, “Beyond 5G Wireless IRT for Industry 4.0: Design Principles and Spectrum Aspects”, in *2018 IEEE Globecom Workshops (GC Wkshps)*, 2018, pp. 1–6.

[26] P. Fraga-Lamas, T. M. FernáNdez-CaraméS, S. Blanco-Novoa, and M. A. Vilar-Montesinos, “A Review on Industrial Augmented Reality Systems for the Industry 4.0 Shipyard”, *IEEE Access*, vol. 6, pp. 13 358–13 375, 2018.

[27] V. Paelke, “Augmented Reality in the Smart Factory: Supporting Workers in an Industry 4.0. Environment”, in *Proceedings of the 2014 IEEE Emerging Technology and Factory Automation (ETFA)*, 2014, pp. 1–4.

[28] M. Saad, C. F. Bader, J. Palicot, Y. Corre, G. Gougeon, and J.-B. Doré, “Beyond-5G Wireless Tbps Scenarios and Requirements”, Ph.D. dissertation, ANR-BRAVE, 2018.

[29] Z. Chen, X. Ma, B. Zhang, Y. Zhang, Z. Niu, N. Kuang, W. Chen, L. Li, and S. Li, “A Survey on Terahertz Communications”, *China Communications*, vol. 16, no. 2, pp. 1–35, 2019.

[30] T. S. Rappaport, Y. Xing, O. Kanhere, S. Ju, A. Madanayake, S. Mandal, A. Alkhateeb, and G. C. Trichopoulos, “Wireless Communications and Applications Above 100 GHz: Opportunities and Challenges for 6G and Beyond”, *IEEE Access*, vol. 7, pp. 78 729–78 757, 2019.

[31] H.-J. Song and T. Nagatsuma, “Present and Future of Terahertz Communications”, *IEEE Transactions on Terahertz Science and Technology*, vol. 1, no. 1, pp. 256–263, 2011.

[32] A. Zeid, S. Sundaram, M. Moghaddam, S. Kamarthi, and T. Marion, “Interoperability in Smart Manufacturing: Research Challenges”, *Machines*, vol. 7, no. 2, 2019.

[33] G. Quintero, J. Zurcher, and A. K. Skrivervik, “System Fidelity Factor: A New Method for Comparing UWB Antennas”, *IEEE Transactions on Antennas and Propagation*, vol. 59, no. 7, pp. 2502–2512, 2011.

[34] M. R. Mahfouz, C. Zhang, B. C. Merkl, M. J. Kuhn, and A. E. Fathy, “Investigation of High-Accuracy Indoor 3-D Positioning Using UWB Technology”, *IEEE Transactions on Microwave Theory and Techniques*, vol. 56, no. 6, pp. 1316–1330, 2008.

[35] M. J. Kuhn, C. Zhang, S. Lin, M. R. Mahfouz, and A. E. Fathy, “A System Level Design Approach to UWB Localization”, in *2009 IEEE MTT-S International Microwave Symposium Digest*, 2009, pp. 1409–1412.

[36] M. J. Kuhn, M. R. Mahfouz, C. Zhang, B. C. Merkl, and A. E. Fathy, “A System-Level Simulation Framework for UWB Localization”, *IEEE Transactions on Microwave Theory and Techniques*, vol. 58, no. 12, pp. 3527–3537, 2010.

[37] T. Cuyckens and H. Rogier, "Framework for the Simulation of Wireless Power Transmission over Ultra Wide Band Links in Multipath Propagation Environments in the Vicinity of the Human Body", *International Journal of Numerical Modelling: Electronic Networks, Devices and Fields*, vol. 29, no. 3, pp. 364–379, 2016.

[38] A. Sibille, "A Framework for Analysis of Antenna Effects in UWB Communications", in *2005 IEEE 61st Vehicular Technology Conference*, vol. 1, 2005, 48–52 Vol. 1.

[39] A. O. Boryssenko and D. H. Schaubert, "Antenna Link Transfer Function Factorization Applied to Optimized Channel Design", *IEEE Transactions on Antennas and Propagation*, vol. 54, no. 10, pp. 2878–2889, 2006.

[40] X. Qing, Z. N. Chen, and M. Y. W. Chia, "Characterization of Ultrawideband Antennas using Transfer Functions", *Radio Science*, vol. 41, no. 01, pp. 1–10, 2006.

[41] A. E. Tan, M. Y. Chia, K. K. Chan, and K. Rambabu, "Modeling the Transient Radiated and Received Pulses of Ultra-Wideband Antennas", *IEEE Transactions on Antennas and Propagation*, vol. 61, no. 1, pp. 338–345, 2013.

[42] W. Wiesbeck, G. Adamiuk, and C. Sturm, "Basic Properties and Design Principles of UWB Antennas", *Proceedings of the IEEE*, vol. 97, no. 2, pp. 372–385, 2009.

[43] S. Lemey and H. Rogier, "SIW Textile Antennas as a novel Technology for UWB RFID tags", in *2014 IEEE RFID-TA*, Tampere, Finland, Sept. 8-9, 2014, pp. 256–260.

[44] V. Sipal, M. John, D. Neirynck, M. McLaughlin, and M. Ammann, "Advent of Practical UWB Localization: (R)Evolution in UWB Antenna Research", in *The 8th European Conference on Antennas and Propagation (EuCAP 2014)*, The Hague, The Netherlands, 6-11 Apr. 2014, pp. 1561–1565.

[45] T. S. Rappaport, G. R. MacCartney, M. K. Samimi, and S. Sun, "Wideband Millimeter-Wave Propagation Measurements and Channel Models for Future Wireless Communication System Design", *IEEE Transactions on Communications*, vol. 63, no. 9, pp. 3029–3056, 2015.

[46] T. Cameron, "5G - The Microwave Perspective", *Analog Devices*, pp. 1–4, 2015.

[47] M. Y. Frankel, P. J. Matthews, and R. D. Esman, "Practical Optical Beamforming Networks", *Optical and Quantum Electronics*, vol. 30, pp. 1033–1050, 1998.

[48] W. Shin, B. Ku, O. Inac, Y. Ou, and G. M. Rebeiz, "A 108-114 GHz 4×4 Wafer-Scale Phased Array Transmitter with High-Efficiency On-Chip Antennas", *IEEE Journal of Solid-State Circuits*, vol. 48, no. 9, pp. 2041–2055, 2013.

[49] B. Ku, O. Inac, M. Chang, H. Yang, and G. M. Rebeiz, "A High-Linearity 76-85-GHz 16-Element 8-Transmit/8-Receive Phased-Array Chip with High Isolation and Flip-Chip Packaging", *IEEE Transactions on Microwave Theory and Techniques*, vol. 62, no. 10, pp. 2337–2356, 2014.

[50] Y. Liu, A. Agrawal, and A. Natarajan, "Millimeter-Wave IC-Antenna Cointegration for Integrated Transmitters and Receivers", *IEEE Antennas and Wireless Propagation Letters*, vol. 15, pp. 1848–1852, 2016.

[51] Y. P. Zhang and D. Liu, "Antenna-on-Chip and Antenna-in-Package Solutions to Highly Integrated Millimeter-Wave Devices for Wireless Communications", *IEEE Transactions on Antennas and Propagation*, vol. 57, no. 10, pp. 2830–2841, 2009.

[52] J. A. Zevallos Luna, L. Dussopt, and A. Siligaris, "Hybrid On-Chip/In-Package Integrated Antennas for Millimeter-Wave Short-Range Communications", *IEEE Transactions on Antennas and Propagation*, vol. 61, no. 11, pp. 5377–5384, 2013.

[53] Y. P. Zhang, M. Sun, D. Liu, and Y. Lu, "Dual Grid Array Antennas in a Thin-Profile Package for Flip-Chip Interconnection to Highly Integrated 60-GHz Radios", *IEEE Transactions on Antennas and Propagation*, vol. 59, no. 4, pp. 1191–1199, 2011.

[54] Y. Song, K. Kang, Y. Tian, Y. Wu, Z. Li, Y. Guo, Y. Ban, J. Liu, X. Tang, H. Liu, and J. Yang, "A Hybrid Integrated High-Gain Antenna with an On-Chip Radiator Backed by Off-Chip Ground for System-on-Chip Applications", *IEEE Transactions on Components, Packaging and Manufacturing Technology*, vol. 7, no. 1, pp. 114–122, 2017.

[55] H. Kim, B. Park, S. Song, T. Moon, S. Kim, J. Kim, J. Chang, and Y. Ho, "A 28-GHz CMOS Direct Conversion Transceiver with Packaged2 × 4Antenna Array for 5G Cellular System", *IEEE Journal of Solid-State Circuits*, vol. 53, no. 5, pp. 1245–1259, 2018.

[56] V. Petrov, T. Kurner, and I. Hosako, "IEEE 802.15.3d: First Standardization Efforts for Sub-Terahertz Band Communications toward 6G", *IEEE Communications Magazine*, vol. 58, no. 11, pp. 28–33, 2020.

[57] X. Fu, F. Yang, C. Liu, X. Wu, and T. J. Cui, "Terahertz Beam Steering Technologies: From Phased Arrays to Field-Programmable Metasurfaces", *Advanced Optical Materials*, vol. 8, no. 3, p. 1 900 628, 2020.

[58] X.-D. Deng, Y. Li, C. Liu, W. Wu, and Y.-Z. Xiong, "340 GHz On-Chip 3-D Antenna With 10 dBi Gain and 80Radiation Efficiency", *IEEE Transactions on Terahertz Science and Technology*, vol. 5, no. 4, pp. 619–627, 2015.

[59] A. V. Lopez, A. Chervyakov, G. Chance, S. Verma, and Y. Tang, "Opportunities and Challenges of mmWave NR", *IEEE Wireless Communications*, vol. 26, no. 2, pp. 4–6, 2019.

[60] S. Lemey, T. Castel, P. V. Torre, T. Vervust, J. Vanfleteren, P. Demeester, D. V. Ginste, and H. Rogier, "Threefold Rotationally Symmetric SIW Antenna Array for Ultra-Short-Range MIMO Communication", *IEEE Transactions on Antennas and Propagation*, vol. 64, no. 5, pp. 1689–1699, 2016.

[61] O. Caytan, S. Lemey, S. Agneessens, D. Vande Ginste, P. Demeester, C. Loss, R. Salvado, and H. Rogier, "Half-Mode Substrate-Integrated-Waveguide Cavity-Backed Slot Antenna on Cork Substrate", *IEEE Antennas and Wireless Propagation Letters*, vol. 15, pp. 162–165, 2016.

[62] A. H. Abdelgwad, "Microstrip Patch Antenna Enhancement Techniques", *International Journal of Electronics and Communication Engineering*, vol. 12, no. 10, pp. 703–708, 2018.

[63] L. I. Balderas, A. Reyna, M. A. Panduro, C. Del Rio, and A. R. Gutiérrez, "Low-Profile Conformal UWB Antenna for UAV Applications", *IEEE Access*, vol. 7, pp. 127 486–127 494, 2019.

[64] J. Liu, K. P. Esselle, S. G. Hay, and S. Zhong, "Effects of Printed UWB Antenna Miniaturization on Pulse Fidelity and Pattern Stability", *IEEE Transactions on Antennas and Propagation*, vol. 62, no. 8, pp. 3903–3910, 2014.

[65] D. Van Baelen, Q. Van den Brande, S. Lemey, J. Verhaevert, and H. Rogier, "Foldable All-Textile Cavity-Backed Slot Antennas for Personal UWB Localization", *Radio Science*, vol. 55, no. 3, e2019RS006990, 2020, e2019RS006990 10.1029/2019RS006990.

[66] T. Saeidi, I. Ismail, W. P. Wen, A. R. Alhawari, and A. Mohammadi, "Ultra-Wideband Antennas for Wireless Communication Applications", *International Journal of Antennas and Propagation*, vol. 2019, 2019.

[67] B. Mohamadzade, R. B. V. B. Simorangkir, R. M. Hashmi, and A. Lalbakhsh, "A Conformal Ultrawideband Antenna With Monopole-Like Radiation Patterns", *IEEE Transactions on Antennas and Propagation*, vol. 68, no. 8, pp. 6383–6388, 2020.

[68] S. R. Emadian, J. Ahmadi-Shokouh, C. Ghobadi, and J. Nourinia, "Study on Frequency and Impulse Response of novel Triple Band Notched UWB Antenna in Indoor Environments", *AEU - International Journal of Electronics and Communications*, vol. 96, pp. 93–106, 2018.

[69] S. Ullah, C. Ruan, M. S. Sadiq, T. U. Haq, and W. He, "High Efficient and Ultra Wide Band Monopole Antenna for Microwave Imaging and Communication Applications", *Sensors*, vol. 20, no. 1, 2020.

[70] B. J. Silva and G. P. Hancke, "Practical Challenges of IR-UWB based Ranging in Harsh Industrial Environments", in *2015 IEEE 13th International Conference on Industrial Informatics (INDIN)*, IEEE, 2015, pp. 618–623.

[71] M. Bozzi, L. Perregrini, K. Wu, and P. Arcioni, "Current and Future Research Trends in Substrate Integrated Waveguide Technology", *Radioengineering*, vol. 18, no. 2, 2009.

[72] M. Bozzi, A. Georgiadis, and K. Wu, “Review of Substrate-Integrated Waveguide Circuits and Antennas”, English, *IET Microwaves, Antennas Propagation*, vol. 5, 909–920(11), 8 2011.

[73] D. Van Baelen, N. Macoir, Q. Van den Brande, E. De Poorter, S. Lemey, J. Verhaevert, and H. Rogier, “Fully Flexible Textile Antenna-Backed Sensor Node for Body-Worn UWB Localization”, *Sensors*, vol. 21, no. 5, 2021.

[74] S. Lemey and H. Rogier, “SIW Textile Antennas as a Novel Technology for UWB RFID Tags”, in *2014 IEEE RFID Technology and Applications Conference (RFID-TA)*, 2014, pp. 256–260.

[75] A. Belenguer, H. Esteban, and V. E. Boria, “Novel Empty Substrate Integrated Waveguide for High-Performance Microwave Integrated Circuits”, *IEEE Transactions on Microwave Theory and Techniques*, vol. 62, no. 4, pp. 832–839, 2014.

[76] J. V. Morro, A. RodrÃguez, A. Belenguer, H. Esteban, and V. Boria, “Multilevel Transition in Empty Substrate Integrated Waveguide”, *Electronics Letters*, vol. 52, no. 18, pp. 1543–1544, 2016.

[77] A. Belenguer, J. L. Cano, H. Esteban, E. Artal, and V. E. Boria, “Empty Substrate Integrated Waveguide Technology for E Plane High-Frequency and High-Performance Circuits”, *Radio Science*, vol. 52, no. 1, pp. 49–69, 2017.

[78] F. Parment, A. Ghiotto, T. P. Vuong, J. M. Duchamp, and K. Wu, “Ka-band Compact and High-Performance Bandpass Filter based on Multilayer Air-Filled SIW”, *Electronics Letters*, vol. 53, no. 7, pp. 486–488, 2017.

[79] ——, “Double Dielectric Slab-Loaded Air-Filled SIW Phase Shifters for High-Performance Millimeter-Wave Integration”, *IEEE Transactions on Microwave Theory and Techniques*, vol. 64, no. 9, pp. 2833–2842, 2016.

[80] J. W. Digby, C. E. McIntosh, G. M. Parkhurst, B. M. Towlson, S. Hadjiloucas, J. W. Bowen, J. M. Chamberlain, R. D. Pollard, R. E. Miles, D. P. Steenson, L. S. Karatzas, N. J. Cronin, and S. R. Davies, “Fabrication and Characterization of Micromachined Rectangular Waveguide Components for Use at Millimeter-Wave and Terahertz Frequencies”, *IEEE Transactions on Microwave Theory and Techniques*, vol. 48, no. 8, pp. 1293–1302, 2000.

[81] J. Mateo, A. M. Torres, A. Belenguer, and A. L. Borja, “Highly Efficient and Well-Matched Empty Substrate Integrated Waveguide H-Plane Horn Antenna”, *IEEE Antennas and Wireless Propagation Letters*, vol. 15, pp. 1510–1513, 2016.

[82] F. Bigelli, D. Mencarelli, M. Farina, G. Venanzoni, P. Scalmati, C. Renghini, and A. Morini, “Design and Fabrication of a Dielectricless Substrate-Integrated Waveguide”, *IEEE Transactions on Components, Packaging and Manufacturing Technology*, vol. 6, no. 2, pp. 256–261, 2016.

[83] F. Parment, A. Ghiotto, T. P. Vuong, J. M. Duchamp, and K. Wu, “Millimetre-Wave Air-Filled Substrate Integrated Waveguide Slot Array Antenna”, *Electronics Letters*, vol. 53, no. 11, pp. 704–706, 2017.

[84] A. Ghiotto, F. Parment, T. P. Vuong, and K. Wu, "Millimeter-Wave Air-Filled SIW Antipodal Linearly Tapered Slot Antenna", *IEEE Antennas and Wireless Propagation Letters*, vol. 16, pp. 768–771, 2017.

[85] F. Parment, A. Ghiotto, T. P. Vuong, J. M. Duchamp, and K. Wu, "Air-Filled Substrate Integrated Waveguide for Low-Loss and High Power-Handling Millimeter-Wave Substrate Integrated Circuits", *IEEE Transactions on Microwave Theory and Techniques*, vol. 63, no. 4, pp. 1228–1238, 2015.

[86] M. DAuria, W. J. Otter, J. Hazell, B. T. W. Gillatt, C. Long-Collins, N. M. Ridler, and S. Lucyszyn, "3-D Printed Metal-Pipe Rectangular Waveguides", *IEEE Transactions on Components, Packaging and Manufacturing Technology*, vol. 5, no. 9, pp. 1339–1349, 2015.

[87] B. Zhang, Z. Zhan, Y. Cao, H. Gulan, P. Linnér, J. Sun, T. Zwick, and H. Zirath, "Metallic 3-D Printed Antennas for Millimeter- and Submillimeter Wave Applications", *IEEE Transactions on Terahertz Science and Technology*, vol. 6, no. 4, pp. 592–600, 2016.

[88] F. Bongard, M. Gimersky, S. Doherty, X. Aubry, and M. Krummen, "3D-printed Ka-Band Waveguide Array Antenna for Mobile SATCOM Applications", in *2017 11th European Conference on Antennas and Propagation (EUCAP)*, 2017, pp. 579–583.

[89] J. Shen and D. S. Ricketts, "Additive Manufacturing of Complex Millimeter-Wave Waveguides Structures Using Digital Light Processing", *IEEE Transactions on Microwave Theory and Techniques*, vol. 67, no. 3, pp. 883–895, 2019.

[90] Y. Li, X. Yang, Z. Li, L. Wang, and H. Yang, "A Unidirectional Cylindrical Conformal Monopole Antenna Designed for Impulse Radar System", *IEEE Antennas and Wireless Propagation Letters*, vol. 10, pp. 1397–1400, 2011.

[91] M. Li and K. Luk, "A Differential-Fed UWB Antenna Element With Unidirectional Radiation", *IEEE Transactions on Antennas and Propagation*, vol. 64, no. 8, pp. 3651–3656, 2016.

[92] D. Van Baelen, Q. Van den Brande, S. Lemey, J. Verhaevert, and H. Rogier, "Foldable All-Textile Cavity-Backed Slot Antennas for Personal UWB Localization", *Radio Science*, vol. 55, no. 3, e2019RS006990, 2020, e2019RS006990 10.1029/2019RS006990.

[93] E. Ojefors, H. Kratz, K. Grenier, R. Plana, and A. Rydberg, "Micromachined Loop Antennas on Low Resistivity Silicon Substrates", *IEEE Transactions on Antennas and Propagation*, vol. 54, no. 12, pp. 3593–3601, 2006.

[94] G. P. Gauthier, J. Raskin, L. P. B. Katehi, and G. M. Rebeiz, "A 94-GHz Aperture-Coupled Micromachined Microstrip Antenna", *IEEE Transactions on Antennas and Propagation*, vol. 47, no. 12, pp. 1761–1766, 1999.

[95] H. Chu, Y. Guo, T. Lim, Y. M. Khoo, and X. Shi, "135-GHz Micromachined On-Chip Antenna and Antenna Array", *IEEE Transactions on Antennas and Propagation*, vol. 60, no. 10, pp. 4582–4588, 2012.

[96] P. Liu, L. Chang, Y. Li, Z. Zhang, S. Wang, and Z. Feng, "A Millimeter-Wave Micromachined Air-Filled Slot Antenna fed by Patch", *IEEE Transactions on Components, Packaging and Manufacturing Technology*, vol. 7, no. 10, pp. 1683–1690, 2017.

[97] W. T. Khan, A. Cagri Ulusoy, G. Dufour, M. Kaynak, B. Tillack, J. D. Cressler, and J. Papapolymerou, "A D-band Micromachined End-Fire Antenna in 130-nm SiGe BiCMOS Technology", *IEEE Transactions on Antennas and Propagation*, vol. 63, no. 6, pp. 2449–2459, 2015.

[98] Y. Koga, Y. Yoshida, A. Yamashita, T. Hamaguchi, K. Nishizawa, M. Taguchi, T. Nishino, H. Miyashita, and S. Makino, "Cavity-Backed MEMS Patch Antennas on Double-Layer Silicon Wafers", in *2006 IEEE Antennas and Propagation Society International Symposium*, 2006, pp. 3935–3938.

[99] I. Papapolymerou, R. Franklin Drayton, and L. P. B. Katehi, "Micromachined Patch Antennas", *IEEE Transactions on Antennas and Propagation*, vol. 46, no. 2, pp. 275–283, 1998.

[100] V. K. Singh, "Ka-band Micromachined Microstrip Patch Antenna", *IET Microwaves, Antennas Propagation*, vol. 4, no. 3, pp. 316–323, 2010.

[101] Y. Ou and G. M. Rebeiz, "On-Chip Slot-Ring and High-Gain Horn Antennas for Millimeter-Wave Wafer-Scale Silicon Systems", *IEEE Transactions on Microwave Theory and Techniques*, vol. 59, no. 8, pp. 1963–1972, 2011.

[102] ——, "Differential Microstrip and Slot-Ring Antennas for Millimeter-Wave Silicon Systems", *IEEE Transactions on Antennas and Propagation*, vol. 60, no. 6, pp. 2611–2619, 2012.

[103] J. M. Edwards and G. M. Rebeiz, "High-Efficiency Elliptical Slot Antennas with Quartz Superstrates for Silicon RFICs", *IEEE Transactions on Antennas and Propagation*, vol. 60, no. 11, pp. 5010–5020, 2012.

[104] M. Komulainen, J. Mahonen, T. Tick, M. Berg, H. Jantunen, M. Henry, C. Free, and E. Salonen, "Embedded Air Cavity Backed Microstrip Antenna on an LTCC Substrate", *Journal of the European Ceramic Society*, vol. 27, no. 8, pp. 2881 –2885, 2007, Papers Presented at the Fourth International Conference on Microwave Materials and their Applications - MMA2006, Oulu, Finland.

[105] Y. He, Y. Chen, L. Zhang, S.-W. Wong, and Z. N. Chen, "An Overview of Terahertz Antennas", *China Communications*, vol. 17, no. 7, pp. 124–165, 2020.

[106] C. Jastrow, "300GHz Transmission System", English, *Electronics Letters*, vol. 44, 213–214(1), 3 2008.

[107] Y. Shang, H. Yu, C. Yang, Y. Liang, and W. M. Lim, "A 239281GHz Sub-THz Imager with 100MHz Resolution by CMOS Direct-Conversion Receiver with On-Chip Circular-Polarized SIW Antenna", in *Proceedings of the IEEE 2014 Custom Integrated Circuits Conference*, 2014, pp. 1–4.

[108] J. Al-Eryani, H. Knapp, J. Kammerer, K. Aufinger, H. Li, and L. Maurer, "Fully Integrated Single-Chip 305375-GHz Transceiver With On-Chip Antennas in SiGe BiCMOS", *IEEE Transactions on Terahertz Science and Technology*, vol. 8, no. 3, pp. 329–339, 2018.

[109] J. Liu, S. Chen, K. Xiao, and X. Chen, "100 GHz Silicon-based Micro-Machined Patch Antenna and Arrays", *The Journal of Engineering*, vol. 2019, no. 19, pp. 5622–5625, 2019.

[110] S. B. Yeap, Z. N. Chen, L. Rui, D. S. W. Ho, and L. T. Guan, "135-GHz Co-Planar Patch Array on BCB/Silicon with Polymer-Filled Cavity", in *2011 International Workshop on Antenna Technology (iWAT)*, 2011, pp. 344–347.

[111] T. Deckmyn, S. Agneessens, A. C. F. Reniers, A. B. Smolders, M. Cauwe, D. V. Ginste, and H. Rogier, "A Novel 60 GHz Wideband Coupled Half-Mode/Quarter-Mode Substrate Integrated Waveguide Antenna", *IEEE Transactions on Antennas and Propagation*, vol. 65, no. 12, pp. 6915–6926, 2017.

[112] "IEEE Standard for Local and Metropolitan Area Networks–Part 15.4: Low-Rate Wireless Personal Area Networks (LR-WPANs)", *IEEE Std 802.15.4-2011*, pp. 1–314, 2011.

[113] C. Liu, S. Xiao, H. Tu, and Z. Ding, "Wide-Angle Scanning Low Profile Phased Array Antenna Based on a Novel Magnetic Dipole", *IEEE Transactions on Antennas and Propagation*, vol. 65, no. 3, pp. 1151–1162, 2017.

Part I

Robust and Highly-Efficient Antenna Systems for IR-UWB Localization in Industry 4.0 Applications

2

System-Level Optimization: Modular full-wave/circuit IR-UWB co-optimization framework

Abstract

A novel, modular system-oriented full-wave/circuit Impulse Radio Ultra-Wideband (IR-UWB) co-optimization framework is presented that facilitates highly accurate and efficient system-level optimization of IR-UWB antenna systems. Based on antenna link decomposition, allowing standalone simulations of the IR-UWB antennas to calculate the antenna link transfer function, and the integration of simulation or measurements results of standalone Radio Frequency (RF) components, highly accurate results are obtained with significantly reduced computational resources. The framework focuses on the optimization of system-level metrics, the System Fidelity Factor (SFF) and the Distance Estimation Error (DEE), to facilitate the development of highly accurate IR-UWB Real-Time Locating Systems (RTLSs). To validate the framework, a dedicated time-domain measurement campaign was performed, showing a very good agreement between simulations and measurements. Finally, the framework performance is benchmarked against CST Microwave Studio, showing a reduction of simulation time by a factor 3. Furthermore, the simulations in CST Microwave Studio only provide system-level information in one orientation, whereas the presented framework fully characterizes the each orientation.

2.1 Introduction

In data driven smart factories, where the Internet-of-Things (IoT) is leveraged to facilitate the next industrial revolution (Industry 4.0), location information has become essential for workflow optimization [1], resource tracking [2], safety management [3] and autonomous robot navigation [4]. However, due to the lack of Global Positioning System (GPS) signals inside these harsh indoor factory environments, alternative indoor RTLS need to be considered to provide accurate and robust location information. Several of these RTLS have been investigated, based on infrared radiation, ultrasound, Bluetooth and WiFi [5]. However, due to the challenging propagation conditions in the smart factory, the large amount of interference sources and the massive amount of IoT devices to be serviced, the current solutions do not suffice [2]. Here, Time of Arrival (ToA) based IR-UWB RTLS have received significant attention from both the academic and industrial world. They use bursts of (sub)nanosecond pulses to transmit information and, hence, exhibit high immunity to both multipath and interference, provide high localization accuracy and longer indoor range due to the higher peak-to-average power ratio [3].

However, the ultra-wide bandwidth of such (sub)nanosecond pulses present significantly different design challenges compared to a narrowband RF-based RTLS. The Ultra-Wideband (UWB) hardware need to exhibit both excellent frequency- and time-domain performance, individually as well as on a system level [6]–[10]. Furthermore, it has been demonstrated that not only the transmit and receive chain, but also the antenna link has a significant influence on the IR-UWB RTLS performance [7], [11]–[14]. This is due to orientation-specific pulse distortion and phase-center variations, induced by non-ideal space-, frequency- and time-domain characteristics of the transmitting and receiving antenna. More specifically, a high pulse distortion introduced by the antenna link results in a high standard deviation of ranging results [15], whereas phase-center variation as a function of antenna orientation may lead to orientation-specific ranging bias [7], [16]. As a result, conventional frequency- and time-domain metrics, such as return loss, gain and group delay, do not suffice to characterize and optimize IR-UWB antennas. To accurately simulate system-level performance, a new set of metrics is required that jointly analyze the antenna behavior in the frequency, time and space domains, specifically for a certain system configuration. The amount of pulse distortion introduced by the antenna system is characterized by the SFF [6], which considers a specified input pulse traveling through the antenna link and compares it to the resulting output pulse. By calculating the SFF for different antenna orientations, the pulse distortion can be simulated for each angle of the antenna, where a high SFF (maximally 100%) signifies a low pulse distortion. The amount of ranging bias is in turn defined by the DEE, comparing the estimated ToA for different angle configurations with the ToA in boresight of the antenna. However, no commercial simulation tools currently exist to efficiently and simultaneously optimize for frequency-domain and system-level antenna metrics. This makes accurate and complete IR-UWB RTLS simulation very challenging.

In this chapter, a modular full-wave/circuit IR-UWB co-optimization framework is developed and validated to facilitate highly accurate and efficient system-level optimization of IR-UWB systems. By enabling standalone full-wave or circuit simulations of each IR-UWB component in the link and, in a next step, efficiently integrating them in the framework to characterize the complete IR-UWB system performance, a modular approach is obtained that allows for light-weight simulations with great design flexibility. Note that this also facilitates measurement results to be included in the co-optimization framework. Furthermore, the antenna link decomposition in [10] is extended to provide system-level optimization functionality, based on time-domain simulation results. As a result, IR-UWB RTLS optimization is enabled by joint frequency- and time-domain simulations, characterized by the SFF and DEE. The framework accuracy is validated by means of dedicated time-domain measurements, showing a good agreement between simulations and measurements. Additionally, its performance is benchmarked against commercial solvers, showing a significant improvement in computing time and required memory.

Dedicated simulation frameworks have been proposed in literature focusing on either the active electronics [8], [9] or the antenna link [11]–[14], but not both. In [8] and [9] a UWB simulation framework is described that models the complete IR-UWB link in Agilent Advanced Design System (ADS). However, the antenna link is modeled via generic multipath channel models and, thus, fails to incorporate the effect of orientation specific antenna effects. Although this framework provides a powerful tool for standalone hardware design, it lacks the antenna orientation dependency required for highly accurate IR-UWB RTLS simulations. In [14], the transient radiated and received pulses of UWB planar aperture antennas are modeled to predict angle-dependent pulse distortion in an antenna link. However, the used antenna parameters for simulation are hard to measure and, thus, the framework does not provide sufficient flexibility, nor does it allow to include active electronics into the simulation. Both [12] and [13] provide methods for antenna link decomposition to efficiently characterize the link transfer function. However, they do not allow the designer to incorporate circuit simulations or measurements results to enable full-wave/circuit co-optimization. Therefore, they do not accurately calculate system-level parameters. Finally, in [11], A. Sibille presents a framework for analysis of antenna effects in UWB communication. The framework provides efficient antenna link simulations in a multipath environment, by means of antenna link factorization, and analyzes the angle-dependent pulse distortion. Unfortunately, no active electronics are co-simulated and, hence, no accurate system-level characterization is possible.

The rest of this paper is organized as follows. Section 2.2 outlines the framework architecture and elaborates on the antenna link decomposition. In Section 2.3, the simulation accuracy and performance is validated and benchmarked, respectively.

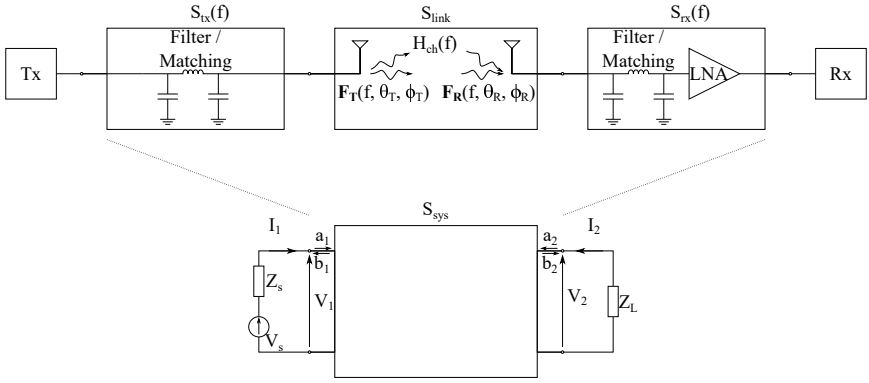

Figure 2.1: Graphical representation of the IR-UWB system and its components.

2.2 Modular IR-UWB framework

2.2.1 Framework architecture

When analyzing any IR-UWB system, three generic components can be identified: the source (or transmitter), the antenna link and the load (or receiver). The source can be further subdivided into a generator and a transmit chain, comprising a variety of microwave components such as filters and amplifiers. Similarly, the load can be subdivided into a receiver and receive chain. Finally, the antenna link can be implemented by any pair of transmit and receive antennas, each in different orientations, and a deterministic communication channel, which may be a free-space link or a multpath channel. As such, a modular approach is required to facilitate efficient and agile IR-UWB system-level simulations. To characterize the performance of an IR-UWB system, given a certain predefined reference pulse, a thorough frequency- and time-domain analysis of the complete IR-UWB link is required. By calculating the pulse received at the receiver and comparing it with the reference pulse, a wide variety of system-level metrics can be extracted, such as the SFF and the DEE. To this end, a modular IR-UWB full-wave/circuit co-optimization framework is proposed, as depicted in Fig. 2.1, where the complete IR-UWB link is characterized by cascading the transmit chain, the antenna link and the receive chain. Each component is considered linear and is characterized by its S-parameters S_i, calculated by either a circuit or full-wave solver, or a combination of both. The S-parameters of the complete IR-UWB system are then calculated by cascading the subsequent S-parameters of the transmit chain S_{tx}, the antenna link S_{link} and the receive chain S_{rx}. It is, however, noteworthy to mention that performing a full-wave simulation of the antenna link for each relevant antenna orientation quickly becomes computationally intensive and doesn't scale well for large inter-antenna distances.

To calculate the resulting output pulse, the IR-UWB system S-parameters need to

be transformed into the system transfer function, defined as $H_{sys}(f) = \frac{V_2}{V_1}$. The equivalent ABCD-parameters allow to directly extract this relationship, as seen in definition (2.1)

$$\begin{bmatrix} V_1 \\ I_1 \end{bmatrix} = \begin{bmatrix} A & B \\ C & D \end{bmatrix} \begin{bmatrix} V_2 \\ -I_2 \end{bmatrix} \tag{2.1}$$

with

$$\begin{cases} A = \frac{(1+S_{11})(1-S_{22})+S_{12}S_{21}}{2S_{21}} \\ B = Z_0 \frac{(1+S_{11})(1+S_{22})-S_{12}S_{21}}{2S_{21}} \\ C = \frac{1}{Z_0} \frac{(1-S_{11})(1-S_{22})-S_{12}S_{21}}{2S_{21}} \\ D = \frac{(1-S_{11})(1+S_{22})+S_{12}S_{21}}{2S_{21}} \end{cases} \tag{2.2}$$

and Z_0 the reference impedance of the S-parameters. The system transfer function is then calculated as

$$H_{sys}(f) = \frac{Z_L}{AZ_L + B + CZ_sZ_L + DZ_s}, \tag{2.3}$$

with Z_s and Z_L the source and load impedance, respectively. Next, to calculate the output pulse, the system impulse response $h_{sys}(t)$ is computed by performing an inverse Fourier transformation. The output pulse $x(t)$ is then calculated as

$$x(t) = s(t) * h_{sys}(t) \tag{2.4}$$

with $s(t)$ the input pulse and $*$ the convolution operator. Once the output pulse is calculated, any system-level characteristic can be determined by comparing it to the input pulse. The SFF and DEE are of particular interest in the context of IR-UWB indoor localization systems, as they characterize the localization system accuracy and robustness. The SFF is defined as

$$\mathrm{SFF}(\theta, \phi) = \max_t \left| \frac{\int_{t_0}^{t_n} s(\tau) x(\tau + t, \theta, \phi) d\tau}{\sqrt{\int_{t_0}^{t_n} s^2(\tau) d\tau \int_{t_0}^{t_n} x^2(\tau, \theta, \phi) d\tau}} \right|, \tag{2.5}$$

with θ and ϕ the azimuth and polar angle in a spherical coordinate system, respectively, and $s(t)$ and $x(t)$ the input and output pulse, respectively. The DEE is defined by

$$d_{est,e}(\theta, \phi) = (t_{max}(\theta, \phi) - t_{max}(0,0))\, c, \tag{2.6}$$

with c the speed of light and $t_{max}(\theta, \phi)$ and $t_{max}(0,0)$ the time at which the SFF becomes maximum for (θ, ϕ) and broadside, respectively.

Finally, the discretization of continuous time-domain signals and frequency-domain parameters during simulations impacts not only the computational workload, but the system-level parameter accuracy as well. Therefore, it is important to consider its impact on the SFF and the DEE. First, the relation between the time- and frequency-domain properties is defined by

$$\begin{cases} \delta f = \frac{1}{t_{max}} \\ \delta t = \frac{1}{f_s}, \end{cases} \tag{2.7}$$

with δt and t_{max} the time step and the maximum observation time, respectively, and δf and f_s the frequency step and sampling frequency, respectively. When looking at (2.5) and (2.6), it can be seen that the accuracy depends on the time-domain resolution. On the one hand, a suitable δt should be selected to minimize loss of pulse information and maximize SFF and DEE accuracy. In the context of IR-UWB localization, sub-nanosecond pulses are used and, as such, a guideline is to select $\delta t < 10$ ps [17], corresponding to a sampling frequency above 100 GHz. On the other hand, the maximum observation time t_{max} is determined by the maximum path length traveled by the signal from the input to the output of the IR-UWB system. To prevent time-domain aliasing, t_{max} is constrained by

$$t_{max} \geq t_{p,max} + \sum_{i=0}^{n} \frac{r_i}{v_i}, \tag{2.8}$$

with $t_{p,max}$ the input pulse duration and r_i and v_i the maximal path length and wave speed in component i, respectively. Similarly, the frequency step δf is constrained by $\delta f \leq t_{max}^{-1}$. Note that cascading the different components in the time or frequency domain requires an identical δf or δt, respectively.

Although the modular framework enables accurate time-domain simulations for a fixed antenna link, it quickly becomes computationally intensive once the system-level performance needs to be assessed for different antenna orientations. Furthermore, because the antenna link is considered as a monolithic component, it significantly degrades the framework modularity. It prevents replacing one of the antennas in the link without having to re-simulate the link for each relevant orientation configuration. These issues are mitigated by decomposing the antenna link based on the radiation patterns and impedance of the standalone antennas, as discussed below.

2.2.2 Antenna link decomposition

As mentioned before, full-wave simulation of an antenna link for different antenna orientations and separations quickly becomes computationally intensive and, therefore, the antenna link should be decomposed to enable link simulations based on the individual radiation patterns of the standalone antennas. To this end, a circuit equivalent model is derived for the antenna link without additional peripheral circuitry, as proposed in [10]. As in Fig. 2.2, the transmit antenna is modeled by its internal radiation impedance Z_T, whereas the receive antenna is modeled by its internal radiation impedance Z_R which is excited in a free-space environment without multipath by an incident electromagnetic plane wave, represented by the voltage source

$$V_o = \frac{-2jc}{Z_c f} \left(\mathbf{F}_R(-\mathbf{u_0}) \circ \mathbf{E}^{inc} \right), \tag{2.9}$$

with Z_c the free-space wave impedance, $\mathbf{F}_R(-\mathbf{u_0})$ the radiation vector of the receive antenna in direction $\mathbf{u_0}$ and $\mathbf{E}^{inc}$ the electric field of a plane wave impinging from

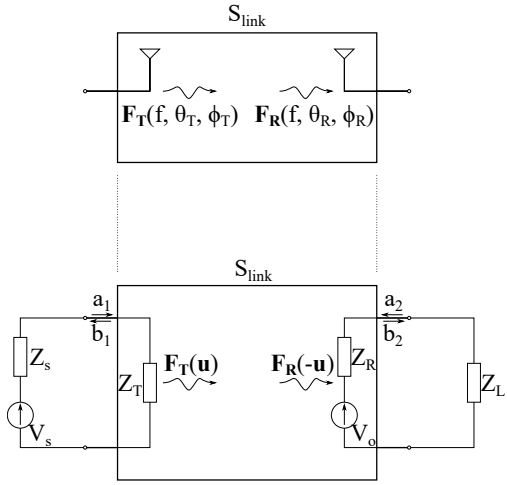

Figure 2.2: Equivalent circuit of the link between the transmit antenna (left) and the receive antenna (right).

that direction. The transmit antenna is excited by a voltage source V_s with source impedance Z_s. The receive antenna is loaded by an impedance of Z_L.

The transmission of the antenna link $S_{link,21}$ at frequency f is calculated as

$$S_{link,21} = \left(\frac{|\mathbf{F_R}(-\mathbf{u_0})|}{Z_L + Z_R}\right)\left(\frac{-2j\lambda}{Z_c} Z_L \frac{\mathbf{F_R}(-\mathbf{u_0}) \circ \mathbf{F_T}(\mathbf{u_0})}{|\mathbf{F_R}(-\mathbf{u_0})||\mathbf{F_T}(\mathbf{u_0})|} \frac{e^{-jkr}}{r}\right)\left(\frac{|\mathbf{F_T}(\mathbf{u_0})|}{Z_T + Z_S}\right), \quad (2.10)$$

with $\lambda = c/f$ the free-space wavelength, k the wave number and r the distance between the two antennas [10]. Furthermore, $\mathbf{F}(\mathbf{u_0})$ is the current normalized radiation pattern for the direction defined by $\mathbf{u_0}$. This radiation pattern can be expressed in terms of its orthogonal θ and ϕ components as

$$\begin{cases} \mathbf{F}(\mathbf{u_0}) = F_\theta(\mathbf{u_0})\hat{\theta} + F_\phi(\mathbf{u_0})\hat{\phi} \\ \mathbf{F}(-\mathbf{u_0}) = F_\theta(\mathbf{u_0})\hat{\theta} - F_\phi(\mathbf{u_0})\hat{\phi}. \end{cases} \quad (2.11)$$

The resulting dot product of both vectors is defined by

$$\mathbf{F_R}(-\mathbf{u_0}) \circ \mathbf{F_T}(\mathbf{u_0}) = F_{R,\theta}(\theta,\phi)F_{T,\theta}(\theta,\phi) - F_{R,\phi}(\theta,\phi)F_{T,\phi}(\theta,\phi). \quad (2.12)$$

As the antenna link is reciprocal, the full two-port S-parameters $\mathbf{S_{link}}$ are then constructed as

$$\mathbf{S_{link}} = \begin{bmatrix} S_{11,T} & S_{link,21} \\ S_{link,21} & S_{11,R} \end{bmatrix}, \quad (2.13)$$

with $S_{11,T}$ and $S_{11,R}$ the reflection coefficient of the transmit and receive antenna, respectively.

From (2.13), any combination of antennas can be simulated in a link at any target frequency f, regardless of the orientation or the distance between them, as long as the normalized radiation pattern $\mathbf{F}(\mathbf{u_0})$ is calculated for the standalone antenna elements for the targeted frequency of operation. In order to extend this functionality to time-domain simulations, first the frequency-domain axis should be defined based on the considerations of (2.7). Next, the link S-parameters S_{link} should be calculated for each frequency bin in the frequency-domain axis. Finally, the S-parameters of all components in the IR-UWB system are cascaded, as shown in Fig. 2.1, to calculate S_{sys}. After conversion to ABCD-parameters, the system transfer function H_{sys} is calculated by (2.3).

2.3 Validation: An example IR-UWB link

To validate the theory postulated in the previous section, the proposed modular IR-UWB framework is applied to simulate the following IR-UWB link: The IR-UWB link is composed of a transmit antenna, described in Chapter 3, and a receive antenna, described in Chapter 4, spaced 1.0 m apart in free space (corresponding to a delay of 3.3 ns). A modulated root-raised-cosine pulse is transmitted, characterized by

$$s(t) = \cos(2\pi f_0 t)\frac{2}{\pi\sqrt{T_p}}\frac{\cos(1.5\pi t/T_p) + \frac{\sin(0.5\pi t/T_p)}{2t/T_p}}{1-(2t/T_p)^2}, \tag{2.14}$$

with $f_0 = 4.25$ GHz the pulse carrier frequency and $T_p = 0.92$ ns the pulse width, resulting in a pulse bandwidth of 1.5 GHz and thereby covering channels 1, 2 and 3 of the IEEE 802.15.4z standard. The input pulse duration $T_{p,max}$ is 15 ns and, as such, the total required simulation time ($t_{max} \geq 15$ ns$+3.3$ ns$= 18.3$ ns) is chosen to be 20 ns. To measure the proposed IR-UWB system, a dedicated time-domain measurement setup, described in more detail in Chapter 4, is utilized inside an anechoic chamber, composed of an M8196A Arbitrary Waveform Generator (AWG) (with a sampling rate of 92 GSa/s) to generate the input pulse and a DSAX96204Q Real-Time Oscilloscope (RTO) (sampling at 160 GSa/s) to measure the received pulses. The resulting time- and frequency-domain axis properties are given by

$$\begin{cases} f_s = 160 \text{ GHz} \\ t_{max} = 20 \text{ ns} \\ \delta f = \frac{1}{t_{max}} = \frac{1}{20 \text{ ns}} = 50 \text{ MHz} \\ \delta t = \frac{1}{f_s} = \frac{1}{160 \text{ GHz}} = 6.25 \text{ ps}. \end{cases} \tag{2.15}$$

However, to prevent exuberant simulation times because of the large frequency simulation range ($[0-160]$ GHz), a final optimization step is required. When analyzing the measured input pulse spectrum, depicted in Fig 2.3, it is apparent that only a limited part of the spectrum contains relevant information on the pulse. In order to determine the exact frequency range that contains the pulse information,

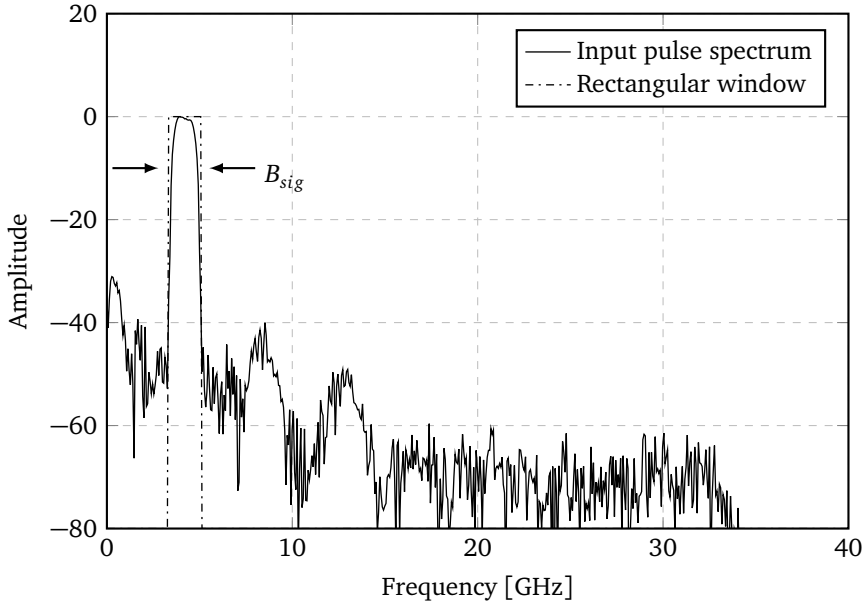

Figure 2.3: Normalized input pulse spectrum and superimposed rectangular window.

a rectangular window is superimposed on the input pulse spectrum. The resulting windowed spectrum $S_{win}(f)$, depicted in Fig. 2.3, is defined by

$$S_{win}(f, B_{sig}) = \text{rect}\left(\frac{f - f_0}{B_{sig}}\right) S(f), \tag{2.16}$$

with $S(f) = \text{FFT}(s(t))$ the spectrum of the input pulse, B_{sig} the significant bandwidth of the input pulse and

$$\text{rect}\left(\frac{f - f_0}{B_{sig}}\right) = \begin{cases} 0, \text{ if } |f - f_0| > B_{sig}/2 \\ 0.5, \text{ if } |f - f_0| = B_{sig}/2 \\ 1, \text{ if } |f - f_0| < B_{sig}/2. \end{cases} \tag{2.17}$$

The inverse Fourier transform of the windowed spectrum S_{win} is calculated by the convolution

$$s_{win}(t) = 2\pi B_{sig} e^{j2\pi f_0 B_{sig} t} \text{sinc}\left(2\pi B_{sig} t\right) * s(t). \tag{2.18}$$

As seen in (2.18), the windowing effect appears as a sinc pulse with a pulse width defined by B_{sig}. To minimize this windowing effect, B_{sig} is optimized by iteratively increasing B_{sig} until

$$\max_t \left| \frac{\int_{t_0}^{t_n} s(\tau) s_{win}(\tau + t) d\tau}{\sqrt{\int_{t_0}^{t_n} s^2(\tau) d\tau \int_{t_0}^{t_n} s_{win}^2(\tau) d\tau}} \right| > 0.9995. \tag{2.19}$$

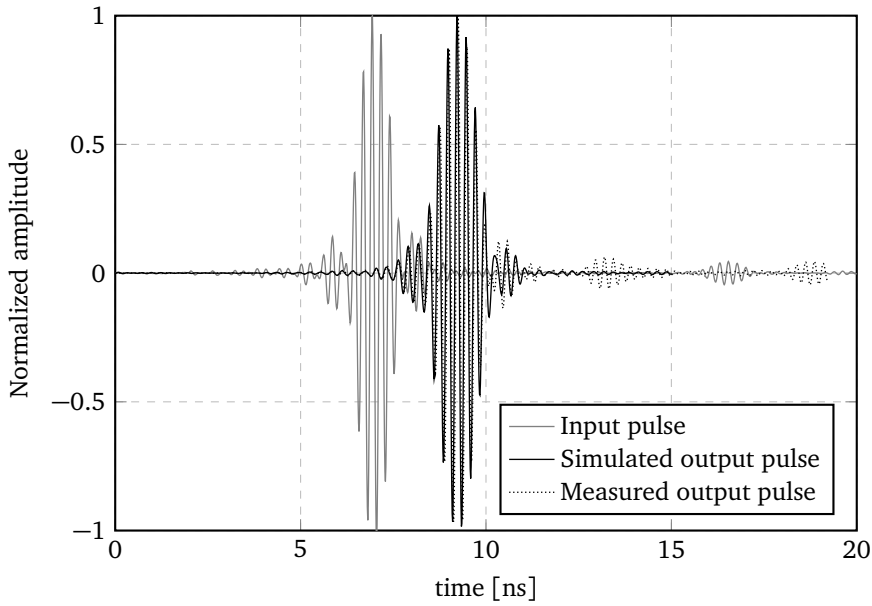

Figure 2.4: Normalized amplitude of the simulated and measured output pulse, compared to the input pulse.

Table 2.1: Summary of time-domain results and computational requirements.

	SFF [%]	**Sim. time [s]**	**Req. memory [MB]**
Measured	96.2		
Simulated (full-wave)	97.3	1869	2250
Simulated (framework)	96.9	598	2486

In the current example, with the input pulse defined by (2.14), the optimal window is found to be $B_{sig} = 1.7$ GHz with a pulse carrier frequency $f_0 = 4.25$ GHz.

The normalized input pulse is depicted together with the normalized simulated (with the proposed IR-UWB framework) and measured output pulse in Fig. 2.4. A good agreement can be observed between the simulated and measured output pulse. Small multipath components can be identified in the measured output pulse, due to imperfect shielding of measurement equipment in the anechoic chamber.

The agreement between simulated and measured pulse is more clearly visible in Fig. 2.5, where the normalized baseband representations of the input and output pulses are depicted.

A summary of the results is provided in Table 2.1, depicting the predicted SFF and benchmarking the proposed framework performance against two-port full-wave simulations in CST Microwave Solver. A good agreement between simulated and

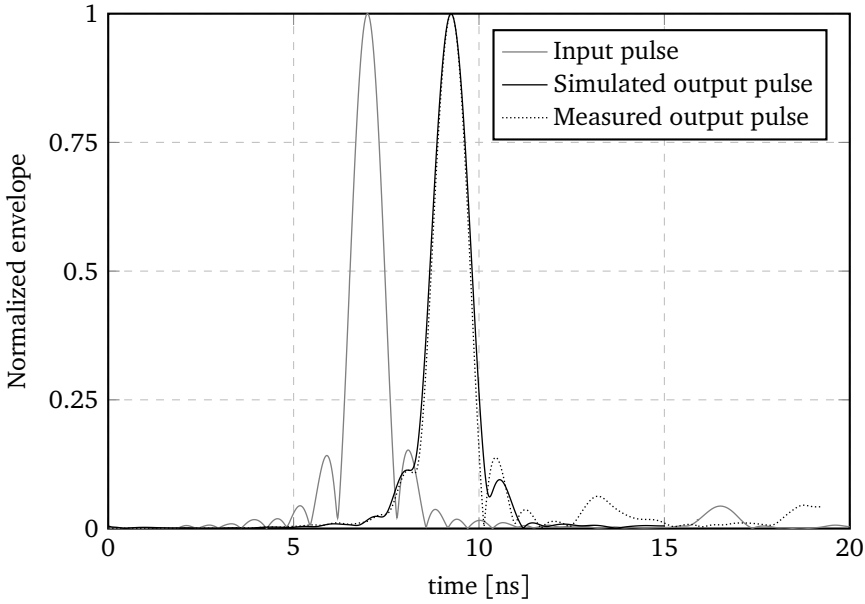

Figure 2.5: Normalized envelope of the simulated and measured baseband waveforms, compared to the input baseband waveform.

measured SFF can be seen. Furthermore, the full-wave solver only computes one antenna orientation at a specified distance per simulation and, as such, does not scale well when additional orientations or distances need to be simulated. The proposed modular IR-UWB framework computes the required system-level parameters for all requested orientations and distances in one simulation. In addition, the simulation time is not affected by the number of orientations or distance between the antennas and, as such, provides the required flexibility and performance for the optimization of IR-UWB systems.

2.4 Conclusion

A novel, modular system-oriented full-wave/circuit IR-UWB co-optimization framework is presented to efficiently develop highly accurate and efficient system-level IR-UWB antenna systems for highly accurate RTLSs. Special care is devoted to integrate standalone simulation results into a system-level simulation, thereby facilitating light-weight simulations with great design flexibility. To obtain high accuracy with significantly reduced computational resources, the antenna link is partitioned, enabling the combination of standalone full-wave antenna simulations with different wireless channel models to construct the two-port antenna link. The complete IR-UWB is jointly characterized in the frequency, time and space domains, allowing

the assessment and optimization of the system-level performance in terms of the SFF and the DEE. The proposed framework is validated by means of a series of dedicated time-domain measurements, transmitting and measuring IR-UWB pulses in an anechoic chamber by using a AWG and RTO, respectively. A good agreement between simulations and measurements is observed. Finally, the framework performance is benchmarked against commercial solvers, showing a reduction in the orders of magnitude of the required computing time and memory.

References

[1] B. J. Silva and G. P. Hancke, "Practical Challenges of IR-UWB based Ranging in Harsh Industrial Environments", in *2015 IEEE 13th International Conference on Industrial Informatics (INDIN)*, 2015, pp. 618–623.

[2] A. Racz-Szabo, T. Ruppert, L. Bantay, A. Locklin, L. Jakab, and J. Abonyi, "Real-Time Locating System in Production Management", *Sensors*, vol. 20, no. 23, 2020.

[3] S. Jiang, M. J. Skibniewski, Y. Yuan, C. Sun, and Y. Lu, "Ultra-Wide Band Applications in Industry: A Critical Review", *Journal of Civil Engineering and Management*, vol. 17, no. 3, pp. 437–444, 2011.

[4] A. D. Preter, G. Goysens, J. Anthonis, J. Swevers, and G. Pipeleers, "Range Bias Modeling and Autocalibration of an UWB Positioning System", in *2019 International Conference on Indoor Positioning and Indoor Navigation (IPIN)*, 2019, pp. 1–8.

[5] A. Syberfeldt, M. Ayani, M. Holm, L. Wang, and R. Lindgren-Brewster, "Localizing Operators in the Smart Factory: A Review of Existing Techniques and Systems", in *2016 International Symposium on Flexible Automation (ISFA)*, 2016, pp. 179–185.

[6] G. Quintero, J. Zurcher, and A. K. Skrivervik, "System Fidelity Factor: A New Method for Comparing UWB Antennas", *IEEE Transactions on Antennas and Propagation*, vol. 59, no. 7, pp. 2502–2512, 2011.

[7] M. R. Mahfouz, C. Zhang, B. C. Merkl, M. J. Kuhn, and A. E. Fathy, "Investigation of High-Accuracy Indoor 3-D Positioning Using UWB Technology", *IEEE Transactions on Microwave Theory and Techniques*, vol. 56, no. 6, pp. 1316–1330, 2008.

[8] M. J. Kuhn, C. Zhang, S. Lin, M. R. Mahfouz, and A. E. Fathy, "A System Level Design Approach to UWB Localization", in *2009 IEEE MTT-S International Microwave Symposium Digest*, 2009, pp. 1409–1412.

[9] M. J. Kuhn, M. R. Mahfouz, C. Zhang, B. C. Merkl, and A. E. Fathy, "A System-Level Simulation Framework for UWB Localization", *IEEE Transactions on Microwave Theory and Techniques*, vol. 58, no. 12, pp. 3527–3537, 2010.

[10] T. Cuyckens and H. Rogier, "Framework for the Simulation of Wireless Power Transmission over Ultra Wide Band Links in Multipath Propagation Environments in the Vicinity of the Human Body", *International Journal of Numerical Modelling: Electronic Networks, Devices and Fields*, vol. 29, no. 3, pp. 364–379, 2016.

[11] A. Sibille, “A Framework for Analysis of Antenna Effects in UWB Communications”, in *2005 IEEE 61st Vehicular Technology Conference*, vol. 1, 2005, 48–52 Vol. 1.

[12] A. O. Boryssenko and D. H. Schaubert, “Antenna Link Transfer Function Factorization Applied to Optimized Channel Design”, *IEEE Transactions on Antennas and Propagation*, vol. 54, no. 10, pp. 2878–2889, 2006.

[13] X. Qing, Z. N. Chen, and M. Y. W. Chia, “Characterization of Ultrawideband Antennas using Transfer Functions”, *Radio Science*, vol. 41, no. 01, pp. 1–10, 2006.

[14] A. E. Tan, M. Y. Chia, K. K. Chan, and K. Rambabu, “Modeling the Transient Radiated and Received Pulses of Ultra-Wideband Antennas”, *IEEE Transactions on Antennas and Propagation*, vol. 61, no. 1, pp. 338–345, 2013.

[15] H. Vanhuysse, Q. Van den Brande, M. Ridolfi, J. Rossey, B. Van Herbruggen, E. De Poorter, and S. Lemey, “Analysis of Range and Accuracy of an UWB Indoor Localization System”, M.S. thesis, Ghent University, Jul. 2019.

[16] Q. Van den Brande, S. Lemey, and H. Rogier, “Planar Sectoral Antenna for IR-UWB Localization With Minimal Range Estimation Biasing”, *IEEE Antennas and Wireless Propagation Letters*, vol. 20, no. 2, pp. 135–139, 2021.

[17] I. Recommendation, “Measurement Techniques of Ultra-Wideband Transmissions”, 2006.

3

System Fidelity Factor: Highly-Efficient IR-UWB Cavity-Backed Slot Antenna in Stacked AFSIW Technology

Abstract

An Impulse Radio Ultra-Wideband (IR-UWB) cavity-backed slot antenna covering the [5.9803; 6.9989] GHz frequency band of the IEEE 802.15.4a-2011 standard is designed and implemented in Air-Filled Substrate-Integrated-Waveguide (AFSIW) technology for localization applications with an accuracy of at least 3 cm. By relying on both frequency- and time-domain optimization, the antenna achieves excellent IR-UWB characteristics. In free-space conditions, an impedance bandwidth of 1.92 GHz (or 29.4 %), a total efficiency higher than 89 %, a front-to-back-ratio of at least 12.1 dB and a gain higher than 6.3 dBi are measured in the frequency domain. Furthermore, a system fidelity factor larger than 98 % and a relative group delay smaller than 100 ps are measured in the time domain within the Half-Power Beamwidth (HPBW) of the antenna. As a result, the measured time-of-arrival of a transmitted Gaussian pulse, for different angles of arrival, exhibits variations smaller than 100 ps, corresponding to a maximum distance estimation error of 3 cm. Additionally, the antenna is validated in a real-life worst-case deployment scenario, showing that its characteristics remain stable in a large variety of deployment scenarios. Finally, the difference in frequency-domain and time-domain performance is studied between the antenna implemented in AFSIW and in Dielectric-Filled Substrate-Integrated-Waveguide (DFSIW) technology. We conclude that DFSIW technology is less suitable for the envisaged precision IR-UWB localization application.

3.1 Introduction

The IR-UWB technology is one of the most promising solutions for accurate localization in indoor and in obstructed or difficult outdoor environments. Exploiting (sub)nanosecond duration pulses yields supreme position accuracy and ensures excellent resilience against narrowband interference and multipath effects [1], [2]. The latter adverse propagation characteristics are typically encountered in dense and heterogeneous Internet-of-Things (IoT) environments, in applications such as indoor localization [3], healthcare [4]–[8] and low-power Ultra-Wideband (UWB) communication [9], [10].

However, the ultra-wide bandwidth of such a short pulse implies different radiowave propagation characteristics as compared to narrowband systems. Therefore, substantially different antenna topologies are required [11], exhibiting both excellent frequency- and time-domain characteristics. Moreover, UWB antenna design for practical systems should focus on guaranteeing the desired performance in the envisaged deployment scenarios, rather than being optimized in a stand-alone free-space set-up [12], [13]. On the one hand, a plethora of IR-UWB antennas are found in current literature [11], [14], [15]. These antennas exhibit suitable form factors [16] and excellent ultra-wideband characteristics. However, all these antennas were validated in stand-alone free-space conditions. They are easily detuned by objects in their direct proximity. On the other hand, [12] and [17] have proposed innovative UWB textile cavity-backed slot antennas in DFSIW technology that guarantee highly-efficient and robust performance in the frequency domain, even in the challenging IoT environment. As such, the cavity-backed slot antenna topology implemented in a dielectric substrate forms a suitable foundation to achieve the desired performance characteristics. However, the latter designs were not optimized nor validated for IR-UWB applications. Hence, to guarantee precise and robust ranging, the proposed antenna should be optimized and validated for system-oriented time-domain metrics, to account for the effect of the antenna design on the global UWB channel.

In this article, a highly-efficient IR-UWB coupled half-mode cavity-backed slot antenna in a stacked AFSIW technology is reported. In order to obtain the required antenna characteristics, the antenna, based on a cavity-backed slot antenna topology, is implemented using the coupled half-mode technique [18]. Furthermore, to achieve the high performance demands, as required for the precision IR-UWB localization, the antenna is realized in AFSIW technology. Through optimization in both the frequency and the time domain, the proposed antenna exhibits outstanding IR-UWB characteristics in its HPBW, such as a very high system fidelity factor and a minimal relative group delay. As a result, pulse distortion is minimized and time-of-arrival variations comply with the requirements for precision IR-UWB localization. For validation purposes, the antenna is also measured in a realistic hostile environment to guarantee robust ranging performance. Furthermore, the proposed antenna is suitable for mass production industrial applications owing to its low-cost fabrication process and its topology, which allows for seamless inte-

gration with the active IR-UWB electronics.

Due to the low fabrication cost and high efficiency, AFSIW technology has become a novel up-and-coming trend in microwave and millimeter wave applications [19]–[29]. Various AFSIW designs and fabrication methodologies have been proposed in literature. [19]–[23] have proposed numerous AFSIW filters, phase shifters and transitions implemented in multilayer Printed Circuit Board (PCB) technology. Soldering paste is applied between the different milled and copper plated layers to preclude radiation leakage. Another fabrication technology is applied in [24], where an AFSIW slotted G-band horn antenna is micromachined. In [25], a 15 GHz highly-efficient AFSIW H-plane horn antenna is reported, constructed by stacking several layers of copper plated FR4 substrates. A -10 dB impedance bandwidth of 250 MHz is achieved, with a total efficiency of 89.1 % at 15 GHz. In [26], a 11.75 GHz AFSIW resonant slot array is described. This design is fabricated by milling the contours of the waveguide in the dielectric substrate, after which traditional additive processes are used to metallize the milled recess. A -15 dB impedance bandwidth of 100 MHz is obtained. Finally, two AFSIW UWB antennas are reported in [27], [28]. In [27], a highly-efficient 30.5 GHz UWB AFSIW slot array antenna is described, achieving a -10 dB impedance bandwidth of 2.64 GHz. In [28] a highly-efficient *Ka*-band UWB AFSIW antipodal linearly tapered slot antenna is reported, achieving a -10 dB impedance bandwidth of 14 GHz. Although both studies compare the performance of the AFSIW design to its DFSIW counterpart in the frequency domain, they are not optimized nor validated for time-domain characteristics. Hence, their use in precision IR-UWB localization applications is not recommended without further analysis.

The remainder of this paper is organized as follows. Section 3.2 outlines the antenna design process, describing the antenna specifications, the antenna topology and its operation principle, elaborating on the implementation technology and specifying the final antenna dimensions. In Section 3.3, the AFSIW technology is compared to its DFSIW counterpart by means of simulations. The comparison is based on the antenna form factor, bandwidth performance and radiation efficiency. Finally, the simulation and measurement results for the proposed antenna are reported in Section 3.4. Both frequency-domain and time-domain results are discussed.

3.2 Coupled Half-Mode AFSIW Cavity-Backed Slot IR-UWB Antenna

3.2.1 Antenna design specifications

The proposed IR-UWB antenna is designed in compliance with the IEEE 802.15.4a-2011 standard [30]. In this work, the design is optimized for operation in the [5.9803; 6.9989] GHz frequency band, covering channels 5 and 7 of the IEEE 802.15.4a-2011 standard. A magnitude of the reflection coefficient with respect

to 50Ω, $|S_{11}(f)|$, below -10 dB and a total antenna efficiency of more than 85 % is imposed in the entire specified frequency band.

When considering UWB antennas, time-domain effects cannot be neglected [31]. A plethora of time-domain parameters has been proposed in literature [11], but, in particular the magnitude of the relative group delay and the system fidelity factor are of importance for IR-UWB localization. The magnitude of the relative group delay [32] is considered over the frequency range of interest and is defined by

$$\left|\tau_{g,r}\right| = \left| \frac{d\phi(\omega)}{d\omega} - \frac{1}{\omega_n - \omega_0} \int_{\phi_0}^{\phi_n} d\phi \right|, \tag{3.1}$$

with ω and ϕ the angular frequency and phase, respectively. The system fidelity factor [33] is defined by

$$SFF = \max_t \left| \frac{\int_{t_0}^{t_n} s(\tau)x(\tau + t)d\tau}{\sqrt{\int_{t_0}^{t_n} s^2(\tau)d\tau \int_{t_0}^{t_n} x^2(\tau)d\tau}} \right|, \tag{3.2}$$

with $s(t)$ and $x(t)$ the input and output pulse, respectively. Furthermore, considering the envisaged application of sub-3cm accurate IR-UWB localization, the accuracy of the estimated distance is chosen as an additional system-oriented figure-of-merit. In order to minimize ranging errors to a maximum of 3 cm, the magnitude of the relative group delay $|\tau_{g,r}(f, \theta, \phi)|$ must be smaller than 100 ps and the System Fidelity Factor (SFF) should be higher than 98 % for all orientations within the HPBW of the antenna [34].

Finally, antenna design for IR-UWB localization applications imposes certain requirements to guarantee robust performance and high efficiency in realistic deployment scenarios. To minimize platform and proximity effects in actual operating conditions, high shielding of the fields in undesired directions is imposed. Therefore, the radiation pattern should be tailored to the envisaged application. Furthermore, for seamless and inconspicuous integration of the IR-UWB antenna, a compact low-profile antenna design is necessary whilst maintaining a high efficiency.

3.2.2 Antenna topology

In order to satisfy the design specifications, we rely on a cavity-backed slot antenna topology [35], as illustrated in Fig. 3.1, for our novel IR-UWB antenna design. It consists of a hollow metallic cavity, through which electromagnetic waves only radiate via a slot in the top metal plane. The solid metal walls confine the electromagnetic fields to the air cavity and ensure that electromagnetic radiation only originates from the slot. Thereby, the antenna mainly radiates in the hemisphere along the positive z-axis. Undesired (backside) radiation is minimized, yielding a very high Front-to-Back Ratio (FTBR). Moreover, the topology is well-known for

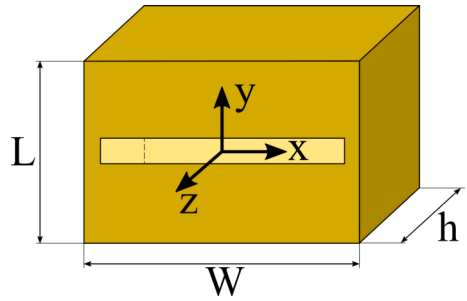

Figure 3.1: Example of a conventional cavity-backed slot antenna topology.

its very high radiation efficiency [36]. Hence, such topologies demonstrate great potential, as they provide stable characteristics when installed in or onto different everyday objects and when exploited as an integration platform for additional electronic hardware [37]. Despite these excellent features, conventional cavity-backed slot antennas mainly exhibit narrowband behavior, due to excitation of only one resonant cavity mode [38]. To enhance the bandwidth performance of the antenna, we leverage a coupled half-mode AFSIW cavity-backed slot antenna topology.

3.2.3 Operation principle

An ultra-wide -10-dB impedance bandwidth is obtained by judiciously combining two half-mode cavity-backed slot antennas, resonating at distinct frequencies, into one single-footprint antenna topology. The three-step design procedure is shown in Fig. 3.2. Two rectangular resonating cavities, operating at their fundamental TE_{110}-mode, form the starting point of the design process. Cavity A resonates at frequency f_{res1}, while cavity B resonates at frequency f_{res2}. Because of the symmetric field distribution of the TE_{110}-mode inside these rectangular cavities, their horizontal geometric symmetry plane (Fig. 3.2(a)) behaves as a virtual magnetic wall. Hence, in a first step, their size can be reduced by a factor two by cutting away the lower half of the cavity along this symmetry plane, without significant loss in antenna performance [39], [40]. A small ground plane extension is kept to direct radiation towards the positive z-direction. Now, both half-mode cavities radiate via leakage through the open side walls, which yields efficient antenna operation. These cavities are then brought together into one antenna topology (Fig. 3.2(b)), in such a way that the virtual magnetic walls of both half-mode cavities face each other, with a spacing D_{AB} between them. By removing the dielectric substrate inside the antenna, the resulting antenna forms a coupled half-mode AFSIW cavity-backed slot antenna (Fig. 3.2(c)).

To minimize backside radiation, as potentially generated by slots that are part of a grounded coplanar waveguide (GCPW) feed or aperture coupled feed [41], the half-mode cavity B is excited by means of a coaxial probe feed. Via the open side

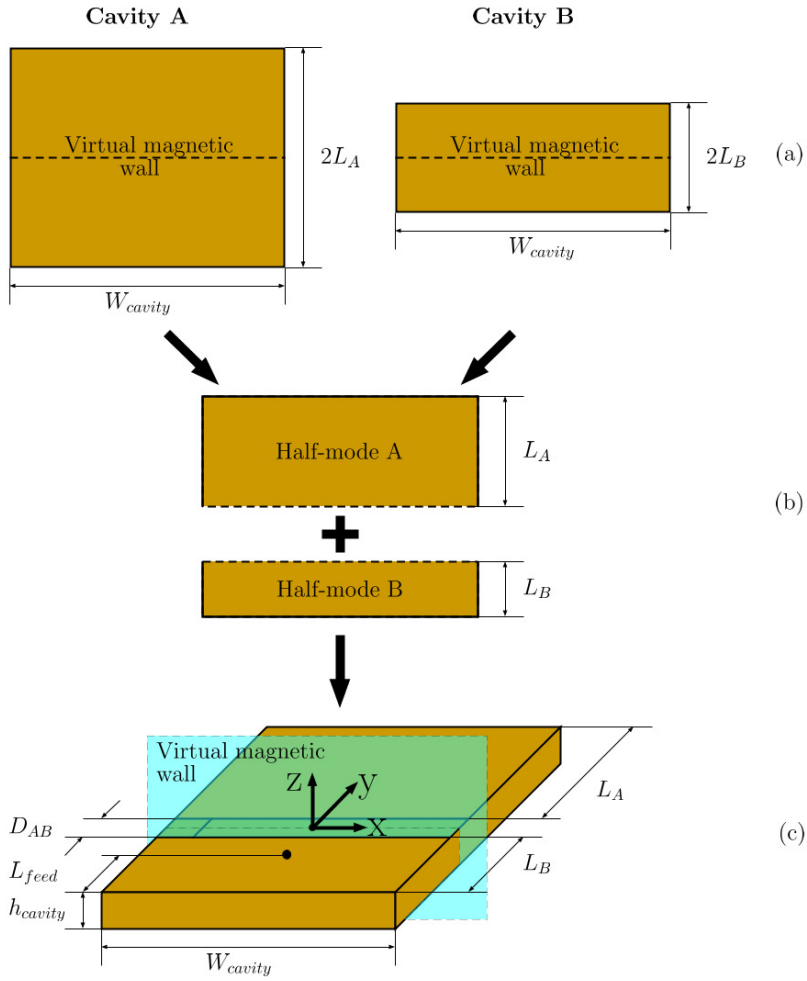

Figure 3.2: Design evolution of coupled half-mode cavity-backed slot antenna.

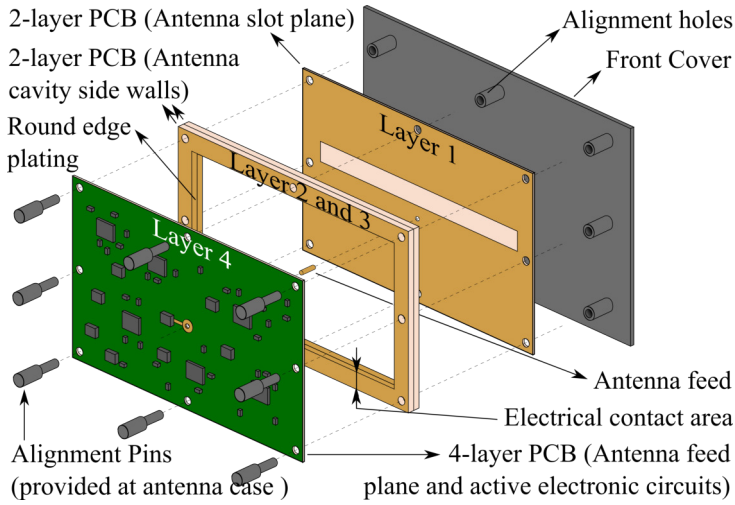

Figure 3.3: Implementation of the cavity-backed slot antenna in standard PCB technology, with integrated IR-UWB circuitry. The copper plated surfaces of the antenna are indicated in dark yellow.

walls, the fields in half-mode cavity B couple into half-mode cavity A. The coupling between both half-mode cavities, controlled by the spacing D_{AB} (Fig. 3.2(c)) between them, introduces mode splitting [42]. As a result, the resonance frequencies of the TE_{110}-mode in the half-mode cavities shift from f_{res1} and f_{res2} to f'_{res1} and f'_{res2}, respectively. Thus, by carefully selecting D_{AB} and both resonance frequencies f_{res1} and f_{res2}, the impedance bandwidth is considerably enlarged by overlapping the -10-dB impedance bandwidth of both half-mode cavity resonances at f'_{res1} and f'_{res2}.

3.2.4 Fabrication technology

In this work, the coupled half-mode AFSIW cavity-backed slot antenna is realized using standard PCB manufacturing techniques in low-cost PCB substrates, as depicted in Fig. 3.3. The side walls of the air-filled cavity are created by milling a rectangular hole in a standard FR4 substrate [43], after which the milled sides are metalized using rounded edge plating. By relying on multiple similar FR4 substrates and/or by applying different thicknesses for each separate 2-layer PCB, a wide variety of cavity thicknesses can be obtained. Next, the feed and slot plane of the AFSIW cavity-backed slot antenna are implemented on two distinct standard PCB substrates. The antenna slot plane is implemented on a standard two-layer high-frequency laminate, such as Rogers RO4350b [44], while the antenna feed plane can be shared with the PCB on which the antenna circuitry is implemented. The latter minimizes the length of the Radio Frequency (RF) connection between UWB transceiver and IR-UWB antenna. It also prevents antenna radiation from

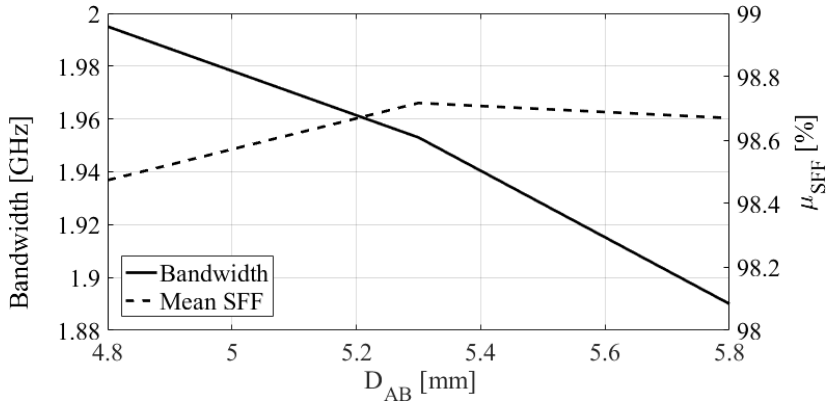

Figure 3.4: Impedance bandwidth and mean system fidelity factor, μ_{SFF}, for varying slot widths D_{AB}.

coupling into the active UWB transceiver circuitry. In order to guarantee sufficient electrical contact and to provide correct alignment between the subsequent PCB layers, alignment pins are used to tighten the boards.

3.2.5 Antenna dimensions

For the coupled half-mode AFSIW cavity-backed slot antenna, the fundamental resonant frequencies of each half-mode cavity are given by

$$f_{110} = \frac{c}{2\pi}\sqrt{\left(\frac{\pi}{W_{cavity}}\right)^2 + \left(\frac{\pi}{2L_x}\right)^2}, \tag{3.3}$$

with L_x the length (Fig. 3.2(c)) of half-mode cavity A or B [45]. In order to cover the frequency band $[5.9803; 6.9989]$ GHz, the initial resonant frequencies of the lower and upper resonant cavity are chosen to be 5.0 GHz and 8.5 GHz respectively. After frequency domain optimization in CST Design Studio for the parameters f_{res1}, f_{res2}, L_{feed} and D_{AB}, an optimal impedance bandwidth is achieved for an f_{res1} and f_{res2} of 5.172 GHz and 8.529 GHz, respectively.

A sensitivity analysis revealed that the slot width D_{AB} has a significant influence on the antenna performance in both the frequency domain and the time domain. Fig. 3.4 shows the -10 dB impedance bandwidth and mean system fidelity factor, μ_{SFF}, averaged over the angles of interest, for a varying slot width D_{AB}. On the one hand, it can be seen that an increase in slot width gives rise to a decrease in impedance bandwidth. On the other hand, the μ_{SFF} is maximized by setting the slot width D_{AB} to an intermediate value. Evidently, the slot width D_{AB} is an important parameter in both frequency-domain and time-domain optimization. Therefore, a multi-objective optimization is performed for the parameters D_{AB} and L_{feed}, finding the

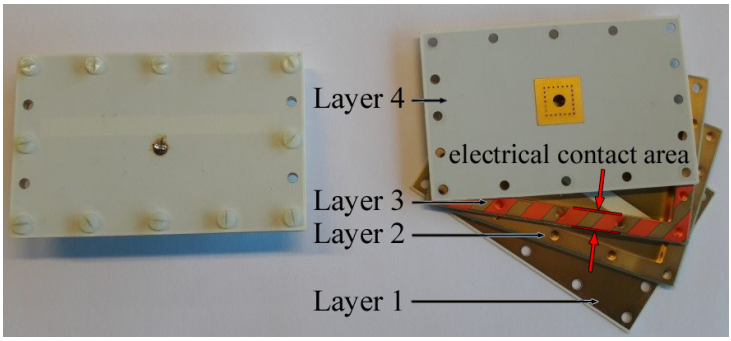

(a)

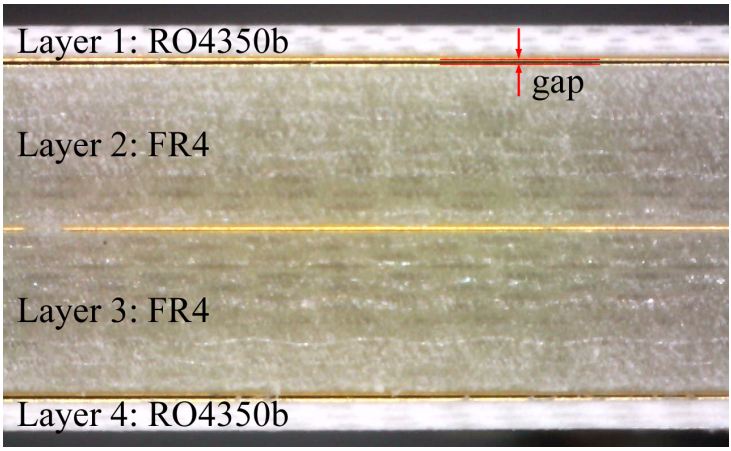

(b)

Figure 3.5: Prototype of AFSIW cavity-backed slot antenna: top view (a) and side view (b).

optimal point on the Pareto front, yielding the highest mean system fidelity factor for an acceptable impedance bandwidth. Furthermore, the system fidelity factor may not drop below the threshold value of 98 % for all angles of interest in both channels 5 and 7, yielding an optimal slot width D_{AB} of 5.3 mm. The final antenna dimensions are given in table 3.1. Fig. 3.5(a) shows a prototype of the optimized AFSIW cavity-backed slot antenna. This design requires two 1.55-mm-thick FR4 PCB boards to form the copper-plated antenna side walls. An electrical contact area width of 6.00 mm was selected, as indicated in Fig. 3.3 and Fig. 3.5(a), to guarantee sufficient electrical contact between subsequent PCB-layers. Furthermore, the air gap between subsequent layers, shown in Fig. 3.5(b), is smaller than $10\mu m$. Simulations have shown that this gap size does not reduce the antenna performance. After assembly, the total antenna height equals 3.20 mm, because of the high-frequency RO4350b laminates on the top and bottom wall of the antenna.

Table 3.1: Antenna dimensions for the antenna prototypes implemented in AFSIW and DFSIW technology.

Parameter	AFSIW antenna [mm]	DFSIW antenna [mm]
W_{cavity}	41.66	30.00
L_B	9.70	6.58
L_A	20.20	10.39
H_{cavity}	3.17	4.00
D_{AB}	5.30	4.20
L_{feed}	14.90	6.39

3.3 AFSIW versus DFSIW

For comparison, also a half-mode cavity-backed slot antenna in DFSIW technology has been designed and optimized to cover the specified frequency band of operation. The DFSIW antenna's simulation model is constructed by stacking four layers of Rogers 4350 ($\epsilon_r = 3.66$, $h_{sub} = 1.0mm$), and by applying vias with 2.00 mm diameter spaced at 3.50 mm from each other.

3.3.1 Form factor

As can be seen from table 3.1, the dimensions of the AFSIW cavity are slightly larger than those of its DFSIW counterparts. On the one hand, the dimensions of the AFSIW cavity increase when reducing the dielectric constant of the substrate to one. On the other hand, the use of solid walls reduces the size of the AFSIW cavity compared to its DFSIW equivalent. The amount of reduction in size by the latter depends on the diameter of the vias used in the DFSIW and their spacing.

3.3.2 Bandwidth

The use of AFSIW technology, in which the dielectric substrate inside the cavity is replaced by air, induces three effects related to the antenna bandwidth performance: a decrease in electrical cavity height, being the height with respect to the wavelength, an increase of the Q-factor of both half-mode cavities and a decrease in Q of the aperture between the two half-mode cavities, mimicking the virtual magnetic wall. These effects are discussed into more depth in the remainder of this section.

The decrease of the electrical cavity height is a result of the increase of the effective wavelength λ_{eff}. Inherently, this lower proportionate cavity height reduces the antenna impedance bandwidth, as specified in [38]. This effect can also be seen in Fig. 3.6(a), showing the relation between the fractional cavity height, $H_{cavity,frac} = H_{cavity}/\lambda_0$, with λ_0 the free-space wavelength of the center frequency, and the maximum impedance bandwidth, for both the AFSIW and DFSIW technology. Furthermore, removing the dielectric substrate inside the half-mode

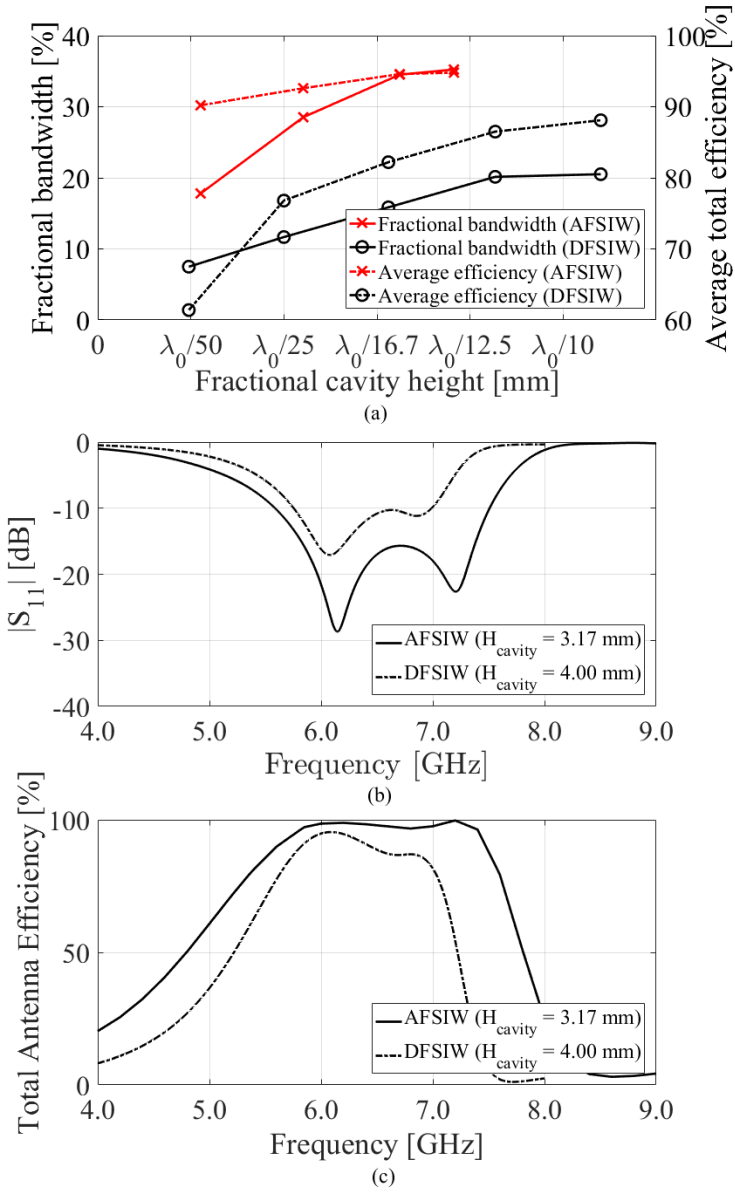

Figure 3.6: Comparison between AFSIW and DFSIW cavity-backed slot antennas, based on simulation of the antennas in Table 3.1: (a) Influence of cavity height on impedance bandwidth and total antenna efficiency. (b) Reflection coefficient w.r.t. 50Ω. (c) Total antenna efficiency.

cavities eliminates substrate losses, results in a higher unloaded Q and a smaller impedance bandwidth. Finally, we consider the influence of the aperture on the antenna impedance bandwidth. As stated in [46], a decrease in permittivity of the substrate underneath the aperture causes a decrease of the aperture Q. Simulations with dielectric-filled half-mode cavities and an air-filled aperture have shown that the increase in bandwidth, induced by the decrease in aperture Q, is substantially greater than the decrease in bandwidth caused by the two former effects. Taking into account all effects, the impedance bandwidth is greatly enhanced by implementing the coupled half-mode cavity-backed slot antenna in AFSIW technology, as observed in Fig. 3.6(b).

3.3.3 Radiation efficiency

The AFSIW technology also yields a substantial improvement in radiation efficiency, compared to its DFSIW counterpart. This effect can be attributed to the following facts: a lack of dielectric losses, a reduction in ohmic losses owing to reduced surface roughness, and the absence of side wall leakage. By removing the lossy substrates, present in standard manufacturing technology, and by replacing them by air, the dielectric losses are minimized. Furthermore, [29] shows that, in case of DFSIW, the inner surface roughness of the copper foil has to be taken into account, whereas for AFSIW the outer surface roughness must be considered. As the outer surface roughness of the copper foil is smaller than the inner surface roughness, ohmic losses are reduced by implementing the antenna in AFSIW technology. Moreover, as seen in Fig. 3.6(a), choosing a larger cavity height, by stacking multiple sidewall layers on top of each other, reduces ohmic losses even further [47]. Finally, by using solid side walls, no electromagnetic energy can leak through the via walls used in conventional DFSIW technology, thereby significantly reducing losses and radiation in undesired directions.

Considering these improvements, the use of AFSIW technology yields a vast increase in radiation efficiency. This hypothesis is confirmed by simulation results, depicted in Fig. 3.6(c), showing that the DFSIW antenna reaches a maximum total efficiency of 95.36 % at 6.10 GHz, whereas its AFSIW counterpart exhibits a total simulated efficiency higher than 97.0 % in the complete $[5.80; 7.40]$ GHz band. Taking into account the frequency-domain limitations of the DFSIW implementation of the antenna, and because the four-layer DFSIW antenna is not poolable, leading to excessive production costs, the fabrication of a DFSIW prototype is not pursued. However, the relevant additional simulation results of the DFSIW antenna will be given in the following section.

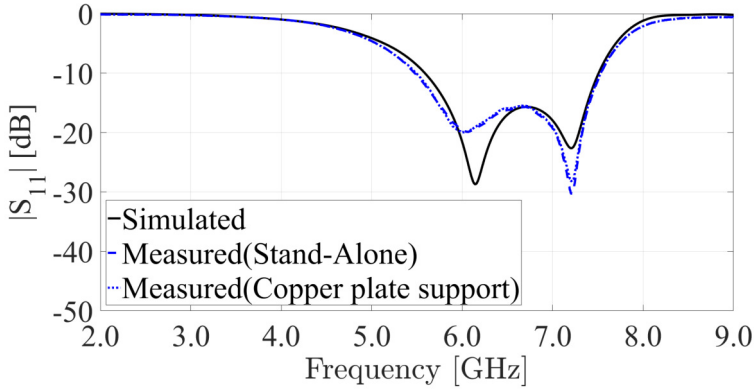

Figure 3.7: Reflection coefficients w.r.t. 50 Ω of the [5.60; 7.50] GHz-band coupled half-mode AFSIW cavity-backed slot antenna, under different operating conditions.

3.4 Simulation and Measurement Results

3.4.1 Frequency-domain antenna parameters

First, the antenna was measured stand-alone in an anechoic chamber. Fig. 3.7 shows that the simulated and measured reflection coefficients are in good agreement. Good impedance matching with respect to $Z_0 = 50\Omega$ from 5.58 GHz to 7.50 GHz can be observed, yielding a -10 dB impedance bandwidth of 1.92 GHz or 29.4 %. Impedance matching in the [5.9803; 6.9989] GHz band is guaranteed by implementing frequency margins of at least 300 MHz, to account for inaccuracies in the fabrication and alignment process. Fig. 3.8 depicts the simulated and measured total antenna efficiency, determined through the directivity/gain method[48]. It demonstrates that the total antenna efficiency is always higher than the required 85 %, indicating highly efficient antenna operation. The slight discrepancy between simulation and measurement results is due to the measurement accuracy. Nonetheless, a good agreement between simulations and measurements is obtained.

Fig. 3.9 shows the simulated and measured co- and cross-polarization radiation patterns in the azimuth (xz-plane) and elevation plane (yz-plane) of the antenna, as depicted in Fig. 3.2(c), at the lower, center, and upper frequency of UWB channel 7. A very good agreement between measurements and simulations is observed. This proves that our optimized design provides a gain radiation pattern that hardly changes over the desired UWB channels, thereby minimizing direction-specific distortion of UWB waveforms. The excellent antenna performance in the frequency domain is also demonstrated in Table 3.2. Table 3.2 depicts the simulated and measured antenna gains along broadside, the FTBR, the total antenna efficiency and the HPBW in the azimuth and elevation plane at the three frequencies under

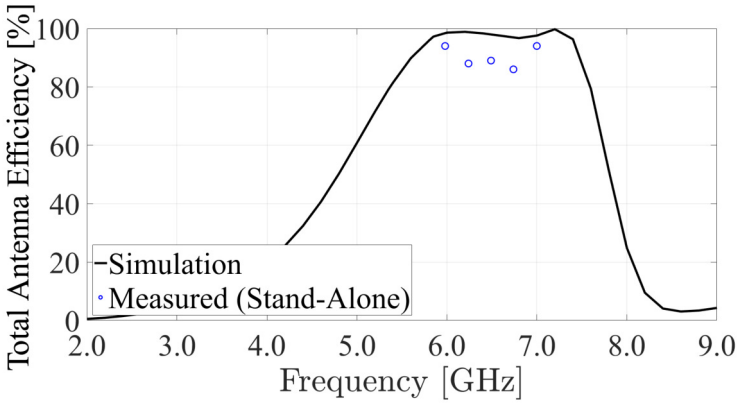

Figure 3.8: Measured and simulated total antenna efficiency of the AFSIW cavity-backed slot antenna that operates in the [5.60; 7.50] GHz-band, as a function of frequency.

Table 3.2: Simulated and measured frequency-domain characteristics. (a) Simulation, (b) Free-space measurement.

Frequency [GHz]	5.980		6.490		6.999	
	(a)	(b)	(a)	(b)	(a)	(b)
Gain [dBi]	6.9	6.9	6.8	6.3	6.9	6.6
FTBR [dB]	13.6	13.1	15.1	13.1	16.0	12.1
Antenna efficiency [%]	99.2	94.0	97.3	89.0	98.0	92.0
HPBW [°]						
Azimuth plane	61	55	61	65	60	60
Elevation plane	95	105	97	110	101	110

study per UWB channel.

In addition, the antenna was measured in an anechoic chamber when mounted on a copper plate (with maximal dimensions of 35x35 cm due to weight limitations of the positioner) to mimic the worst-case deployment scenario (a perfectly conducting wall or ceiling serving as antenna platform). Fig. 3.7 and Fig. 3.9 prove that, even under such a worst-case deployment scenario, the antenna's impedance matching and radiation performance hardly changes. As a result, the total antenna efficiency also barely changes under the latter conditions. Hence, the proposed antenna provides robust, highly efficient performance in realistic deployment scenarios.

3.4.2 Time-domain antenna parameters

As stated in [31], it is imperative to consider the time-domain characteristics when designing UWB antennas. In this respect, the antenna should be analyzed in a com-

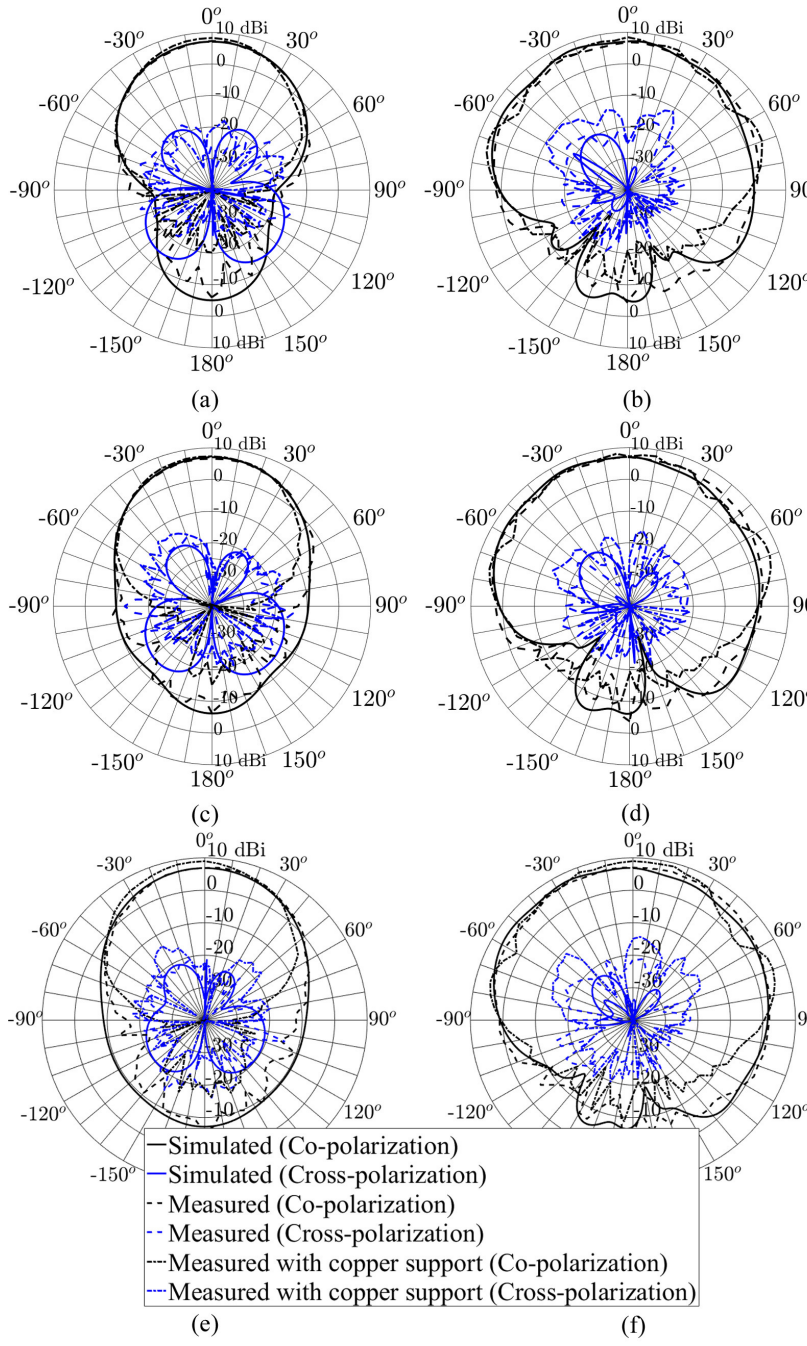

Figure 3.9: Measured and simulated radiation pattern [dBi] in UWB channel 7: at 5.980 GHz in the azimuth (a) and elevation plane (b), at 6.490 GHz in the azimuth (c) and elevation plane (d), and at 6.999 GHz in the azimuth (e) and elevation plane (f).

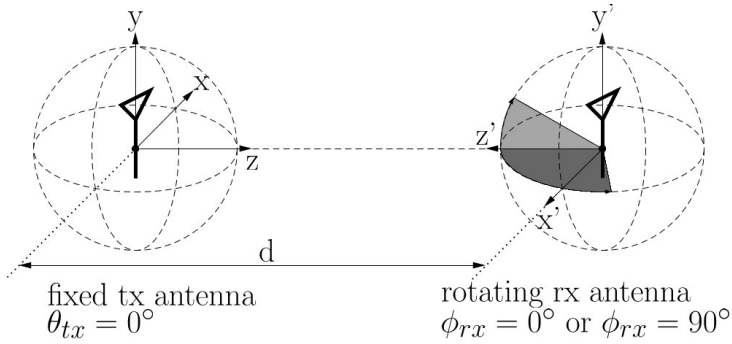

Figure 3.10: System configuration for simulations and measurements with a fixed transmit (tx) antenna and rotating receive (rx) antenna.

plete transmit-receive antenna system. To this end, the coupled half-mode AFSIW cavity-backed slot antenna is used in a specific system configuration, depicted in Fig. 3.10, which is then measured in an anechoic chamber. To mitigate pulse distortion due to higher-order mode excitation in the coaxial measurement cables [49], high-performance coaxial measurement cables with single-mode operation up to at least 26.5 GHz were used. Furthermore, measurements are carried out in the frequency domain by performing a frequency sweep from 2 GHz to 9 GHz. In this way, the spectral content of the pulse contains no higher-order mode components after conversion to the time domain. In the setup, our coupled half-mode AFSIW or DFSIW cavity-backed slot antenna serves both as a transmit and receive antenna. In both simulations and measurements, the distance between both antennas, d, is 5.12 m. In order to analyze the relative group delay, the SFF and the Time of Arrival (ToA) variations in the azimuth and elevation plane, the receive antenna is rotated around its x-axis ($\phi_{rx} = 0°$) and y-axis ($\phi_{rx} = 90°$), respectively. Remark that the transmit antenna always transmits along broadside, implying $\theta_{tx} = 0°$.

The time-domain characterization of the antenna relies on Gaussian pulses, obtained by taking the inverse discrete Fourier transform of its Gaussian spectrum [50], defined by

$$G(f) = \frac{1}{\sigma\sqrt{2\pi}} e^{-\frac{(f-\mu)^2}{2\sigma^2}}, \tag{3.4}$$

with $\mu = f_{center}$ and $\sigma = \frac{BW}{\sqrt{8\ln 10}}$. The parameters f_{center} and BW correspond to the center frequency and bandwidth of the relevant UWB channels, here channels 5 ($\mu = 6489.6$ MHz, $\sigma = 116.3$ MHz) and 7 ($\mu = 6489.6$ MHz, $\sigma = 252.0$ MHz), in the IEEE 802.15.4a-2011 standard. The pulse shapes and their positive envelope for channel 5 and 7 are depicted in Fig. 3.11(a) and 3.11(b), respectively. Each pulse is cut off after the pulse amplitude drops by 50 dB below its maximum value.

Fig. 3.12 shows the simulated and measured SFF for channels 5 and 7. When applying the 98 % SFF criterion, it is found that the antenna meets the requirements

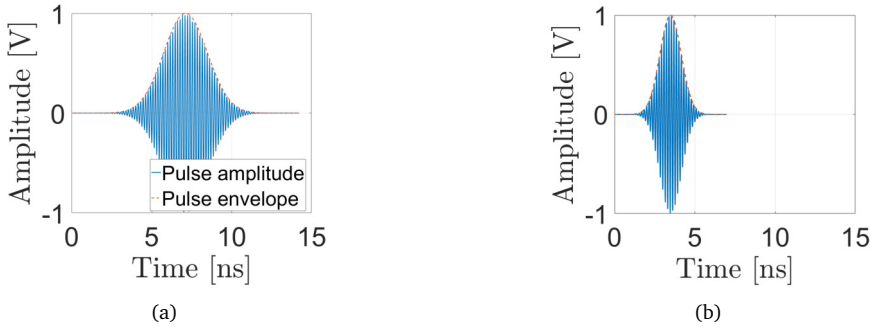

Figure 3.11: Pulse shapes and their positive envelope used for time domain characterization of the antenna. (a) Channel 5. (b) Channel 7.

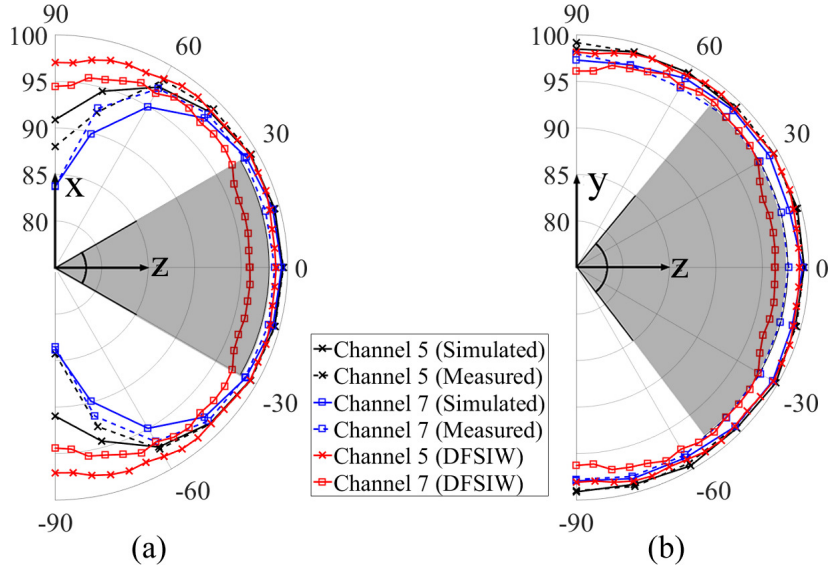

Figure 3.12: SFF for the channels' 5 and 7 pulse shape in the azimuth (a) and elevation plane (b).

in their respective HPBW, as specified in Table 3.2, indicated by the gray area in Fig. 3.12. Again, a very good agreement between measurements and simulations is observed. As a result, the antenna hardly introduces any pulse distortion for the Gaussian pulses in channels 5 and 7, within its HPBW. Furthermore, Fig. 3.12 also depicts the SFF for the antenna implemented in DFSIW technology. For channel 5, the DFSIW antenna complies with the 98 % SFF criterion. However, for channel 7 the DFSIW antenna does not comply with the 98 % SFF criterion and, hence, AFSIW technology is favored for IR-UWB localization applications.

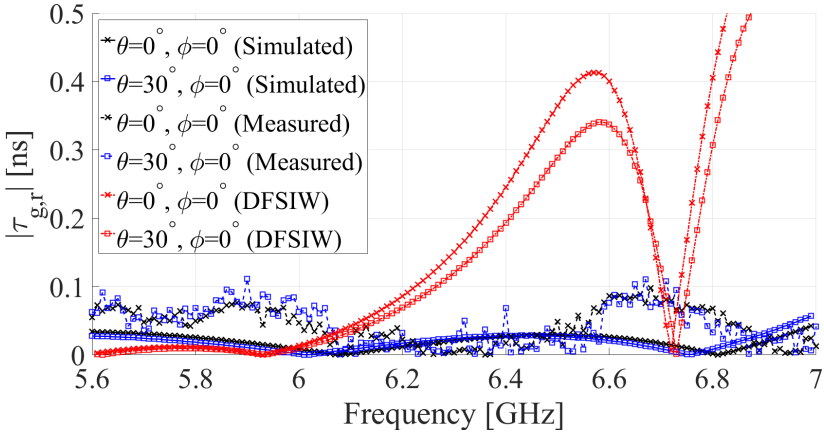

Figure 3.13: $|\tau_{g,r}|$ for the coupled half-mode AFSIW and DFSIW cavity-backed slot antenna system, in the azimuth plane.

Fig. 3.13 and Fig. 3.14 depict the simulated and measured magnitude of the relative group delay, $|\tau_{g,r}|$, for the center and outer angle of arrival of the HPBW in the azimuth and elevation plane, respectively. Due to phase noise introduced by the measurement cables, a slight discrepancy can be observed between measurements and simulations. Nonetheless, we see that the antenna remains compliant with the 100 ps limitation in terms of the magnitude of the relative group delay. Both figures also depict $|\tau_{g,r}|$ for the antenna implemented in DFSIW technology. First of all, it is clear that the AFSIW antenna outperforms its DFSIW counterpart regarding the relative group delay. Furthermore, the DFSIW antenna does not comply to the 100 ps limitation in the entire frequency band of operation, and is, therefore, less suitable for IR-UWB localization applications than its AFSIW counterpart.

In order to verify the potential of our AFSIW antenna in precise IR-UWB ranging applications, the envelope ToA is calculated as the time where the received pulse envelope has its maximal amplitude:

$$t_{ToA} = \arg\max |V_{rx}(t) + j\mathcal{H}\{V_{rx}(t)\}|, \tag{3.5}$$

with $V_{rx}(t)$ the received voltage and $\mathcal{H}$ the Hilbert transform. Fig. 3.15 and 3.16 show the simulated received voltage, as a function of time and orientation, for channels 5 and 7, respectively. The simulated and measured ToA, indicated by the solid and dashed blue line, respectively, are in good agreement. ToA variations smaller than 100 ps can be observed inside the HPBW of the antenna, indicating that the coupled half-mode AFSIW cavity-backed slot antenna is suitable for precise ranging applications.

Finally, the complete system is verified in its application scenario by calculating the distance between transmit and receive antenna from the simulated and measured Time Difference of Arrival (TDoA), which is obtained by subtracting the peak time

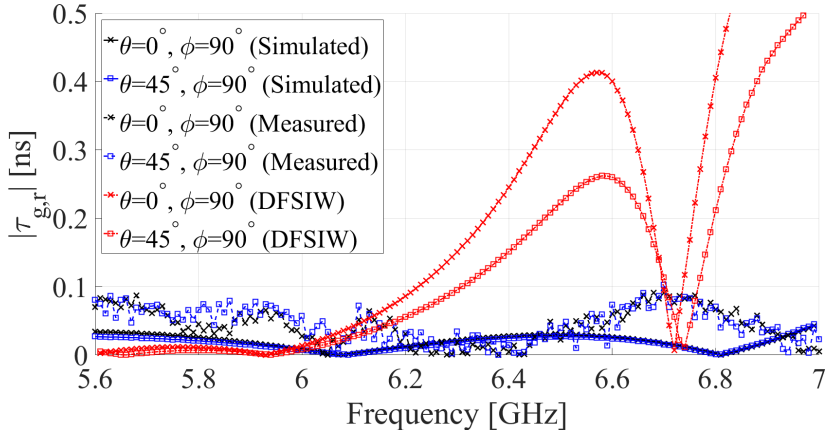

Figure 3.14: $|\tau_{g,r}|$ for the coupled half-mode AFSIW and DFSIW cavity-backed slot antenna system, in the elevation plane.

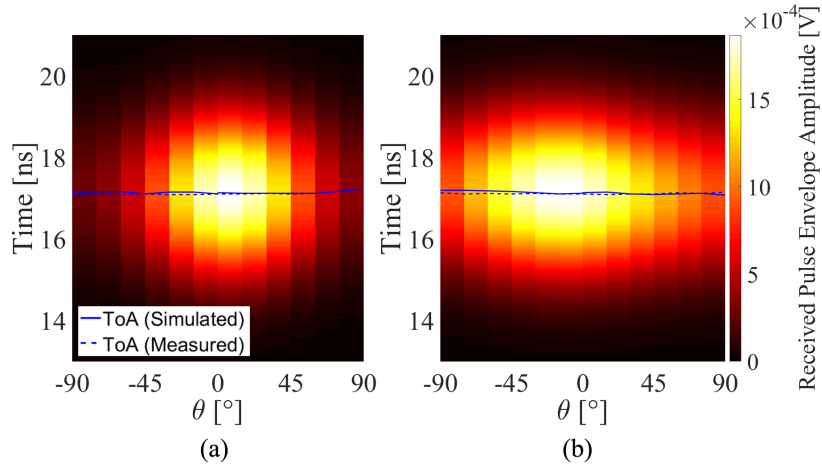

Figure 3.15: Simulated and measured ToA for the coupled half-mode AFSIW cavity-backed slot antenna system, for the channel 5 pulse shape, in the azimuth (a) and elevation plane (b).

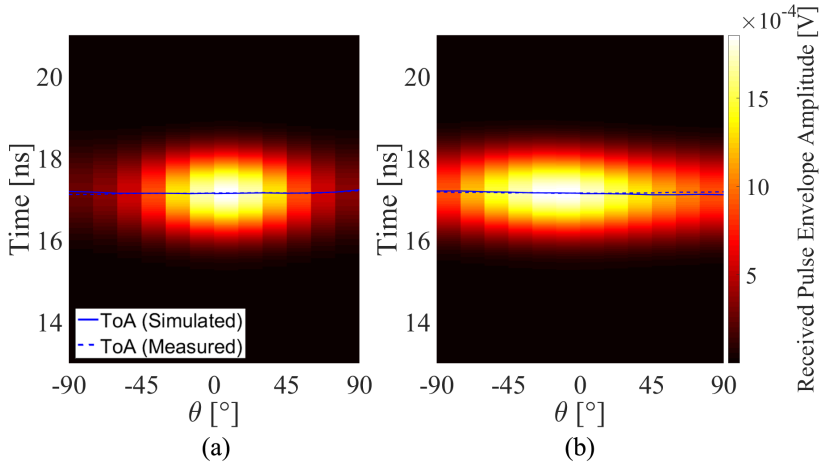

Figure 3.16: Simulated and measured ToA for the coupled half-mode AFSIW cavity-backed slot antenna system, for the channel 7 pulse shape, in the azimuth (a) and elevation plane (b).

of the input pulse envelope from t_{ToA}. The estimated distance between both antennas, as a function of the angle of arrival, is depicted in Fig. 3.17, for channels 5 and 7. Note that noise in the measured ToA gives rise to a small difference between the simulated and measured distance. However, both measured and simulated results yield an accuracy better than 3 cm for both channels 5 and 7 in the HPBW of the antenna, confirming that the coupled half-mode AFSIW cavity-backed slot antenna is suitable for precise ranging applications. Lastly, the estimated distance between the DFSIW antennas is given in Fig. 3.17. Although the required accuracy is achieved for both the AFSIW and DFSIW antenna within their respective HPBW, the ripple in the estimated distance is larger in the latter case. Hence, the AFSIW enables more accurate ranging capabilities, and is, therefore, favored for precision IR-UWB localization applications.

The excellent antenna performance in the time domain is also seen in Table 3.3. Table 3.3 shows the simulated and measured minimal SFF within the antenna's HPBW, the maximum magnitude of the relative group delay and the maximum variation of the ToA within the antenna's HPBW.

3.5 Conclusion

A highly-efficient IR-UWB cavity-backed slot antenna implemented in stacked AFSIW technology was proposed. The design was optimized for precise localization applications operating within the IEEE 802.15.4a-2011 standard, more specifically for the channels 5 and 7, by relying on extensive frequency-domain and time-domain analysis of the antenna's characteristics.

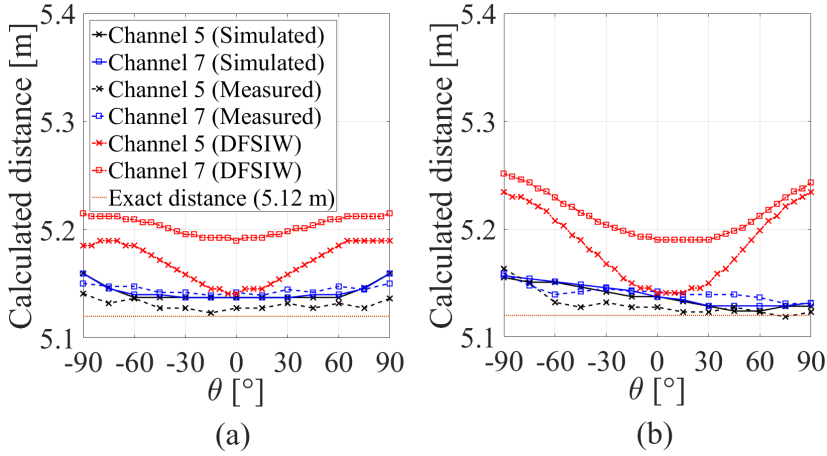

Figure 3.17: Calculated distance based on simulated and measured TDoA for channels 5 and 7, in the azimuth (a) and elevation plane (b).

Table 3.3: Simulated and measured time-domain characteristics within the antenna HPBW. (a) Simulation, (b) Free-space measurement.

	SFF_{min} [%]		$\lvert ø_{g,r,max} \rvert$ [ps]		ΔToA_{max} [ps]	
	(a)	(b)	(a)	(b)	(a)	(b)
Azimuth plane						
Channel 5	99.25	99.28	57.0	110.9	40	30
Channel 7	98.69	98.42			10	20
Elevation plane						
Channel 5	99.07	99.19	44.7	102.5	60	30
Channel 7	98.73	98.03			60	20

Measurements in an anechoic chamber were performed to validate the antenna in free-space conditions in both the frequency and time domain. A very good agreement between frequency-domain simulations and measurements in terms of impedance matching and radiation performance is observed. The ultra-wide bandwidth of 1.92 GHz (29.4 %) ensures coverage of both channels 5 and 7, with a maximal measured gain of 6.9 dBi and a minimal measured antenna efficiency of 89 %. Furthermore, the antenna is validated in a worst-case deployment scenario. The results prove a stable antenna performance in the latter condition. Likewise, a very good agreement between time-domain simulation and measurement results is observed. A minimal SFF of 99.19 % and 98.03 % is measured for channel 5 and 7, respectively. The measured magnitude of the relative group delay remains lower than 100 ps in almost the complete [5.60; 7.00] GHz frequency band. As a result, the estimated distance is accurate up to at least 3 cm.

Furthermore, the difference in performance between the AFSIW and DFSIW tech-

nology is studied. Simulations have shown that the use of AFSIW introduces three effects: an increase in form factor, a vast increase in impedance bandwidth and an increase in radiation efficiency. Time-domain simulations have indicated that the DFSIW is less suited for IR-UWB purposes than its AFSIW counterpart, owing to a lesser SFF and a relative group delay which is not compliant to the 100 ps criterion. In addition to its secondary performance characteristics, the fabrication cost of the DFSIW antenna is much higher than its AFSIW counterpart, because of the expensive high-frequency laminates and the non poolability of the four-layer buildup. Other low-permittivity, low-loss and low-cost high-frequency antenna foam laminates have been considered as well, such as FoamClad RF 100 [51]. Although these laminates allow for similar performance characteristics as the AFSIW technology, they are less suited mass production purposes and do not allow for integration of active IR-UWB electronics. Hence, the antenna implemented in AFSIW technology is favored for precision IR-UWB localization applications.

In conclusion, the simulations and measurements demonstrated that the antenna provides excellent IR-UWB characteristics, even in a worst-case deployment scenario. Furthermore, it is apparent that the antenna implemented in AFSIW technology outperforms its DFSIW counterpart. Hence, to achieve the required accuracy of 3 cm for localization applications the AFSIW antenna is recommended.

References

[1] P. Meissner, E. Leitinger, M. Frohle, and K. Witrisal, "Accurate and Robust Indoor Localization Systems using Ultra-wideband Signals", in *European Navigation Conference (ENC)*, Vienna, Austria, 23-25 Apr. 2013.

[2] W. C. Chung and D. S. Ha, "An Accurate Ultra Wideband (UWB) Ranging for Precision Asset Location", in *IEEE Int. Conf. on Ultra Wideband Systems and Technologies*, Virginia, USA, 16-19 Nov. 2003, pp. 389–393.

[3] R. J. Fontana, E. Richley, and J. Barney, "Commercialization of an Ultra Wideband Precision Asset Location System", in *IEEE Conference on Ultra Wideband Systems and Technologies, 2003*, 2003, pp. 369–373.

[4] O. Novak and C. Charles, "Low-Power UWB Pulse Generators for Biomedical Implants", in *2009 IEEE International Conference on Ultra-Wideband*, 2009, pp. 778–782.

[5] R. Chavez-Santiago, A. Khaleghi, I. Balasingham, and T. A. Ramstad, "Architecture of an Ultra Wideband Wireless Body Area Network for Medical Applications", in *2009 2nd International Symposium on Applied Sciences in Biomedical and Communication Technologies*, 2009, pp. 1–6.

[6] A. Lazaro, D. Girbau, R. Villarino, and A. Ramos, "Vital Signs Monitoring using Impulse based UWB Signal", in *2011 41st European Microwave Conference*, 2011, pp. 135–138.

[7] D. T. Wisland, K. Granhaug, J. R. Pleym, N. Andersen, S. StÃÿa, and H. A. Hjortland, "Remote Monitoring of Vital Signs using a CMOS UWB Radar Transceiver", in *2016 14th IEEE International New Circuits and Systems Conference (NEWCAS)*, 2016, pp. 1–4.

[8] J. M. Lee, J. W. Choi, and S. H. Cho, "Movement Analysis during Sleep using an IR-UWB Radar Sensor", in *2016 IEEE International Conference on Network Infrastructure and Digital Content (IC-NIDC)*, 2016, pp. 486–490.

[9] J. Ryckaert, C. Desset, A. Fort, M. Badaroglu, V. D. Heyn, P. Wambacq, G. V. der Plas, S. Donnay, B. V. Poucke, and B. Gyselinckx, "Ultra-Wide-Band Transmitter for Low-Power Wireless Body Area Networks: Design and Evaluation", *IEEE Transactions on Circuits and Systems I: Regular Papers*, vol. 52, no. 12, pp. 2515–2525, 2005.

[10] J. F. M. Gerrits, J. R. Farserotu, and J. R. Long, "Low-Complexity Ultra-Wide-Band Communications", *IEEE Transactions on Circuits and Systems II: Express Briefs*, vol. 55, no. 4, pp. 329–333, 2008.

[11] W. Wiesbeck, G. Adamiuk, and C. Sturm, "Basic Properties and Design Principles of UWB Antennas", *Proceedings of the IEEE*, vol. 97, no. 2, pp. 372–385, 2009.

[12] S. Lemey and H. Rogier, "SIW Textile Antennas as a novel Technology for UWB RFID tags", in *2014 IEEE RFID-TA*, Tampere, Finland, Sept. 8-9, 2014, pp. 256–260.

[13] V. Sipal, M. John, D. Neirynck, M. McLaughlin, and M. Ammann, "Advent of Practical UWB Localization: (R)Evolution in UWB Antenna Research", in *The 8th European Conference on Antennas and Propagation (EuCAP 2014)*, The Hague, The Netherlands, 6-11 Apr. 2014, pp. 1561–1565.

[14] W. Q. Malik, C. J. Stevens, and D. J. Edwards, "Ultra-wideband Antenna Distortion Compensation", *IEEE Trans. Antennas. Propag.*, vol. 56, no. 7, pp. 1900–1907, 2008.

[15] Y. Shen and M. Z. Win, "Fundamental Limits of Wideband Localization 2014; Part I: A General Framework", *IEEE Transactions on Information Theory*, vol. 56, no. 10, pp. 4956–4980, 2010.

[16] G. Adamiuk, T. Zwick, and W. Wiesbeck, "UWB Antennas for Communication Systems", *Proceedings of the IEEE*, vol. 100, no. 7, pp. 2308–2321, 2012.

[17] O. Caytan, S. Lemey, S. Agneessens, D. Vande Ginste, P. Demeester, C. Loss, R. Salvado, and H. Rogier, "Half-Mode Substrate-Integrated-Waveguide Cavity-Backed Slot Antenna on Cork Substrate", *IEEE Antennas and Wireless Propagation Letters*, vol. 15, pp. 162–165, 2016.

[18] T. Deckmyn, S. Agneessens, A. C. F. Reniers, A. B. Smolders, M. Cauwe, D. V. Ginste, and H. Rogier, "A Novel 60 GHz Wideband Coupled Half-Mode/Quarter-Mode Substrate Integrated Waveguide Antenna", *IEEE Transactions on Antennas and Propagation*, vol. 65, no. 12, pp. 6915–6926, 2017.

[19] A. Belenguer, H. Esteban, and V. E. Boria, "Novel Empty Substrate Integrated Waveguide for High-Performance Microwave Integrated Circuits", *IEEE Transactions on Microwave Theory and Techniques*, vol. 62, no. 4, pp. 832–839, 2014.

[20] J. V. Morro, A. RodrÃguez, A. Belenguer, H. Esteban, and V. Boria, "Multilevel Transition in Empty Substrate Integrated Waveguide", *Electronics Letters*, vol. 52, no. 18, pp. 1543–1544, 2016.

[21] A. Belenguer, J. L. Cano, H. Esteban, E. Artal, and V. E. Boria, "Empty Substrate Integrated Waveguide Technology for E Plane High-Frequency and High-Performance Circuits", *Radio Science*, vol. 52, no. 1, pp. 49–69, 2017.

[22] F. Parment, A. Ghiotto, T. P. Vuong, J. M. Duchamp, and K. Wu, "Ka-band Compact and High-Performance Bandpass Filter based on Multilayer Air-Filled SIW", *Electronics Letters*, vol. 53, no. 7, pp. 486–488, 2017.

[23] ——, "Double Dielectric Slab-Loaded Air-Filled SIW Phase Shifters for High-Performance Millimeter-Wave Integration", *IEEE Transactions on Microwave Theory and Techniques*, vol. 64, no. 9, pp. 2833–2842, 2016.

[24] J. W. Digby, C. E. McIntosh, G. M. Parkhurst, B. M. Towlson, S. Hadjiloucas, J. W. Bowen, J. M. Chamberlain, R. D. Pollard, R. E. Miles, D. P. Steenson, L. S. Karatzas, N. J. Cronin, and S. R. Davies, "Fabrication and Characterization of Micromachined Rectangular Waveguide Components for Use at Millimeter-Wave and Terahertz Frequencies", *IEEE Transactions on Microwave Theory and Techniques*, vol. 48, no. 8, pp. 1293–1302, 2000.

[25] J. Mateo, A. M. Torres, A. Belenguer, and A. L. Borja, "Highly Efficient and Well-Matched Empty Substrate Integrated Waveguide H-Plane Horn Antenna", *IEEE Antennas and Wireless Propagation Letters*, vol. 15, pp. 1510–1513, 2016.

[26] F. Bigelli, D. Mencarelli, M. Farina, G. Venanzoni, P. Scalmati, C. Renghini, and A. Morini, "Design and Fabrication of a Dielectricless Substrate-Integrated Waveguide", *IEEE Transactions on Components, Packaging and Manufacturing Technology*, vol. 6, no. 2, pp. 256–261, 2016.

[27] F. Parment, A. Ghiotto, T. P. Vuong, J. M. Duchamp, and K. Wu, "Millimetre-Wave Air-Filled Substrate Integrated Waveguide Slot Array Antenna", *Electronics Letters*, vol. 53, no. 11, pp. 704–706, 2017.

[28] A. Ghiotto, F. Parment, T. P. Vuong, and K. Wu, "Millimeter-Wave Air-Filled SIW Antipodal Linearly Tapered Slot Antenna", *IEEE Antennas and Wireless Propagation Letters*, vol. 16, pp. 768–771, 2017.

[29] F. Parment, A. Ghiotto, T. P. Vuong, J. M. Duchamp, and K. Wu, "Air-Filled Substrate Integrated Waveguide for Low-Loss and High Power-Handling Millimeter-Wave Substrate Integrated Circuits", *IEEE Transactions on Microwave Theory and Techniques*, vol. 63, no. 4, pp. 1228–1238, 2015.

[30] "IEEE Standard for Local and Metropolitan Area Networks–Part 15.4: Low-Rate Wireless Personal Area Networks (LR-WPANs)", *IEEE Std 802.15.4-2011 (Revision of IEEE Std 802.15.4-2006)*, pp. 1–314, 2011.

[31] A. Shlivinski, E. Heyman, and R. Kastner, "Antenna Characterization in the Time Domain", *IEEE Transactions on Antennas and Propagation*, vol. 45, no. 7, pp. 1140–1149, 1997.

[32] D.-H. Kwon, "Effect of Antenna Gain and Group Delay Variations on Pulse-Preserving Capabilities of Ultrawideband Antennas", *IEEE Transactions on Antennas and Propagation*, vol. 54, no. 8, pp. 2208–2215, 2006.

[33] D. Lamensdorf and L. Susman, "Baseband-Pulse-Antenna Techniques", *IEEE Antennas and Propagation Magazine*, vol. 36, no. 1, pp. 20–30, 1994.

[34] "APH0007 Antenna Selection / Design Guide for DW1000", DecaWave, Tech. Rep., 2014.

[35] J. Galejs, "Admittance of a Rectangular Slot which is backed by a Rectangular Cavity", *IEEE Transactions on Antennas and Propagation*, vol. 11, no. 2, pp. 119–126, 1963.

[36] G. Luo, T. Wang, and X. Zhang, "Review of Low Profile Substrate Integrated Waveguide Cavity Backed Antennas", *International Journal of Antennas and Propagation*, 2013.

[37] F. Giuppi, A. Georgiadis, A. Collado, M. Bozzi, and L. Perregrini, "Tunable SIW Cavity Backed Active Antenna Oscillator", *Electronics Letters*, vol. 46, no. 15, pp. 1053–1055, 2010.

[38] G. Q. Luo, Z. F. Hu, L. X. Dong, and L. L. Sun, "Planar Slot Antenna Backed by Substrate Integrated Waveguide Cavity", *IEEE Antennas and Wireless Propagation Letters*, vol. 7, pp. 236–239, 2008.

[39] Q. Lai, C. Fumeaux, W. Hong, and R. Vahldieck, "Characterization of the Propagation Properties of the Half-Mode Substrate Integrated Waveguide", *IEEE Transactions on Microwave Theory and Techniques*, vol. 57, no. 8, pp. 1996–2004, 2009.

[40] I. S. S. Lima, F. Parment, A. Ghiotto, T. P. Vuong, and K. Wu, "Broadband Dielectric-to-Half-Mode Air-Filled Substrate Integrated Waveguide Transition", *IEEE Microwave and Wireless Components Letters*, vol. 26, no. 6, pp. 383–385, 2016.

[41] S. S. Chakravarthy, N. Sarveshwaran, S. Sriharini, and M. Shanmugapriya, "Comparative Study on Different Feeding Techniques of Rectangular Patch Antenna", in *2016 Thirteenth International Conference on Wireless and Optical Communications Networks (WOCN)*, 2016, pp. 1–6.

[42] J.-S. Hong and M. J. Lancaster, "Couplings of Microstrip Square Open-Loop Resonators for Cross-Coupled Planar Microwave Filters", *IEEE Transactions on Microwave Theory and Techniques*, vol. 44, no. 11, pp. 2099–2109, 1996.

[43] "FR402 Tetrafunctional Epoxy Laminateand Prepreg", Isola, Tech. Rep., 2017.

[44] "RO4000 Series High Frequency Circuit Materials", Rogers corporation, Tech. Rep., 2017.

[45] D. Pozar, *Microwave Engineering*. Wiley, 2012, ch. 6.

[46] S. Yun, D. Y. Kim, and S. Nam, "Bandwidth and Efficiency Enhancement of Cavity-Backed Slot Antenna Using a Substrate Removal", *IEEE Antennas and Wireless Propagation Letters*, vol. 11, pp. 1458–1461, 2012.

[47] M. Bozzi, M. Pasian, L. Perregrini, and K. Wu, "On the Losses in Substrate-Integrated Waveguides and Cavities", *International Journal of Microwave and Wireless Technologies*, vol. 1, no. 5, pp. 395–401, 2009.

[48] D. M. Pozar and B. Kaufman, "Comparison of Three Methods for the Measurement of Printed Antenna Efficiency", *IEEE Transactions on Antennas and Propagation*, vol. 36, no. 1, pp. 136–139, 1988.

[49] G. Wen, "A Time-Domain Theory of Waveguide", *Progress In Electromagnetics Research*, vol. 59, pp. 267–297, 2006.

[50] D. D. Wentzloff and A. P. Chandrakasan, "Gaussian Pulse Generators for Subbanded Ultra-Wideband Transmitters", *IEEE Transactions on Microwave Theory and Techniques*, vol. 54, no. 4, pp. 1647–1655, 2006.

[51] "FoamClad RF 100: Low Dielectric Constant Lightweight Laminate", Arlon, Tech. Rep., 2003.

4

Range Estimation Biasing: Planar Sectoral Antenna for IR-UWB Localization with Minimal Range Estimation Biasing

Abstract

A planar sectoral antenna is presented, optimized for highly precise Impulse Radio Ultra-Wideband (IR-UWB) indoor localization with minimal distance estimation biasing errors. By judiciously combining two planar inverted-F antenna elements into one footprint, a large Half-Power Beamwidth (HPBW) is obtained in the [3.2448 – 4.7424] GHz band, thereby covering channels 1 to 4 of the IEEE 802.15.4a-2011 standard. Through system-level optimization, the System Fidelity Factor (SFF) is maximized for a minimal value of at least 90% within its entire HPBW, while minimizing the orientation-specific Distance Estimation Error (DEE) down to 10 mm. To validate the antenna performance, measurements have been performed in both the frequency and time domain, showing a HPBW larger than 120° in the complete frequency-band of operation and an SFF larger than 90% and a DEE lower than 4 mm within the antenna's HPBW.

4.1 Introduction

With the rapid advent of Industry 4.0 in high-tech industrial environments, tangible research results on state-of-the-art sensor systems are of major importance to facilitate a steady transition into this new industrial revolution. A great example can be found in the domain of indoor localization, demonstrating major advantages in different sectors and on different scales [1], [2]. Here, IR-UWB localization systems yield superior accuracy, attributed to their resilience against narrowband interference and detrimental multipath effects [3]. Furthermore, because of the development of low-cost and accurate IR-UWB localization sensor platforms [4], IR-UWB indoor localization has become a driving force for innovation in many applications in healthcare [5], robot navigation [6], [7], etc. However, with IR-UWB localization systems entering the stage of mass production, new research challenges associated with the integration of IR-UWB antennas in practical indoor localization systems emerge to ensure cm-level-precision accuracy to a large number of users in the harsh and challenging Industry 4.0 environment [8], [9].

The use of sub-nanosecond pulses in IR-UWB localization systems imposes a substantially different antenna design procedure when compared to narrowband technology. As stated in [10], [11], both the frequency-domain and system-level performance of the antenna should be optimized, where the latter focuses primarily on the pulse distortion introduced by the antenna system. However, recent studies have demonstrated that not only pulse distortion, but also the orientation-dependent time delay introduced by the antenna should be investigated at a system level [12]–[15]. These delays were investigated in [12], [13], [15] through time-domain measurements, showing an antenna-induced orientation-dependent range estimation bias up to 30 cm. In [14], the influence of this range estimation bias was studied for angle-of-arrival estimation. Furthermore, [16]–[19] report that certain IR-UWB hardware platforms exhibit a correlation between range estimation bias and received power, thereby requiring minimal antenna gain variation within the targeted field of view.

In this work, a planar sectoral coupled Planar Inverted-F Antenna (PIFA) for IR-UWB localization is proposed, operational in the [3.2448 – 4.7424] GHz band, thereby covering channels 1 through 4 of the IEEE 802.15.4a-2011 standard [20]. Inspired by the topology in [21] and by means of a rigorous analysis and optimization process, both in the frequency-domain and on a system level, a large HPBW and a minimal DEE within that HPBW is obtained. The antenna performance is validated by both frequency- and time-domain measurements, thereby confirming the potential of the proposed antenna for IR-UWB indoor localization systems.

A plethora of antennas for IR-UWB localization have been extensively analyzed in literature, both with omnidirectional [22]–[24] and hemispherical [25]–[28] radiation properties. Analyzing the frequency domain radiation characteristics of [22]–[24], it is apparent that an omnidirectional antenna is not suited as a sec-

tor antenna. To mitigate interference in sectorized network topologies, several omnidirectional antennas were equipped with a reflector to shape the radiation pattern towards the targeted cell area [25], [26]. However, this approach creates highly directive antennas and may cause strong variations in the radiation pattern as a function of frequency. In [27], a hemispherical antenna is presented, achieving a HPBW larger than 90° and showing a fidelity factor of 80% in broadside. Unfortunately, a gain as low as -15 dBi is reported, rendering it unsuitable for the envisioned application scenario. In terms of time-domain characteristics, most research imposes a design requirement of a SFF higher than 50%, as defined in [10]. However, the state-of-the-art IR-UWB antennas easily reach a measured SFF higher than 80% [22]–[24], [27]. In [26], [28], SFFs up to 91% and 95% are reported, respectively. Furthermore, a ranging estimation bias of 50 mm is reported in [28], showing that a high system fidelity factor does not necessarily result in a low ranging estimation bias and that specific system-level time-domain optimization is required to optimize this parameter. Alternatively, in terms of narrowband topologies, magnetic dipoles, as analyzed in [21], provide highly beneficial radiation properties for sectorized antenna arrays. Despite the favorable radiation characteristics, the impedance bandwidth of 2% is not sufficient for IR-UWB applications. However, by adopting an air-substrate PIFA topology and leveraging mode-bifurcation, ultra-wideband operation is achieved. Furthermore, a time-domain optimization is performed utilizing an in-house modular full-wave/circuit co-optimization framework [29] to maximize the system fidelity factor and minimize the range estimation bias.

The remainder of this letter is organized as follows. In Section 4.2, both the frequency- and time-domain antenna design requirements are discussed. Section 4.3 elaborates on the antenna topology, its operation principle and summarizes the final antenna specifications. Next, Section 4.4 provides an overview of both the frequency- and time-domain simulation and measurement results. Finally, a conclusion is presented in Section 4.5.

4.2 Design Requirements

A sectoral IR-UWB anchor antenna is designed for IR-UWB localization applications in the $[3.2448 - 4.7424]$ GHz frequency band. Thereby, the antenna covers channels 1 to 4 of the IEEE 802.15.4a-2011 standard, frequently adopted in academic and commercial localization applications [30]–[33]. In the following, all design requirements in the frequency domain are imposed over the entire specified frequency band. The magnitude of the reflection coefficient, $|S_{1,1}|$, with respect to 50 Ω, should remain below -10 dB. Furthermore, a total antenna efficiency above 85% is targeted to maximize range and minimize power consumption. Finally, in order to comfortably provide a 360° coverage in a three-element sectorized antenna array, while minimizing inter-antenna interference, a HPBW of 120° in the azimuth plane and a Front-to-Back Ratio (FTBR) larger than 10 dB is imposed on

the unit antenna element.

As mentioned in [10], [11], time-domain optimization is imperative to achieve robust and excellent system performance in IR-UWB localization applications. Special care is devoted to minimizing pulse distortion and orientation-specific distance estimation biasing errors, introduced by the antenna system. The pulse distortion is characterized the SFF, defined by [10]

$$SFF = \max_{t} \left| \frac{\int_{t_0}^{t_n} s(\tau)x(\tau+t)d\tau}{\sqrt{\int_{t_0}^{t_n} s^2(\tau)d\tau \int_{t_0}^{t_n} x^2(\tau)d\tau}} \right|, \tag{4.1}$$

with $s(t)$ and $x(t)$ the input and output pulse, respectively. The algorithm used to estimate the range and, hence, the orientation-specific distance estimation biasing error, $d_{est}(\theta,\phi)$, is defined by

$$d_{est}(\theta,\phi) = (t_{max}(\theta,\phi) - t_{max}(0,0))\,c, \tag{4.2}$$

where t_{max} is the time delay that maximizes the SFF for a certain orientation (θ,ϕ) and c is the speed of light. As such, for a given antenna system, the output pulse needs to be calculated for each orientation of the antenna under test (AUT). To guarantee high-precision localization with minimal orientation-specific biasing errors, both an SFF higher than 90% and a DEE, $|d_{est}|$, lower than 10 mm are imposed.

4.3 Sectoral Coupled Planar Inverted-F Antenna: Topology and Operation Principle

4.3.1 Ultra-Wideband Half-Power Beamwidth Optimization

A suitable antenna topology with favorable inherent radiation properties is required and needs to be tailored to satisfy the aforementioned design requirements. A promising candidate is the microstrip patch antenna, because of its low profile, wide HPBW and large FTBR [34]–[38]. In addition, [39] demonstrates that the HPBW can be further enhanced by cutting the patch in half along its E-plane and shorting the patch along this cut. Although the mode profile inside the resulting planar inverted-F antenna is identical to half of the TM01-mode in the original patch, the radiation characteristics have slightly changed. By only retaining half of the TM01-mode, the contribution of both sidewalls to the radiation pattern increases substantially and, as a result, the HPBW enlarges compared to a patch antenna [39].

Evidently, the PIFA exhibits advantageous radiation properties and, as such, is selected as the starting point for this design. However, despite the potential of the PIFA, its inherent narrowband behaviour remains a major drawback for IR-UWB

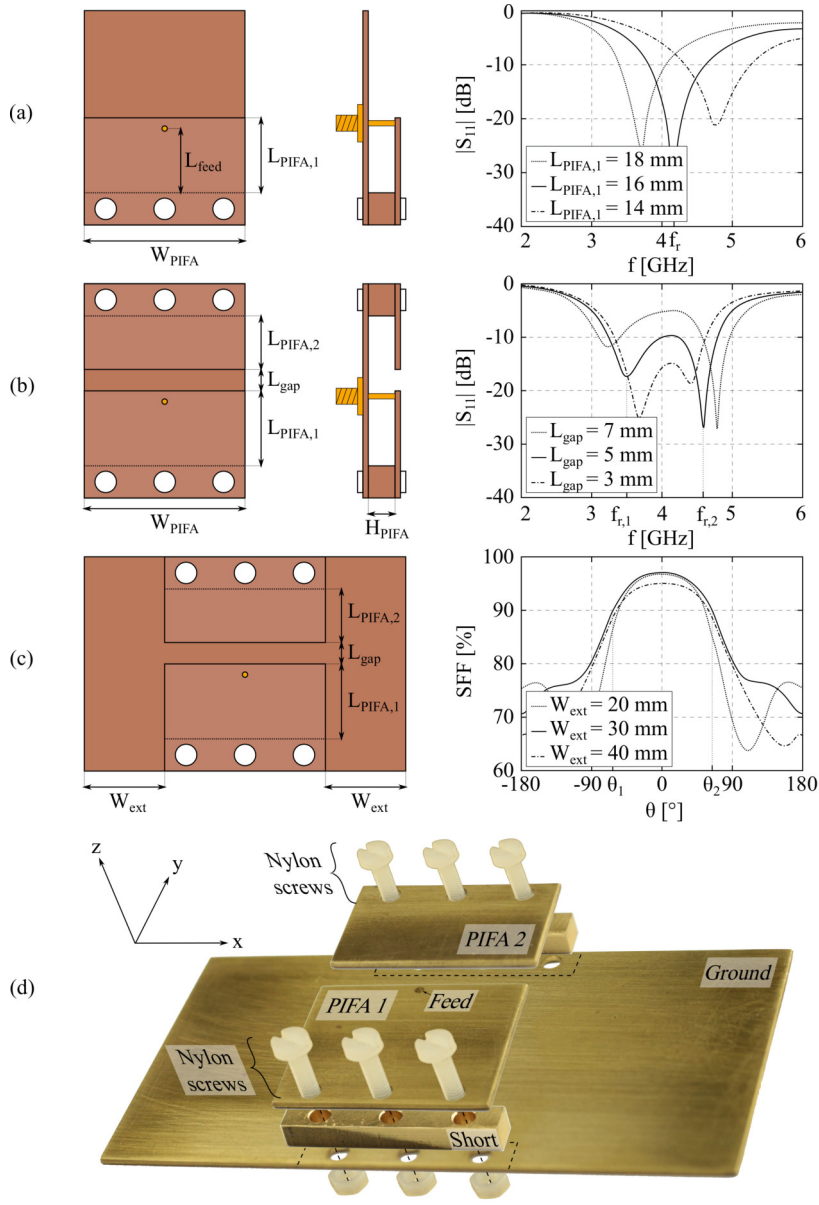

Figure 4.1: Design process of the coupled PIFA IR-UWB antenna: Single PIFA (a), coupled PIFA (b), ground plane extension (c) and exploded view of the prototype (d). The parameter sweeps are obtained with the final antenna dimensions, specified in Table 4.1, unless stated otherwise.

applications. To resolve this issue, a technique called mode-bifurcation [11] is exploited. The resulting coupled PIFA antenna topology, its design flow and implementation is illustrated in Fig. 4.1, depicting both the top and side views in each step, as well as the effect of antenna dimensions on the relevant antenna characteristics.

Initially, as depicted in Fig. 4.1(a), a single PIFA element, fed by a coaxial feed, is impedance-matched to 50 Ω at a frequency $f_r = 4$ GHz. By optimizing the width (W_{PIFA}), length ($L_{PIFA,1}$) and feed position ($L_{feed} = 10.5$ mm) of the PIFA, the antenna exhibits a resonance at 4 GHz. Next, a second identical PIFA element is added to the antenna footprint, as shown in Fig. 4.1(b). The addition of the second PIFA element induces mode-bifurcation, resulting in two distinct resonant peaks, $f_{r,1}$ and $f_{r,2}$, with $f_{r,1} < f_r < f_{r,2}$. The frequencies $f_{r,1}$ and $f_{r,2}$ and, hence, the impedance bandwidth are controlled by varying the amount of coupling between both PIFA elements. By carefully choosing the PIFA height (H_{PIFA}), the gap between both PIFA elements (L_{gap}) and their respective resonant frequencies, controlled by $L_{PIFA,1}$ and $L_{PIFA,2}$, the shift in resonant frequencies can be adjusted to realize a reflection coefficient, $|S_{1,1}|$, below -10 dB in the complete frequency band of operation. Note that the second PIFA element is not fed directly and is only excited by proximity coupling with the first PIFA element. Additionally, remark that varying L_{gap} changes the total antenna length since we keep the values of $L_{PIFA,1}$ and $L_{PIFA,2}$ fixed during the process. Finally, as illustrated by Fig. 4.1(c), a ground plane extension is added to tailor the radiation pattern to the intended deployment scenario. Tuning W_{ext} allows to optimize for a HPBW in the azimuth plane (xz-plane) of 120°, while maintaining a FTBR larger than 10 dB.

4.3.2 Coupled Inverted-F Antenna and Time-Domain Performance

In addition to the conventional frequency-domain optimization, a system-oriented time-domain optimization is required to guarantee robust and accurate performance for IR-UWB localization applications. This optimization is performed based on a pulse defined by [20]

$$s(t) = \cos(2\pi f_0 t)\frac{2}{\pi\sqrt{T_p}}\frac{\cos(1.5\pi t/T_p) + \frac{\sin(0.5\pi t/T_p)}{2t/T_p}}{1-(2t/T_p)^2}, \tag{4.3}$$

with $f_0 = 4.25$ GHz the pulse carrier frequency and $T_p = 0.92$ ns the pulse duration, thereby covering channels 1 through 4. The pulse is transmitted by a coupled half-mode cavity backed slot antenna, developed in [40], and is received by the Antenna Under Test (AUT) presented in this work. Finally, an in-house modular full-wave/circuit co-optimization framework [29] is utilized to obtain the required time-domain simulation results.

On the one hand, an extensive parameter analysis revealed that the SFF and, hence, the pulse distortion, is predominantly affected by the mode-bifurcation. On the other hand, the AUT's orientation-dependent pulse distortion and the distance

Table 4.1: Final antenna dimensions (and fabrication tolerances).

Dimension	Value [mm]	Dimension	Value [mm]
W_{PIFA}	30.0 (±0.5)	L_{feed}	18.7 (±0.1)
$L_{PIFA,1}$	20.1 (±0.5)	L_{gap}	5.0 (±0.5)
$L_{PIFA,2}$	12.4 (±0.5)	W_{ext}	30.0 (±0.5)
H_{PIFA}	3.55 (±0.1)	t_{metal}	1.0

estimation biasing error are primarily influenced by the ground plane extension. Therefore, two subsequent multi-objective optimization procedures, as defined in [11], are performed. First, a set of Pareto optimal solutions is found that minimize the pulse distortion by maximizing the SFF, while preserving the required frequency-domain properties. To this end, the resonance frequencies of the PIFA elements and their coupling are optimized by adjusting $L_{PIFA,1}$, $L_{PIFA,2}$ and L_{gap}. Next, by sizing the ground plane extension (W_{ext}), a second set of Pareto optimal solutions is obtained that maximize the orientation-specific SFF while minimizing the DEE within the antenna′s HPBW in the azimuth plane.

4.3.3 Fabrication and Final Prototype

Finally, the antenna performance is demonstrated by manufacturing a prototype out of brass sheets, with a thickness of 1.0 mm, using a combination of CNC milling and shearing, exhibiting fabrication tolerances of ±0.1 mm and ±0.5 mm, respectively. Nevertheless, other non-ferrous metals, such as copper or aluminum, could also be applied for the antenna production. Furthermore, diverse metalworking techniques, such as, laser cutting or metal bending, can be adopted without deteriorating the antenna performance. To assemble the different antenna parts without corrupting the antenna performance, standard M3 nylon screws and bolts are used.

The final antenna dimensions are optimized using the CST Microwave Solver. They are summarized in Table 4.1, detailing the dimensions after optimization and the expected tolerances. An exploded view of the final antenna prototype is depicted in Fig. 4.1(d).

4.4 Simulation and Measurement Results

4.4.1 Frequency-domain results

The frequency-domain performance of the antenna is measured in an anechoic chamber, using a Keysight N5242a PNA-X network analyzer and a NSI-MI spherical near-field scanner. Fig. 4.2, depicting the reflection coefficient $|S_{11}|$ with respect to $Z_0 = 50\Omega$, shows a good agreement between the measurement results of two prototypes and simulations. An -10 dB impedance bandwidth of 1.5 GHz is obtained around 4 GHz, yielding a fractional bandwidth of 37.5%. Furthermore,

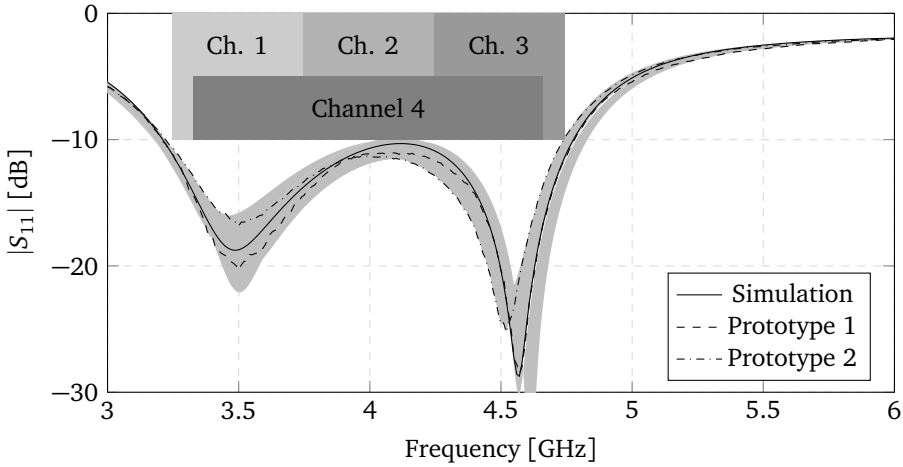

Figure 4.2: Simulated and measured reflection coefficient $|S_{11}|$ w.r.t. 50 Ω of the final antenna (black lines) and parameter sweeps (grey area) to assess fabrication tolerances.

results of an extensive parameter sweep have been added to Fig. 4.2, indicated by the gray area, to demonstrate robustness against fabrication tolerances and material variations. Fig. 4.3 shows a good agreement between the simulated and measured gain pattern in the azimuth (xz-plane) and elevation plane (yz-plane) at 3.5 GHz, 4.0 GHz and 4.5 GHz, reporting a boresight gain of 4.73 dBi, 4.66 dBi and 6.04 dBi, respectively. An HPBW larger than 120° in the azimuth plane, indicated by the gray boxes, can be observed at each frequency, while maintaining an FTBR higher than 10 dB and a mean cross-polarization discrimination within that HPBW of 44.8 dB, 38.6 dB and 39.0 dB at 3.5 GHz, 4.0 GHz and 4.5 GHz, respectively. Furthermore, note that special care is required when integrating this antenna into a three-element sectorized antenna array to preserve its radiation properties. Finally, a total antenna efficiency of 98.8%, 85.1% and 99.1% is measured at 3.5 GHz, 4.0 GHz and 4.5 GHz, respectively.

4.4.2 Time-domain results

To characterize the time-domain system performance, the measurement setup depicted in Fig. 4.4 is used. The antenna system consists of a fixed antenna, fully characterized in [11], and the current antenna which acts as the rotating AUT.

To compensate for any undesired pulse distortion introduced by the measurement setup, all measurements are calibrated by characterizing the time-domain performance of the measurement setup (by implementing a wired through-connection without antennas) and pre-distorting the generated input pulse accordingly. The resulting time-domain results are presented in Fig. 4.5. A good agreement between the simulated and measured SFF can be observed, showing an SFF over

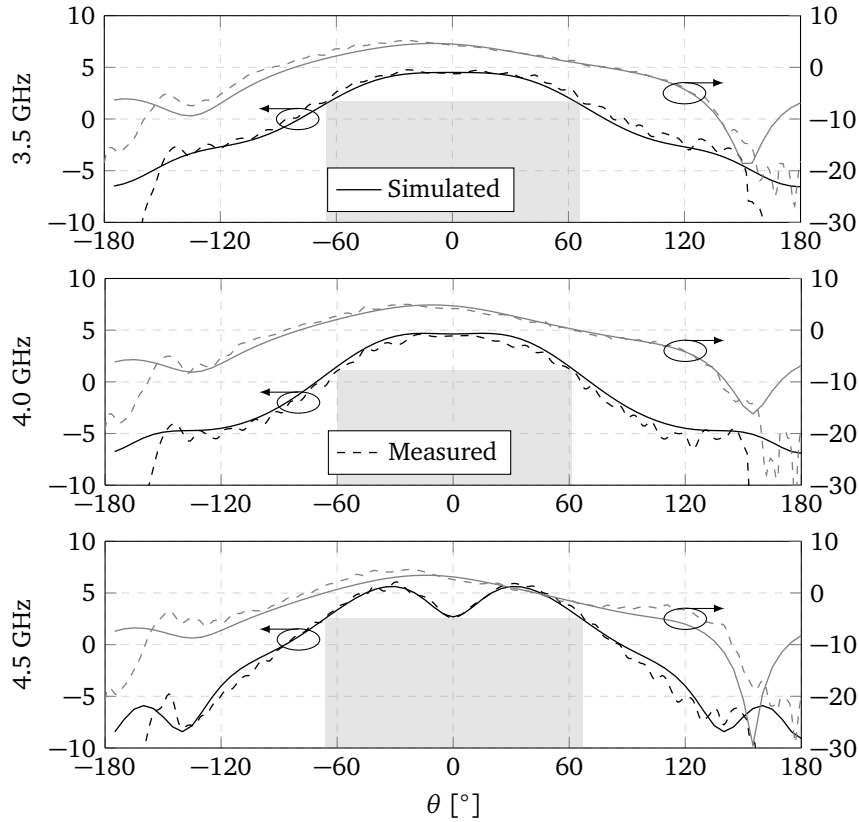

Figure 4.3: Simulated (solid) and measured (dashed) antenna gain [dBi] in the azimuth plane (black) and elevation plane (gray) at 3.5, 4.0 and 4.5 GHz.

90% within the complete HPBW of the azimuth plane. Furthermore, both simulations and measurements of the ranging bias agree very well, proving a ranging bias below 4 mm within the complete HPBW of the azimuth plane. Moreover, an SFF above 95% and ranging bias below 8 mm are measured in the elevation plane for $\theta = [-90°; 90°]$.

4.5 Conclusion

In this letter, a planar sectoral antenna is presented, optimized for highly precise IR-UWB indoor localization with minimal DEE. The antenna exhibits a reflection coefficient below -10 dB for the frequency range [3.2448 – 4.7424] GHz. A HPBW above 120° is reported for all frequencies within the frequency band of operation. Finally, an SFF higher than 90% and a ranging bias lower than 4 mm are measured within the HPBW of the azimuth plane. As a result, the proposed antenna

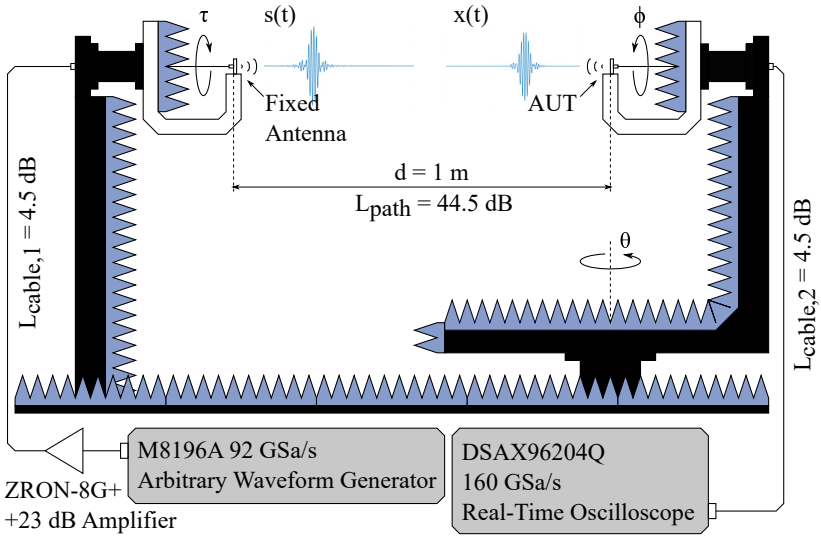

Figure 4.4: Measurement setup for the time-domain measurements in free-space conditions.

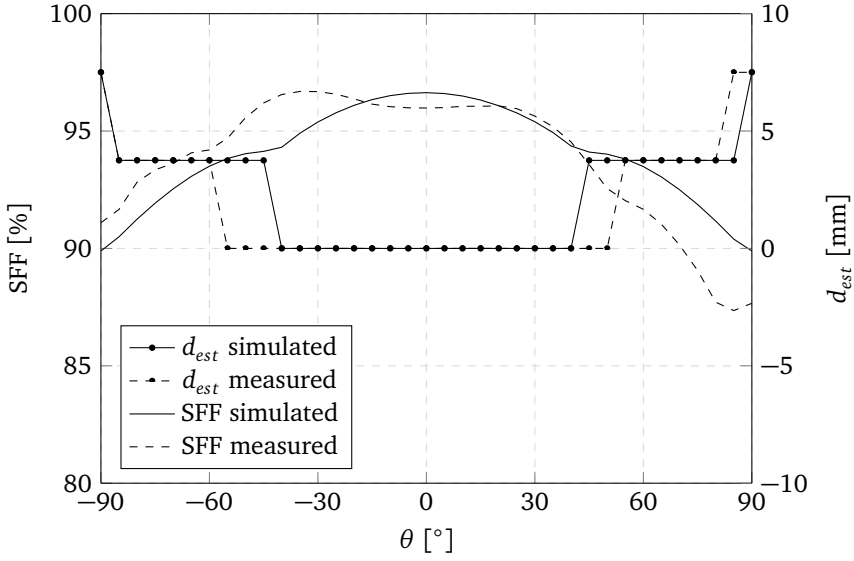

Figure 4.5: Simulated and measured system fidelity factor [%] (left) and orientation-specific ranging bias [mm] (right) in the azimuth plane.

is especially suited as an anchor antenna for highly accurate IR-UWB localization systems.

References

[1] R. Zekavat and R. M. Buehrer, "Wireless Localization Using UltraWideband Signals", in *Handbook of Position Location: Theory, Practice, and Advances*. 2019, pp. 269–301.

[2] F. Zafari, A. Gkelias, and K. K. Leung, "A Survey of Indoor Localization Systems and Technologies", *IEEE Communications Surveys Tutorials*, vol. 21, no. 3, pp. 2568–2599, 2019.

[3] A. Yassin, Y. Nasser, M. Awad, A. Al-Dubai, R. Liu, C. Yuen, R. Raulefs, and E. Aboutanios, "Recent Advances in Indoor Localization: A Survey on Theoretical Approaches and Applications", *IEEE Communications Surveys Tutorials*, vol. 19, no. 2, pp. 1327–1346, 2017.

[4] A. R. Jiménez Ruiz and F. Seco Granja, "Comparing Ubisense, BeSpoon, and DecaWave UWB Location Systems: Indoor Performance Analysis", *IEEE Transactions on Instrumentation and Measurement*, vol. 66, no. 8, pp. 2106–2117, 2017.

[5] R. Bharadwaj, S. Swaisaenyakorn, C. G. Parini, J. C. Batchelor, and A. Alomainy, "Impulse Radio Ultra-Wideband Communications for Localization and Tracking of Human Body and Limbs Movement for Healthcare Applications", *IEEE Transactions on Antennas and Propagation*, vol. 65, no. 12, pp. 7298–7309, 2017.

[6] D. Shi, H. Mi, E. G. Collins, and J. Wu, "An Indoor Low-Cost and High-Accuracy Localization Approach for AGVs", *IEEE Access*, vol. 8, pp. 50 085–50 090, 2020.

[7] Y. Xu *et al.*, "Robust and Accurate UWB-based Indoor Robot Localisation using Integrated EKF/EFIR Filtering", *IET Radar, Sonar Navigation*, vol. 12, no. 7, pp. 750–756, 2018.

[8] A. D. Preter, G. Goysens, J. Anthonis, J. Swevers, and G. Pipeleers, "Range Bias Modeling and Autocalibration of an UWB Positioning System", in *2019 International Conference on Indoor Positioning and Indoor Navigation (IPIN)*, 2019, pp. 1–8.

[9] B. Silva and G. P. Hancke, "IR-UWB-Based Non-Line-of-Sight Identification in Harsh Environments: Principles and Challenges", *IEEE Trans. on Industrial Informatics*, vol. 12, no. 3, pp. 1188–1195, 2016.

[10] G. Quintero, J. Zurcher, and A. K. Skrivervik, "System Fidelity Factor: A New Method for Comparing UWB Antennas", *IEEE Transactions on Antennas and Propagation*, vol. 59, no. 7, pp. 2502–2512, 2011.

[11] Q. Van den Brande, S. Lemey, J. Vanfleteren, and H. Rogier, "Highly Efficient Impulse-Radio Ultra-Wideband Cavity-Backed Slot Antenna in Stacked Air-Filled Substrate Integrated Waveguide Technology", *IEEE Transactions on Antennas and Propagation*, vol. 66, no. 5, pp. 2199–2209, 2018.

[12] L. Zwirello, T. Schipper, M. Harter, and T. Zwick, "UWB Localization System for Indoor Applications: Concept, Realization and Analysis", *Journal of Electrical and Computer Engineering*, 2012.

[13] W. Sörgel and W. Wiesbeck, "Influence of the Antennas on the Ultra-Wideband Transmission", *EURASIP Journal on Advances in Signal Processing*, vol. 2005, no. 3, Mar. 2005.

[14] A. Ledergerber and R. Dandrea, "Calibrating Away Inaccuracies in Ultra Wideband Range Measurements: A Maximum Likelihood Approach", *IEEE Access*, vol. 6, pp. 78 719–78 730, 2018.

[15] R. Ye, S. Redfield, and H. Liu, "High-Precision Indoor UWB Localization: Technical Challenges and Method", in *2010 IEEE International Conference on Ultra-Wideband*, vol. 2, 2010, pp. 1–4.

[16] M. Pelka, M. Cimdins, and H. Hellbrück, "Impact of the Antenna Orientation for Distance Estimation", *Proceedings of the 3rd KuVS/GI Expert Talk on Localization*, M. Cimdins and H. Hellbrück, Eds., pp. 17–19, 2018.

[17] A. Ledergerber and R. D'Andrea, "Ultra-Wideband Range Measurement Model with Gaussian Processes", in *2017 IEEE Conference on Control Technology and Applications (CCTA)*, 2017, pp. 1929–1934.

[18] V. Barral *et al.*, "Assessment of UWB Ranging Bias in Multipath Environments", in *Proceedings of the International Conference on Indoor Positioning and Indoor Navigation (IPIN), Alcala de Henares, Spain*, 2016, pp. 4–7.

[19] M. Pelka, M. Cimdins, and H. Hellbrück, "Impact of the Antenna Orientation for Distance Estimation", en, *Proceedings of the 3rd KuVS/GI Expert Talk on Localization*, 2018.

[20] "IEEE Standard for Local and Metropolitan Area Networks–Part 15.4: Low-Rate Wireless Personal Area Networks (LR-WPANs)", *IEEE Std 802.15.4-2011*, pp. 1–314, 2011.

[21] C. Liu, S. Xiao, H. Tu, and Z. Ding, "Wide-Angle Scanning Low Profile Phased Array Antenna Based on a Novel Magnetic Dipole", *IEEE Transactions on Antennas and Propagation*, vol. 65, no. 3, pp. 1151–1162, 2017.

[22] B. Mohamadzade, R. B. V. B. Simorangkir, R. M. Hashmi, and A. Lalbakhsh, "A Conformal Ultrawideband Antenna With Monopole-Like Radiation Patterns", *IEEE Transactions on Antennas and Propagation*, vol. 68, no. 8, pp. 6383–6388, 2020.

[23] S. R. Emadian, J. Ahmadi-Shokouh, C. Ghobadi, and J. Nourinia, "Study on Frequency and Impulse Response of novel Triple Band Notched UWB Antenna in Indoor Environments", *AEU - International Journal of Electronics and Communications*, vol. 96, pp. 93–106, 2018.

[24] S. Ullah, C. Ruan, M. S. Sadiq, T. U. Haq, and W. He, "High Efficient and Ultra Wide Band Monopole Antenna for Microwave Imaging and Communication Applications", *Sensors*, vol. 20, no. 1, 2020.

[25] A. Edalati, W. Shao, T. McCollough, and W. McCollough, "A Novel Cavity Backed Monopole Antenna with UWB Unidirectional Radiation", *Progress In Electromagnetics Research*, vol. 72, pp. 1–13, 2017.

[26] M. Li and K. Luk, "A Differential-Fed UWB Antenna Element With Unidirectional Radiation", *IEEE Transactions on Antennas and Propagation*, vol. 64, no. 8, pp. 3651–3656, 2016.

[27] Y. Li, X. Yang, Z. Li, L. Wang, and H. Yang, "A Unidirectional Cylindrical Conformal Monopole Antenna Designed for Impulse Radar System", *IEEE Antennas and Wireless Propagation Letters*, vol. 10, pp. 1397–1400, 2011.

[28] D. Van Baelen, Q. Van den Brande, S. Lemey, J. Verhaevert, and H. Rogier, "Foldable All-Textile Cavity-Backed Slot Antennas for Personal UWB Localization", *Radio Science*, vol. 55, no. 3, e2019RS006990, 2020, e2019RS006990 10.1029/2019RS006990.

[29] T. Cuyckens and H. Rogier, "Framework for the Simulation of Wireless Power Transmission over Ultra Wide Band Links in Multipath Propagation Environments in the Vicinity of the Human Body", *International Journal of Numerical Modelling: Electronic Networks, Devices and Fields*, vol. 29, no. 3, pp. 364–379, 2016.

[30] Yanchao Zhang, Wei Liu, Yuguang Fang, and Dapeng Wu, "Secure Localization and Authentication in Ultra-Wideband Sensor Networks", *IEEE Journal on Selected Areas in Communications*, vol. 24, no. 4, pp. 829–835, 2006.

[31] S. Krishnan, P. Sharma, Z. Guoping, and O. H. Woon, "A UWB based Localization System for Indoor Robot Navigation", in *2007 IEEE International Conference on Ultra-Wideband*, 2007, pp. 77–82.

[32] S. J. Ingram, D. Harmer, and M. Quinlan, "UltraWideBand Indoor Positioning Systems and their use in Emergencies", in *PLANS 2004. Position Location and Navigation Symposium (IEEE Cat. No.04CH37556)*, 2004, pp. 706–715.

[33] V. Barral, P. Suárez-Casal, C. Escudero, and J. García-Naya, "Multi-Sensor Accurate Forklift Location and Tracking Simulation in Industrial Indoor Environments", *Electronics*, vol. 8, p. 1152, Oct. 2019.

[34] X. Chen, L. Yang, J. Zhao, and G. Fu, "High-Efficiency Compact Circularly Polarized Microstrip Antenna With Wide Beamwidth for Airborne Communication", *IEEE Antennas and Wireless Propagation Letters*, vol. 15, pp. 1518–1521, 2016.

[35] M. K. Ray, K. Mandal, and N. Nasimuddin, "Low-Profile Circularly Polarized Patch Antenna With Wide 3 dB Beamwidth", *IEEE Antennas and Wireless Propagation Letters*, vol. 18, no. 12, pp. 2473–2477, 2019.

[36] M. Wang, X. Zhu, Y. Guo, and W. Wu, "Compact Circularly Polarized Patch Antenna With Wide Axial-Ratio Beamwidth", *IEEE Antennas and Wireless Propagation Letters*, vol. 17, no. 4, pp. 714–718, 2018.

[37] K. Ng, C. H. Chan, and K. Luk, "Low-Cost Vertical Patch Antenna With Wide Axial-Ratio Beamwidth for Handheld Satellite Communications Terminals", *IEEE Transactions on Antennas and Propagation*, vol. 63, no. 4, pp. 1417–1424, 2015.

[38] T. P. Wong and K. M. Luk, "A Wideband L-Probe Patch Antenna Array with Wide Beamwidth", *IEEE Transactions on Antennas and Propagation*, vol. 51, no. 10, pp. 3012–3014, 2003.

[39] V. Antonchik, "Theory and Experiment of Planar Inverted F-Antennas for Wireless Communications Applications", Ph.D. dissertation, Simon Fraser University, 2007.

[40] Q. Van den Brande, S. Lemey, H. Rogier, and J. Vanfleteren, "Coupled Half-Mode Cavity-Backed Slot Antenna for IR-UWB in Air-Filled SIW Technology", in *2018 IEEE International Symposium on Antennas and Propagation USNC/URSI National Radio Science Meeting*, 2018, pp. 1269–1270.

Part II

Highly Efficient On-Chip Antenna Technology for 5G and beyond 5G Wireless Systems

5

5G: A Hybrid Integration Strategy for Compact, Broadband, and Highly Efficient Millimeter-Wave On-Chip Antennas

Abstract

A novel hybrid integration strategy for compact, broadband and highly efficient Milimeter-Wave (mmWave) on-chip antennas is demonstrated by realizing a hybrid on-chip antenna, operating in the [27.5-29.5] GHz band. A cavity-backed stacked patch antenna is implemented on a 600 µm-thick silicon substrate by using Air-Filled Substrate-Integrated-Waveguide (AFSIW) technology. A hybrid on-chip approach is adopted in which the antenna feed and an air-filled cavity are integrated on chip and the stacked patch configuration is implemented on a high frequency Printed Circuit Board (PCB) laminate that supports the chip. A prototype of the hybrid on-chip antenna is validated, demonstrating an impedance bandwidth of 3.7 GHz. In free-space conditions, a boresight gain of 7.3 dBi and a Front-to-Back Ratio (FTBR) of 20.3 dB at 28.5 GHz are achieved. Moreover, the antenna is fabricated using standard silicon fabrication techniques and features a total antenna efficiency above 90 % in the targeted frequency band of operation. The high performance, in combination with the compact antenna footprint of $0.49\,\lambda_{min} \times 0.49\,\lambda_{min}$, makes it an ideal building block to construct broadband antenna arrays with a broad steering range.

5.1 Introduction

As we embark on the road to the fifth generation of network technology (5G), countless challenges and opportunities emerge. To address the prime objectives of 5G, radical improvements are needed in the cellular network architecture [1]. Given that the cellular bands below 6 GHz cannot support the exponentially increasing demands, a key enabler to realize 5G is mmWave communication. As such, 5G is likely to utilize much higher frequencies, up to mmWave and beyond [2]. On the one hand, one of the major challenges in implementing mmWave communication is overcoming the unfavorable propagation characteristics [3]. To conquer this hurdle, multi-antenna systems with adaptive beamforming will be indispensable [4], [5]. On the other hand, the exploitation of mmWave frequencies gives rise to smaller antenna footprints. This facilitates highly integrated radio units containing both the RF front-end and the antenna, thereby improving reliability and mitigating large interconnect losses [6]–[13]. In literature, two main strategies can be identified to realize these highly integrated RF solutions: Antenna-on-Chip (AoC) and Antenna-in-Package (AiP). Although both strategies are very promising, several critical issues remain. On the one hand, AoC solutions typically suffer from unfavorable electromagnetic material properties of bulk silicon substrates, resulting in poor antenna performance and substantial surface wave excitation [9]. On the other hand, AiP integration strategies face increased interconnect losses. These become more pronounced as the frequency of operation increases [9] and may be reduced by using flip-chip technology [11]. However, the inductive nature of the interconnects may lead to narrow-band performance [13]. Furthermore, in both integration strategies, utmost care should be taken to prevent Electromagnetic Interference (EMI) issues, due to inadequate shielding of the RF front-end [9].

In this letter, a novel hybrid integration strategy for compact, broadband and highly efficient mmWave on-chip antennas is demonstrated by realizing a highly-efficient hybrid on-chip antenna, operating in the [27.5-29.5] GHz band. A cavity-backed stacked patch antenna topology is selected and implemented in AFSIW technology. In order to achieve unprecedented overall AoC/AiP performance, a hybrid on-chip approach is adopted by implementing the antenna feed and a metallized air-filled cavity on chip and the stacked patch configuration on a Rogers $RO4350B^{®}$ laminate supporting the chip. The fabricated hybrid on-chip antenna exhibits a measured -10 dB-bandwidth of 3.7 GHz, a maximal gain of 7.3 dBi at 28.5 GHz and a total antenna efficiency larger than 90 % in the complete [27.5-29.5] GHz frequency band. Moreover, by leveraging a stacked-patch configuration, an antenna footprint of only 5.0 mm × 5.0 mm is obtained. Furthermore, a high isolation between the antenna and both the RF front-end and neighboring antennas is achieved by metallizing the air-filled cavity, thereby reducing EMI issues [9] and detrimental mutual coupling effects in antenna arrays [13], [14].

Many attempts to increase antenna efficiency have been described in literature, both for AoC [15]–[25] and AiP strategies [11], [13], [19]. Considering AoC strate-

gies, micromachined patch antennas have been a popular antenna topology [8], [16], [17], [20]–[22], [26], achieving antenna efficiencies up to 95 %. However, these techniques usually result in an enlarged antenna footprint. Furthermore, high levels of mutual coupling [17] and/or susceptibility to EMI issues [15] were present due to a lack of metallization of the micromachined cavities. Other micromachined topologies have been reported as well [15], [18], [19], achieving equivalent radiation performance. Yet, the aforementioned issues remain. Another common radiation enhancement technique is superstrate focusing [23]–[25], enabling easy integration with 0.13 µm SiGe or Complementary Metal Oxide Semiconductor (CMOS) Radio Frequency (RF) front-ends. However, the highest reported antenna efficiency is limited to 50 %. In conclusion, the AoC strategy typically leads to a constant trade-off between antenna efficiency, bandwidth and antenna footprint. In this respect, the AiP strategy allows achieving high antenna efficiencies within a small antenna footprint [11], [13], [19]. However, interconnects still remain an obstacle for AiP strategies [9] and, as such, hybrid integration strategies have been proposed to combine the best of both integration strategies, yielding high performance integrated antennas [10], [12]. Compared to [10], [12], our hybrid integration strategy reconciles the conflicting demands of high radiation efficiency, large bandwidth, small footprint and low interconnect losses by implementing the antenna feed and a metallized air-filled cavity on chip and exploiting the RF PCB laminate that supports the chip for the implementation of a stacked patch configuration. Furthermore, the use of AFSIW technology strongly reduces EMI issues, commonly encountered in AoC and AiP designs. The proposed hybrid integration strategy is validated by realizing a novel on-chip antenna. Its measured performance is compared with the current state-of-the-art in Table 5.1, proving its excellent performance in terms of bandwidth, antenna efficiency and antenna footprint.

The remainder of this paper is organized as follows. In Section 5.2, the hybrid on-chip antenna topology is proposed and the design evolution is discussed. Section 5.3 elaborates on the fabrication process and the relevant manufacturing tolerances. Simulation and measurement results are discussed in Section 5.4.

5.2 Compact and Highly-Efficient Hybrid On-Chip Stacked Patch Antenna

A linearly polarized, highly integrated antenna on silicon is designed for operation in the [27.5-29.5] GHz band, targeting an antenna footprint smaller than $5.450mm \times 5.450mm$ ($0.54\,\lambda_{min} \times 0.54\,\lambda_{min}$, with λ_{min} the free-space wavelength at 29.5 GHz) for grating lobe-free beamsteering up to $\theta = \pm 60°$. Moreover, an antenna efficiency over 90 % is imposed in the complete bandwidth. Finally, a fabrication procedure that guarantees compatibility with CMOS and Microelectromechanical Systems (MEMS) processes and, thus, allows mass production and scalability to even higher frequencies is strived for to remain competitive with current

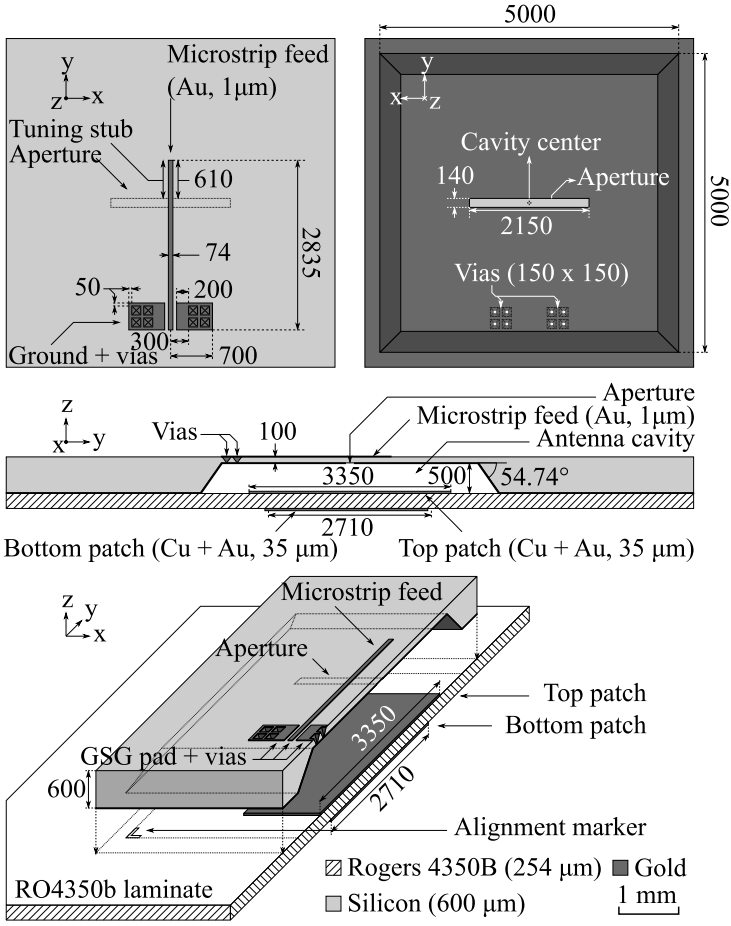

Figure 5.1: Structure of the hybrid on-chip antenna (dimensions in µm). Top left: top view; top right: bottom view; middle: cross-sectional view; bottom: 3D cross-sectional view. The rectangular top and bottom patch have dimensions 3350 µm × 1800 µm and 2710 µm × 3080 µm, respectively.

state-of-the-art solutions. To fulfill these stringent design requirements, a cavity-backed stacked patch antenna topology is adopted, as shown in Fig. 5.1. The backing cavity guarantees both a high antenna-to-integration platform isolation and reduces mutual coupling in arrays [14], while the stacked-patch configuration enables to satisfy the radiation and bandwidth requirements. To achieve the imposed total antenna efficiency, the antenna is implemented in AFSIW technology [27]–[29]. By removing the silicon substrate underneath the stacked patches and plating the newly exposed silicon surface, an AFSIW cavity is created. As a result, the electromagnetic fields of the stacked patch antenna reside in an air substrate for the most part and, hence, a low-loss antenna performance is achieved over a large bandwidth and surface wave excitation is strongly suppressed. Furthermore, by exploiting mode-bifurcation [29] in the stacked patch configuration, the antenna footprint of 5.0 mm × 5.0 mm remains below $0.54\,\lambda_{min} \times 0.54\,\lambda_{min}$, despite the use of AFSIW technology. As can be seen in Fig. 5.1, a hybrid on-chip antenna strategy is adopted. The antenna is constructed partially on chip and partially on a high-frequency PCB laminate, where the parts that need the highest accuracy are developed in silicon, making use of micro- and nanoscale fabrication technologies. The antenna cavity and feed structure are created in and on a 610 µm thick silicon wafer ($\epsilon_r = 11.9, \tan\delta = 0.0013$), respectively, whereas the patches are implemented on a 254 µm thick Rogers *RO*4350*B*® laminate ($\epsilon_r = 3.66, \tan\delta = 0.0031$), subsequently bonded to the silicon wafer with a non-conductive glue. On the one hand, the antenna feed structure is fabricated on-chip, making it compatible with standard silicon fabrication processes and thus, the implementation of the RF front-end can be both fully electrical [6], [7] or an opto-electrical hybrid [30], [31]. On the other hand, suspending the stacked-patch configuration on a Rogers *RO*4350*B*® laminate allows a radiation performance equivalent to AiP antennas, without frequency dependent interconnect losses. As such, our hybrid on-chip antenna approach minimizes interconnect losses and alleviates the trade-off between bandwidth, efficiency and antenna footprint.

A 200 µm pitch Ground-Signal-Ground (GSG) pad is used to enable antenna characterization with a probe, via a microstrip feed that excites the antenna by means of aperture coupling. Tuning the antenna feed dimensions, being the rectangular aperture and the tuning stub (see Fig. 5.1), allows for an optimization of the FTBR while still maintaining sufficient bandwidth. Moreover, leveraging aperture coupling provides adequate shielding between the antenna and feeding network, significantly mitigates parasitic radiation and benefits radiation pattern purity. Remark that the metallic traces on silicon are composed of gold and have a thickness of 1 µm, whereas the patches on the Rogers *RO*4350*B*® laminate are gold-plated copper traces and have a thickness of 35 µm. Both patches and the aperture in the cavity are centered around the cavity center. Furthermore, as the antenna cavity and vias are created with a low-cost potassium hydroxide (*KOH*) wet etch process, they exhibit sloped edges with a fixed angle of 54.74 °, as discussed in more detail in Section 5.3. This is due to the (100) crystalline orientation of the silicon wafer. The proposed antenna is designed using the frequency domain solver of

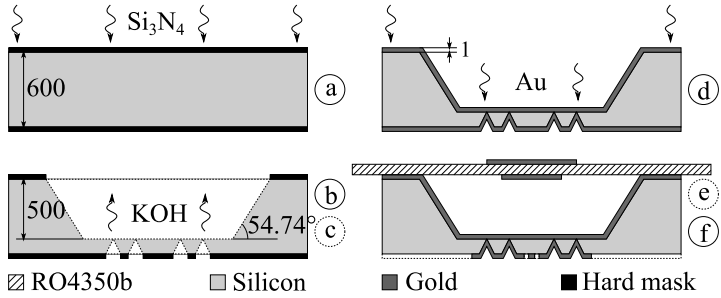

Figure 5.2: An overview of the fabrication process (dimensions in μm): (a) hard mask deposition, (b) hard mask patterning, (c) wet etch, (d) gold deposition, (e) gold patterning and (f) bonding.

CST Microwave Studio. Its final dimensions are shown in Fig. 5.1.

5.3 Fabrication Process

The antenna is fabricated in the clean room facility of Ghent University. It is fully compatible with standard silicon fabrication processes, making it low cost and suitable for mass production. A high-resistivity (100) silicon substrate is used with a thickness of 600 μm and a reported resistivity of 40 Ωcm. The substrate is undoped, double sided polished, and contains a thin silicon oxide (SiO_2) layer of 400 nm on both sides. Using a chemical vapor deposition process, a 600 nm-thick silicon nitride (Si_3N_4) layer is deposited on both sides of the silicon wafer (Fig. 5.2(a)) to realize a hard mask for the wet etch. Next, the silicon wafer is cleaved into samples of 20 mm × 20 mm. The remainder of the processing is divided into the following steps: etching, metallization and bonding.

First, the antenna cavity and vias, described in Section 5.2, are etched into the silicon samples. Thereto, a thin layer of TI prime [32] is spin coated onto the top side of the sample to promote adhesion of the photoresist in the next step. After the proper baking procedure, a 4 μm thick TI 35E [33] photoresist layer is spin coated on top of the TI prime layer and baked. Next, the SUSS MicroTec MA6/BA6 aligner is used to perform the photolithography step, where the image reversal technique [33] is adopted to pattern the photoresist. The Advanced Vacuum Vision 310 Reactive Ion Etching (RIE) is then used to transfer the pattern onto the hard mask with a plasma etching procedure, using a gas mixture of SF_6 and O_2. However, first, a thin TI 35E photoresist layer is coated on the backside of the sample to protect it during the plasma etching step. The cavity pattern is now transferred onto the hard mask of the silicon sample (Fig. 5.2(b)). Next, the same procedure is used to transfer the via patterns onto the hard mask on the sample backside. To ensure accurate positioning of the vias, backside alignment (with an accuracy of ±600 nm) is performed with the cavity corners as a reference. Finally, a wet etch procedure is performed using a 20 % KOH solution. The etching solution is heated to 80 °C,

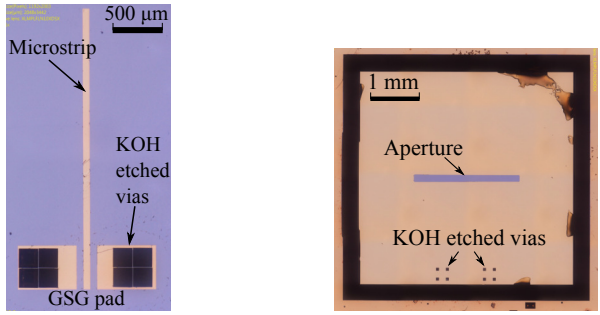

(a) (b)

Figure 5.3: (a) Feed structure with GSG pad and (b) etched cavity with aperture of the on-chip stacked patch antenna.

resulting in a silicon etch rate of about 1.7 µm/min. The samples are submerged in the solution for 295 min, until a cavity depth of 500 µm is reached (Fig. 5.2(c)). Due to the (100) crystalline orientation of the silicon wafer, the edges are etched at an angle of 54.74 ° and, as such, the etching process of the vias stops automatically after the tip of its pyramidal shape is reached (Fig. 5.2(c)). After completing the etching process, a small portion of the cavity is punctured by the vias on the other side of the silicon sample. Lastly, the remainder of the hard mask is removed using a hydrofluoric acid (HF) solution.

In the second step, gold (Au) is deposited and patterned on both sides of the chip. First, a 10 nm layer of titanium (Ti) is predeposited on the sample backside by means of sputtering to act as an adhesive layer between the Si and Au. Afterwards, sputtering is applied to deposit a 1 µm-thick layer of Au (Fig. 5.2(d)). Next, an 8.8 µm-thick layer of AZ9260 positive resist [34] is applied to pattern the metal on the backside of the silicon sample during the photolitography step. After developing the sample in a 1:2 AZ400K [35] water solution, the feed structure of the antenna is finished (Fig. 5.2(e)). Next, the same procedure is performed for the top side of the sample to create the metal cavity and the feeding aperture. Backside alignment is again performed to guarantee accurate alignment of the different antenna features. A fabricated on-chip antenna prototype is shown in Fig. 5.3.

In the final step, the metallized silicon sample is bonded to a $RO4350B^{®}$ laminate, supporting a stacked patch structure. To this end, a 9 µm-thick layer of Cyclotene 3022-57 [36] is spin coated on the substrate. By using the alignment markers on the superstrate (Fig. 5.1), the chip and PCB laminate are aligned by means of a Finetech Pick and Place bonder (with an accuracy of ±1 µm). After alignment, the chip and substrate are pressed together while being heated to 150 °C. After a heating period of 20 min, the antenna is finished (Fig. 5.2(f)). A fabricated on-chip antenna prototype is shown in Fig. 5.3. Note that, in future array configurations some excess silicon can be placed at the edges of the chip, to provide sufficient bonding surface between the superstrate and chip.

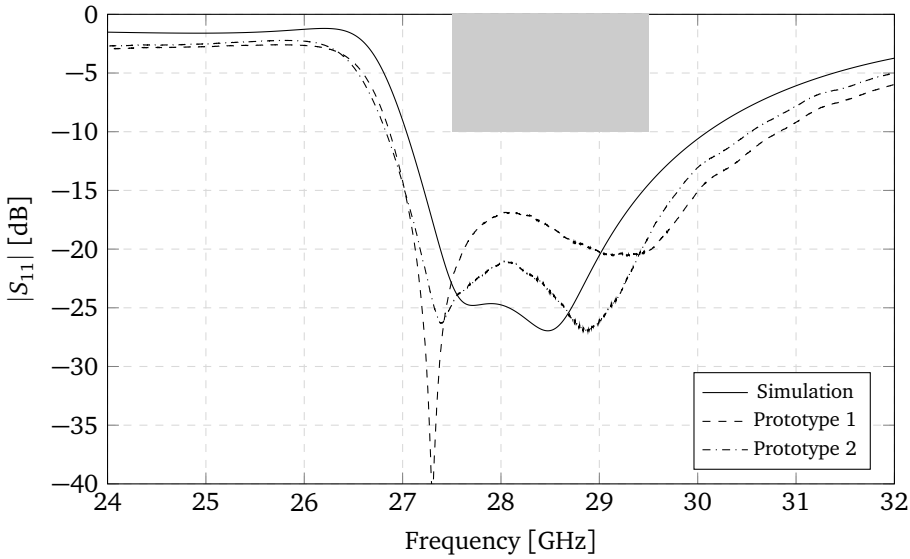

Figure 5.4: Simulated and measured magnitude of the reflection coefficient ($|S_{11}|$) w.r.t. 50 Ω.

5.4 Simulation and Measurement Results

The reflection coefficient and far-field performance of the antenna prototypes are measured in the mmWave Anechoic Chamber [37] at Eindhoven University of Technology (TUe). This fully automated system, with a 1 m diameter and a 0.5 m height, is equipped with a probing setup that allows both backside and front-side probing and is operational up to 90 GHz. In this letter, backside probing is performed using a GSG-200 Picoprobe and a Keysight N5247A PNA-X Microwave Network Analyzer for both the reflection coefficient and far-field measurements. A SOLT calibration is performed to measure the scattering parameters of two prototypes, making use of a CS-5 calibration substrate [38]. For measurement purposes, the patch-supporting *RO*4350*B*® laminate is sized 4 cm × 4 cm. The excess *RO*4350*B*® laminate is used to install the antenna inside the anechoic chamber on top of a Rohacell ($\epsilon_r = 1.05, \tan\delta = 0.0034$) antenna mount.

The simulated and measured $|S_{11}|$ w.r.t. 50 Ω of the hybrid on-chip antenna and the prototypes are shown in Fig. 5.4. Two resonance peaks are visible, because of the two stacked patches, resulting in a measured and simulated bandwidth of 3.7 GHz and 3.1 GHz, respectively. A good agreement between simulated and measured radiation patterns (co- and cross-polarization) in the yz- and xz-plane at 28.5 GHz can be seen in Fig. 5.5. A simulated boresight gain of 6.64 dBi, 7.27 dBi and 7.38 dBi is achieved at 27.5 GHz, 28.5 GHz and 29.5 GHz, respectively. The corresponding measured gain is 6.62 dBi, 7.08 dBi and 7.12 dBi, respectively. This

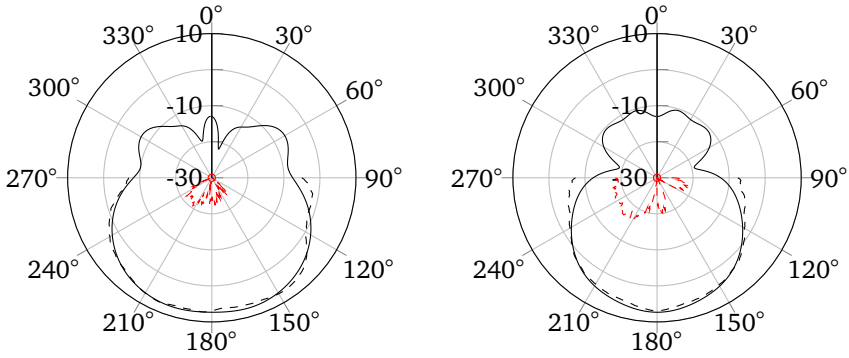

Figure 5.5: Simulated (solid) and measured (dashed), co-polarized (black) and cross-polarized (red) antenna gain at 28.5 GHz. (a) yz-plane (E-plane), (b) xz-plane (H-plane).

Table 5.1: Comparison of current work to the state-of-the-art.

	Technique	**f [GHz]**	**BW [%]**	η **[%]**	**A** [$\lambda \times \lambda$]
[17]	µMachining	135.0	8.90	80.0	0.81 × 0.81
[18]	µMachining	60.0	11.80	90.0	0.61 × 0.95
[19]	µMachining	143.0	13.90	76.0	0.95 × 0.95
[22]	µMachining	34.5	4.00	95.0	1.15 × 1.15
[24]	Superstrate	93.0	8.50	50.0	0.70 × 0.50
[19]	AiP	143.0	6.90	89.0	0.38 × 0.38
[11]	AiP	60.0	8.80	85.0	2.60 × 2.60
[13]	AiP	29.0	5.00	N.A.	0.23 × 0.23
[10]	Hybrid	60.0	12.60	73.0	0.33 × 0.16
[12]	Hybrid	68.0	5.70	96.7	0.16 × 0.28
This	**Hybrid**	**28.5**	**13.00**	**90.9**	**0.49 × 0.49**

results in a total antenna efficiency of 92.7 %, 90.9 % and 90.4 % at those frequencies. Furthermore, a FTBR of 20.3 dB is obtained at the center frequency and an axial radio over 20 dB within the 3 dB beamwidth of over 65°in both planes, is realized. Table 5.1 compares the proposed hybrid on-chip antenna with the state-of-the-art in terms of fractional bandwidth (BW), antenna efficiency (η) and antenna footprint (A). The antenna footprint is expressed in a fraction of the wavelength at the highest frequency of operation. It can be seen that the presented antenna enables excellent performance with respect to to the state-of-the-art, when considering the combination of bandwidth, efficiency and antenna footprint.

5.5 Conclusion

A novel hybrid integration strategy for mmWave antennas is demonstrated by realizing an on-chip AFSIW cavity-backed stacked patch antenna, featuring excellent performance in terms of radiation efficiency, broadside gain and bandwidth. Measurements report a total antenna efficiency over 90 %, a minimal boresight gain of 6.6 dBi and sufficient bandwidth to cover the [27.5-29.5] GHz band. Moreover, the compact antenna footprint (5.0 mm × 5.0 mm) in combination with the large beamwidth (>65°) and high antenna-to-integration platform isolation, makes the proposed antenna element an attractive building block for multi-antenna systems with beamsteering capabilities.

References

[1] A. Gupta and R. K. Jha, "A Survey of 5G Network: Architecture and Emerging Technologies", *IEEE Access*, vol. 3, 2015.

[2] Z. Pi, J. Choi, and R. Heath, "Millimeter-Wave Gigabit Broadband Evolution toward 5G: Fixed Access and Backhaul", *IEEE Communications Magazine*, vol. 54, no. 4, pp. 138–144, 2016.

[3] T. S. Rappaport, G. R. MacCartney, M. K. Samimi, and S. Sun, "Wideband Millimeter-Wave Propagation Measurements and Channel Models for Future Wireless Communication System Design", *IEEE Transactions on Communications*, vol. 63, no. 9, pp. 3029–3056, 2015.

[4] T. Cameron, "5G - The Microwave Perspective", *Analog Devices*, pp. 1–4, 2015.

[5] M. Y. Frankel, P. J. Matthews, and R. D. Esman, "Practical Optical Beamforming Networks", *Optical and Quantum Electronics*, vol. 30, pp. 1033–1050, 1998.

[6] W. Shin, B. Ku, O. Inac, Y. Ou, and G. M. Rebeiz, "A 108-114 GHz 4×4 Wafer-Scale Phased Array Transmitter with High-Efficiency On-Chip Antennas", *IEEE Journal of Solid-State Circuits*, vol. 48, no. 9, pp. 2041–2055, 2013.

[7] B. Ku, O. Inac, M. Chang, H. Yang, and G. M. Rebeiz, "A High-Linearity 76-85-GHz 16-Element 8-Transmit/8-Receive Phased-Array Chip with High Isolation and Flip-Chip Packaging", *IEEE Transactions on Microwave Theory and Techniques*, vol. 62, no. 10, pp. 2337–2356, 2014.

[8] Y. Liu, A. Agrawal, and A. Natarajan, "Millimeter-Wave IC-Antenna Cointegration for Integrated Transmitters and Receivers", *IEEE Antennas and Wireless Propagation Letters*, vol. 15, pp. 1848–1852, 2016.

[9] Y. P. Zhang and D. Liu, "Antenna-on-Chip and Antenna-in-Package Solutions to Highly Integrated Millimeter-Wave Devices for Wireless Communications", *IEEE Transactions on Antennas and Propagation*, vol. 57, no. 10, pp. 2830–2841, 2009.

[10] J. A. Zevallos Luna, L. Dussopt, and A. Siligaris, "Hybrid On-Chip/In-Package Integrated Antennas for Millimeter-Wave Short-Range Communications", *IEEE Transactions on Antennas and Propagation*, vol. 61, no. 11, pp. 5377–5384, 2013.

[11] Y. P. Zhang, M. Sun, D. Liu, and Y. Lu, "Dual Grid Array Antennas in a Thin-Profile Package for Flip-Chip Interconnection to Highly Integrated 60-GHz Radios", *IEEE Transactions on Antennas and Propagation*, vol. 59, no. 4, pp. 1191–1199, 2011.

[12] Y. Song, K. Kang, Y. Tian, Y. Wu, Z. Li, Y. Guo, Y. Ban, J. Liu, X. Tang, H. Liu, and J. Yang, "A Hybrid Integrated High-Gain Antenna with an On-Chip Radiator Backed by Off-Chip Ground for System-on-Chip Applications", *IEEE Transactions on Components, Packaging and Manufacturing Technology*, vol. 7, no. 1, pp. 114–122, 2017.

[13] H. Kim, B. Park, S. Song, T. Moon, S. Kim, J. Kim, J. Chang, and Y. Ho, "A 28-GHz CMOS Direct Conversion Transceiver with Packaged2 × 4Antenna Array for 5G Cellular System", *IEEE Journal of Solid-State Circuits*, vol. 53, no. 5, pp. 1245–1259, 2018.

[14] Y. Li and K. Luk, "60-GHz Substrate Integrated Waveguide Fed Cavity-Backed Aperture-Coupled Microstrip Patch Antenna Arrays", *IEEE Transactions on Antennas and Propagation*, vol. 63, no. 3, pp. 1075–1085, 2015.

[15] E. Ojefors, H. Kratz, K. Grenier, R. Plana, and A. Rydberg, "Micromachined Loop Antennas on Low Resistivity Silicon Substrates", *IEEE Transactions on Antennas and Propagation*, vol. 54, no. 12, pp. 3593–3601, 2006.

[16] G. P. Gauthier, J. Raskin, L. P. B. Katehi, and G. M. Rebeiz, "A 94-GHz Aperture-Coupled Micromachined Microstrip Antenna", *IEEE Transactions on Antennas and Propagation*, vol. 47, no. 12, pp. 1761–1766, 1999.

[17] H. Chu, Y. Guo, T. Lim, Y. M. Khoo, and X. Shi, "135-GHz Micromachined On-Chip Antenna and Antenna Array", *IEEE Transactions on Antennas and Propagation*, vol. 60, no. 10, pp. 4582–4588, 2012.

[18] P. Liu, L. Chang, Y. Li, Z. Zhang, S. Wang, and Z. Feng, "A Millimeter-Wave Micromachined Air-Filled Slot Antenna fed by Patch", *IEEE Transactions on Components, Packaging and Manufacturing Technology*, vol. 7, no. 10, pp. 1683–1690, 2017.

[19] W. T. Khan, A. Cagri Ulusoy, G. Dufour, M. Kaynak, B. Tillack, J. D. Cressler, and J. Papapolymerou, "A D-band Micromachined End-Fire Antenna in 130-nm SiGe BiCMOS Technology", *IEEE Transactions on Antennas and Propagation*, vol. 63, no. 6, pp. 2449–2459, 2015.

[20] Y. Koga, Y. Yoshida, A. Yamashita, T. Hamaguchi, K. Nishizawa, M. Taguchi, T. Nishino, H. Miyashita, and S. Makino, "Cavity-Backed MEMS Patch Antennas on Double-Layer Silicon Wafers", in *2006 IEEE Antennas and Propagation Society International Symposium*, 2006, pp. 3935–3938.

[21] I. Papapolymerou, R. Franklin Drayton, and L. P. B. Katehi, "Micromachined Patch Antennas", *IEEE Transactions on Antennas and Propagation*, vol. 46, no. 2, pp. 275–283, 1998.

[22] V. K. Singh, "Ka-band Micromachined Microstrip Patch Antenna", *IET Microwaves, Antennas Propagation*, vol. 4, no. 3, pp. 316–323, 2010.

[23] Y. Ou and G. M. Rebeiz, "On-Chip Slot-Ring and High-Gain Horn Antennas for Millimeter-Wave Wafer-Scale Silicon Systems", *IEEE Transactions on Microwave Theory and Techniques*, vol. 59, no. 8, pp. 1963–1972, 2011.

[24] ——, “Differential Microstrip and Slot-Ring Antennas for Millimeter-Wave Silicon Systems”, *IEEE Transactions on Antennas and Propagation*, vol. 60, no. 6, pp. 2611–2619, 2012.

[25] J. M. Edwards and G. M. Rebeiz, “High-Efficiency Elliptical Slot Antennas with Quartz Superstrates for Silicon RFICs”, *IEEE Transactions on Antennas and Propagation*, vol. 60, no. 11, pp. 5010–5020, 2012.

[26] M. Komulainen, J. Mahonen, T. Tick, M. Berg, H. Jantunen, M. Henry, C. Free, and E. Salonen, “Embedded Air Cavity Backed Microstrip Antenna on an LTCC Substrate”, *Journal of the European Ceramic Society*, vol. 27, no. 8, pp. 2881 –2885, 2007, Papers Presented at the Fourth International Conference on Microwave Materials and their Applications - MMA2006, Oulu, Finland.

[27] A. Ghiotto, F. Parment, T. P. Vuong, and K. Wu, “Millimeter-Wave Air-Filled SIW Antipodal Linearly Tapered Slot Antenna”, *IEEE Antennas and Wireless Propagation Letters*, vol. 16, pp. 768–771, 2017.

[28] F. Parment, A. Ghiotto, T. P. Vuong, J. M. Duchamp, and K. Wu, “Millimetre-Wave Air-Filled Substrate Integrated Waveguide Slot Array Antenna”, *Electronics Letters*, vol. 53, no. 11, pp. 704–706, 2017.

[29] Q. Van den Brande, S. Lemey, J. Vanfleteren, and H. Rogier, “Highly Efficient Impulse-Radio Ultra-Wideband Cavity-Backed Slot Antenna in Stacked Air-Filled Substrate Integrated Waveguide Technology”, *IEEE Transactions on Antennas and Propagation*, no. 99, pp. 1–1, 2018.

[30] A. O. Boryssenko, J. Liao, J. Zeng, S. Deng, V. M. Joyner, and Z. R. Huang, “Radio-Optical Dual-Mode Communication Modules Integrated with Planar Antennas”, *IEEE Transactions on Microwave Theory and Techniques*, vol. 58, no. 2, pp. 403–410, 2010.

[31] O. Caytan, L. Bogaert, H. Li, J. Van Kerrebrouck, S. Lemey, G. Torfs, J. Bauwelinck, P. Demeester, S. Agneessens, D. Vande Ginste, and H. Rogier, “Passive Opto-Antenna as Downlink Remote Antenna Unit for Radio Frequency over Fiber”, *Journal of Lightwave Technology*, vol. 36, no. 19, pp. 4445–4459, 2018.

[32] *TI PRIME adhesion promotor, Technical datasheet*, MicroChemicals GmbH, Aug. 2002.

[33] *TI 35E image reversal resist, Technical datasheet*, MicroChemicals GmbH, Aug. 2016.

[34] *AZ9200 Photoresist, High-Resolution Thick Resist, Technical datasheet*, MicroChemicals GmbH, 1997.

[35] *AZ400K, Technical datasheet*, MicroChemicals GmbH.

[36] *CYCLOTENE 3000 Series Advanced Electronic Resins, Technical datasheet*, DOW, Feb. 2005.

[37] A. C. F. Reniers, Q. Liu, M. H. A. J. Herben, and A. B. Smolders, "Review of the Accuracy and Precision of mm-Wave Antenna Simulations and Measurements", in *2016 10th European Conference on Antennas and Propagation (EuCAP)*, 2016, pp. 1–5.

[38] *Calibration Substrates, Technical datasheet*, Picoprobe GGB Industries.

6

Beyond 5G: Polymer-Enabled AFSIW Technology for Highly-Efficient, Broadband On-Chip THz Antenna Systems

Abstract

A novel polymer-enabled Air-Filled Substrate-Integrated-Waveguide (AFSIW) technology is presented for cost-effective, highly-efficient, broadband on-chip THz multi-antenna systems. To demonstrate its potential, a cavity-backed slot antenna with exponentially tapered feed and modified slot was designed in both a stand-alone and 1x4 linear array configuration, optimized for operation in the $[252.72-321.84]$ GHz frequency band of the IEEE 802.15.3d-2017 standard. Impedance matching below -10 dB is obtained for the unit antenna element in the $[248.0-355.0]$ GHz frequency band, exhibiting a radiation efficiency over 88% in the complete frequency band of interest within an antenna footprint of 500 $\mu m \times 500$ μm. A maximum gain of 5.32 dBi, 5.81 dBi and 5.81 dBi is obtained at 252.72 GHz, 287.28 GHz and 321.84 GHz, respectively. Grating-lobe free beam-steering is demonstrated in a 1x4 linear array configuration, with an inter-element spacing of 560 μm, with a gain of 11.75 dBi, 12.02 dBi and 11.54 dBi at 252.72 GHz, 287.28 GHz and 321.84 GHz, respectively. Furthermore, mutual coupling levels below -15 dB and an Front-to-Back Ratio (FTBR) above 16.8 dB is obtained in the complete targeted frequency.

6.1 Introduction

The wide-spread commercial adoption of 5G mobile networks is a response of telecommunication operators to the ever increasing demand for faster and more reliable communication services for an increasing amount of mobile devices. This trend is confirmed by the observation that wireless data rates have doubled every 18 months [1]. However, future technologies such as Augmented/Virtual Reality (AR/VR), wireless datacenters, chip-to-chip communication, and next-generation Wireless Personal Area Network (WPAN) or Wireless Local Area Network (WLAN) indoor cellular networks require low-latency, reliable and ultrawide-bandwidth communication channels, supporting data rates up to 100 Gbps [1]–[3]. Although advanced modulation schemes and improved hardware could facilitate higher data rates in the Milimeter-Wave (mmWave) frequency bands, there is an inherent limitation on the achievable data rate due to the limited available bandwidth. As a result, researchers are investigating possibilities in the unlicensed Terahertz (THz) frequency band, defined in the IEEE 802.15.3d-2017 standard [4], providing a bandwidth of 69 GHz and supporting data rates of 100 Gbps and higher at distances up to a few hundred meters [5].

At THz frequencies, the signal is not only subjected to significant and frequency dependent atmospheric attenuation [2], [3], but it also suffers from considerable losses due to poor microwave component efficiency, interconnects, packaging and assembly [1], [6], [7]. Integrating the THz transceiver, the beam forming networks and the on-chip antenna array into a compact and highly integrated System-on-Chip (SoC), greatly reduces the aforementioned losses and, moreover, facilitates further optimization by co-designing the antenna with the transceiver. However, the low radiation efficiency and narrowband behavior of on-chip antennas, still impose significant limitations on the viability of on-chip antennas in THz SoC applications [7].

In this chapter, a polymer-enabled AFSIW technology for highly-efficient, broadband on-chip THz antenna systems is presented, as a key enabler towards a low-cost and highly-integrated SoC framework for THz communication. By suspending a thin, low-loss polymer superstrate on top of an AFSIW cavity that is micromachined into a standard, low-cost silicon substrate, a frequency-independent antenna efficiency over 90% can be obtained. Furthermore, by implementing a coupled cavity-backed slot antenna with modified slot in the proposed layer stack-up, mode bifurcation is leveraged to obtain an ultra-wide impedance bandwidth within a compact footprint. As a result, a unit antenna element is realized that meets the aforementioned requirements for the on-chip antenna array in a low-cost, highly efficient and highly integrated SoC framework for THz communication. Finally, the array performance is demonstrated by means of a 1x4 linear antenna array, implemented using the realized unit antenna element, and shows grating-lobe free beam-steering capabilities up to 30°.

Several on-chip antenna topologies have been explored to resolve the low effi-

ciency and narrowband issues, both in mmWave and THz frequency bands [1], [6], [8]. Lens-loaded antennas have shown great potential enhancing both gain and directivity, whilst reducing side lobes and cross polarization levels of on-chip antennas [8]. However, besides a large footprint and more complex fabrication methods, some lenses can also distort the radiation pattern due to temperature fluctuations [9]. Dielectric-loaded antennas also show great promise to enhance radiation efficiency of THz on-chip antennas, as demonstrated by the antenna in [7] reporting an antenna efficiency of 80% and a gain of 10 dBi at 340 GHz. However, the inherent narrowband behavior and added fabrication complexity of dielectric resonators, limit their use in THz communication systems. THz antennas developed in Complementary Metal Oxide Semiconductor (CMOS) technology have been investigated as well, because of their low-cost and ubiquitous fabrication techniques [10], [11]. Unfortunately, the performance of the antenna reported in [10] was lacking, with a bandwidth of only 32.1 GHz at 267.6 GHz, a radiation efficiency of 23% and a maximum gain of -0.5 dBi. In [11], a transceiver SoC was realized in 130 nm SiGe BiCMOS technology, reporting a maximum radiation efficiency of 54% and maximum gain of 3 dBi. Finally, micro-machining techniques have been used to realize SIW on-chip antennas by filling metalized cavities, micro-machined into a silicon substrate, thereby enhancing the antenna radiation efficiency and impedance bandwidth [12], [13]. Liu et. al. realized a patch antenna and 1x4 linear array on top of a Benzocyclobutene (BCB)-filled metalized cavity, reporting an impedance bandwidth of 2.8 GHz at 100 GHz, a maximum radiation efficiency of 79.6% and a gain of 6.7 dBi and 13 dBi for the single antenna and array, respectively [12]. In [13], a similar approach was followed at 135 GHz, filling the cavity with a DuPont PerMX polymer, obtaining an impedance bandwidth of 4.5% and a gain of 6.4 dBi. Note that, although the impedance bandwidth for both aforementioned designs is not sufficient, the micro-machined cavities show great promise to enhance radiation efficiency as they shield the electromagnetic fields completely from the lossy silicon substrate.

The remainder of this chapter is organized as follows. Section 6.2 outlines the requirements for, and the implementation of the polymer-enabled AFSIW technology for THz on-chip antenna systems. Furthermore, it discusses the topology, design strategy, operation principle and final antenna dimensions of the antenna designed to demonstrate the performance of the polymer-enabled AFSIW technology. In Section 6.3, the antenna fabrication process is described. Finally, the simulation results for the proposed antenna are reported in Section 6.4, for both the unit element and 1x4 linear antenna array.

6.2 AFSIW Technology for Highly-Efficient THz On-Chip Antenna Systems

6.2.1 THz System Requirements

A compact and highly-efficient on-chip antenna is designed for phased arrays operating in the $[252.72-321.84]$ GHz frequency band of the IEEE 802.15.3d-2017 standard [4], defined for point-to-point communication links. Therefore, the magnitude of the reflection coefficient, $|S_{11}|$, with respect to 50 Ω, should be below -10 dB in the specified frequency band. However, given the constraining manufacturing tolerances at THz frequencies and to compensate for mutual coupling effects in array configurations, the reflection coefficient criteria are extended to

$$|S_{11}| \leq \begin{cases} -10\ dB & \forall f \in [247.67-328.28]\ \text{GHz} \\ -15\ dB & \forall f \in [257.77-315.40]\ \text{GHz}, \end{cases} \tag{6.1}$$

thereby providing a margin of 2% for the frequency boundaries and of 5 dB for the magnitude of the reflection coefficient within the frequency band of operation. Next, to facilitate beam steering up to ±30° with maximized gain, the unit antenna element gain is tailored to exhibit a Half-Power Beamwidth (HPBW) larger than 60°. Furthermore, a radiation efficiency over 90% and a FTBR larger than 10 dB are imposed for all frequencies of operation. Additionally, the unit antenna element footprint is restricted by

$$d_{max} = \frac{\lambda_{min}}{1+|\sin\theta_{max}|}, \tag{6.2}$$

where d_{max} is the inter-element spacing in a square lattice phased array, λ_{min} is the free-space wavelength at 321.84 GHz and θ_{max} is the maximal steering angle without undesired grating lobes. As such, to enable beam steering up to ±30° in a 2D phased array, the unit antenna element footprint is constrained to a maximum of 615 $\mu m \times 615\ \mu m$ ($\frac{2}{3}\lambda \times \frac{2}{3}\lambda$). Moreover, the mutual coupling between neighboring antenna elements should remain below -15 dB in the complete targeted frequency band.

Finally, to facilitate wafer-scale fabrication of phased arrays and to guarantee compliance with current microchip manufacturing processes, standard micromachining techniques are preferred to create a planar antenna system that satisfies the aforementioned design requirements.

6.2.2 Technology and antenna topology

It has been proven that cavity-backed topologies provide promising radiation characteristics to meet the proposed design requirements. In [14], [15], a compact polymer-filled cavity-backed patch antenna array is realized, showing a peak gain

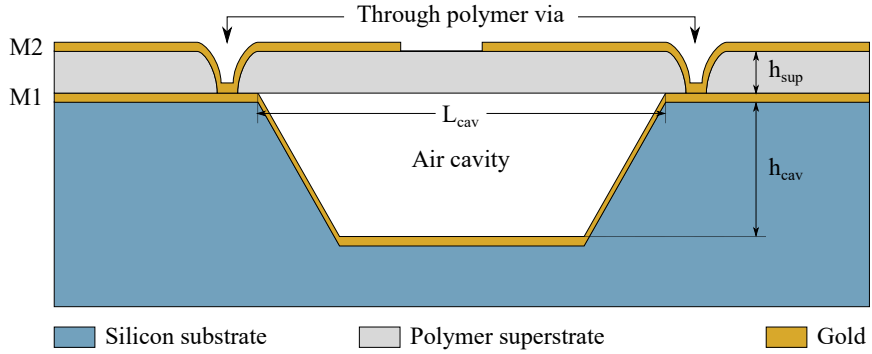

Figure 6.1: Polymer-enabled AFSIW technology for highly-efficient, broadband THz on-chip antenna systems.

of 13 dBi and 10.4 dBi at 100 GHz and 135 GHz, respectively, with minimal back radiation and mutual coupling levels below -28 dB. Nonetheless, the inherent narrow bandwidth of these antennas renders them ineffective for high data-rate wireless communication. These drawbacks are tackled in [16], where micromachining techniques and Printed Circuit Board (PCB) technology are used to realize a hybrid on-chip antenna at 28.5 GHz. Here, mode-bifurcation and AFSIW technology are leveraged to significantly enhance both the impedance bandwidth and radiation efficiency to 3.7 GHz (13%) and over 90%, respectively, within an antenna footprint of 0.49 $\lambda \times 0.49\ \lambda$. However, a modified AFSIW technology is required to scale the design towards THz frequencies, as the fabrication tolerances in commercial PCB manufacturing processes are too high. As such, a polymer-enabled AFSIW technology for highly-efficient, broadband on-chip THz antenna systems is proposed.

The proposed AFSIW technology is shown in Fig 6.1, showing the layer stack-up and the topological properties. It is comprised of a silicon substrate that embeds and supports a metallized air cavity and polymer superstrate, respectively. Metal layer 1 (M1) covers the complete silicon substrate (following the contours of the air cavities), thereby providing a stable Radio Frequency (RF) ground plane and excellent shielding from the lossy silicon substrate. In contrast to [16], where a high resistivity silicon substrate was required, the shielding provided in the proposed AFSIW technology allows the use of standard low-cost silicon substrates. On top of M1, a polymer superstrate with thickness h_{sup} is deposited to support metal layer 2 (M2), which contains both the antenna feeding section and the radiating elements. The superstrate thickness is constrained by two main aspects: electromagnetic performance and mechanical stability. In order to prevent significant losses associated with surface waves, h_{sup} is constrained by

$$\frac{h_{sup}}{\lambda} \leq \frac{0.3}{2\pi\sqrt{\epsilon_{r,sup}}}, \tag{6.3}$$

with $\epsilon_{r,sup}$ the polymer dielectric constant [17]. Next, the deflection of the superstrate spanning the air cavity δh_{sup} should be minimized to less than $h_{sup}/100$. This mitigates fabrication-tolerance-induced electromagnetic errors and guarantees a mechanically rigid membrane that doesn't collapse under its own weight. To this end, an exact solution for the deflection of a clamped rectangular plate under uniform load is found in [18]. The deflection in the center of the plate under its own weight is given by

$$\delta h_{sup} = \frac{6\pi L_{cav} W_{cav}^3 \rho_{sup} g(1-\nu_{sup})}{E_{sup} h_{sup}^2}, \tag{6.4}$$

with L_{cav}, W_{cav} the air cavity length and width, respectively, g the acceleration due to gravity, and ρ_{sup}, ν_{sup} and E_{sup} being the specific mass, Poisson's ratio and Young's modulus of the polymer superstrate, respectively. Taking (6.3) and (6.4) into account, the following set of inequalities is compiled

$$\begin{cases} h_{sup} \leq \frac{0.3\lambda}{2\pi\sqrt{\epsilon_{r,sup}}} \\ h_{sup} \geq \sqrt[3]{\frac{600\pi L_{cav} W_{cav}^3 \rho_{sup} g(1-\nu_{sup})}{E_{sup}}} \end{cases}. \tag{6.5}$$

Considering a square cavity with dimensions $\frac{2}{3}\lambda \times \frac{2}{3}\lambda \times 0.1\ \lambda$, the superstrate height is constrained in terms of cavity dimensions as

$$\sqrt[3]{\frac{600\pi L_{cav}^4 \rho_{sup} g(1-\nu_{sup})}{E_{sup}}} \leq h_{sup} \leq \frac{0.9 L_{cav}}{4\pi\sqrt{\epsilon_{r,sup}}}. \tag{6.6}$$

Next, additional constraints are imposed on the thermal properties of the polymer superstrate to minimize thermal stress $\sigma_{th,sup}$ on the air-suspended superstrate, given by [19]

$$\sigma_{th,sup} = \frac{E_{sup}}{1-\nu_{sup}} \left(\alpha_{sup} - \alpha_{Si}\right) \Delta T, \tag{6.7}$$

where α_{sup} and $\alpha_{Si} = 2.6 ppm/K$ are the thermal expansion coefficients (CTE) of the superstrate and the silicon substrate, respectively. As the temperature difference ΔT is not controllable in most cases, the difference in CTE should be minimized. Additionally, a thermosetting polymer superstrate is preferred to facilitate post-processing procedures at high temperature, as is required for some packaging techniques.

Finally, a polymer needs to be selected that minimizes (6.4) and (6.7). An overview of the most prominent low-loss polymers for mmWave and THz applications is provided in Table 6.1, displaying their relevant thermal, mechanical and electrical

Table 6.1: Summary of material properties (at 200 GHz) for common polymers in THz applications.

Material	α **[ppm/K]**	ρ **[kg/m^3]**	ν	E **[GPa]**	ϵ_r	$\tan\delta$
SU-8	52	1190	0.22	4.0	2.73	0.025
Parylene-C	35	1289	0.40	2.8	2.95	0.0056
Parylene-N	69	1100	0.40	2.4	2.63	0.0056
Polystyrene	65	1052	0.35	3.25	2.59	0.0067
SUEX	63	*	*	3.9	2.86	0.0200
Polyimide	40	1420	0.34	2.5	3.43	0.0035
COC	60	1020	0.37	3.0	2.35	0.0009
BCB	42	956	0.34	2.9	2.45	0.007

characteristics [20]–[24]. Although several materials exhibit promising properties, polyimide and BCB are the only thermosetting polymers in the list. When analyzing the material characteristics in Table 6.1, BCB displays the most favorable qualities and, as such, it is selected to implement the superstrate in the polymer-enabled AFSIW technology.

Now that the polymer-enabled AFSIW technology and its constraints have been defined, a suitable antenna topology needs to be chosen that fulfills the imposed design requirements. Note that, as M2 is the only metal layer to contain radiating elements, the stacked-patch configuration in [16] is not feasible. However, in [25], a cavity-backed slot antenna is realized in AFSIW technology, exhibiting an impedance bandwidth of 29.4% by leveraging mode-bifurcation between two coupled half-mode rectangular cavities. These distinct half-mode cavities are created by inserting a slot in the top metal layer of a rectangular cavity. Consequently, as depicted in Fig 6.2, realizing the air-filled cavity in the silicon substrate and the slot in M2, a cavity-backed slot antenna is realized in the proposed AFSIW technology. Furthermore, the antenna is fed by a tapered Grounded Co-Planar Waveguide (GCPW) to compensate for the slanted sidewalls of the cavity and, as such, ensure broad impedance matching.

6.2.3 Design strategy and operation principle

Now that the antenna technology is defined and a suitable topology is selected, the proposed design can be tailored to meet the specified requirements. The cavity-backed slot antenna with linearly tapered GCPW, depicted in Fig. 6.2, is selected as a starting point for the design process. Similar to [25], this design leverages mode-bifurcation to obtain ultra-wideband operation by judiciously coupling two half-mode cavities, half-mode cavity A and B, with distinct resonant frequencies $f_{110,a}$ and $f_{110,b}$, respectively. The impedance bandwidth is then optimized by controlling the amount of coupling, determined by the slot dimensions (L_{slot} and W_{slot}), and

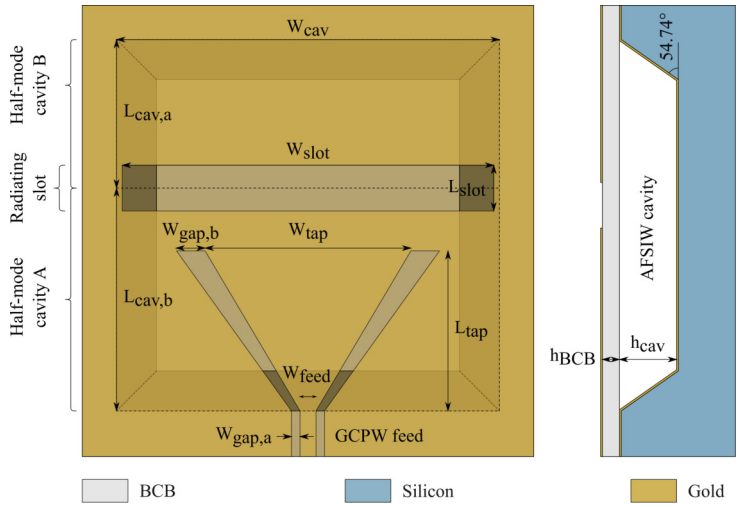

Figure 6.2: Topology: cavity-backed slot on-chip antenna in AFSIW technology.

setting the TE_{110} half-mode cavity resonant frequencies, defined by [26]

$$f_{110,i} = \left(1 - \frac{\epsilon_{r,sup} - 1}{2(h_{cav} + h_{BCB})} h_{BCB}\right) \frac{c}{2\pi} \sqrt{\left(\frac{\pi}{W_{cav}}\right)^2 + \left(\frac{\pi}{2L_{cav,i}}\right)^2}, \tag{6.8}$$

with c the speed of light, $\epsilon_{r,sup}$ the dielectric constant of the BCB superstrate, $L_{cav,i}$, W_{cav} and h_{cav} the half-mode cavity length, width and height, respectively, and h_{BCB} the superstrate height, as depicted in Fig. 6.2. The superstrate height is fixed at 10 µm for fabrication ease and to enable measurements with a 25 µm-pitch Ground-Signal-Ground (GSG) probe, thereby complying with the imposed superstrate constraints defined by (6.6), implying $6.5\ \mu m \leq h_{sup} \leq 21.6\ \mu m$. The dimensions after optimization of the initial rectangular slot antenna with linearly tapered GCPW feed are provided in Table 6.2, resulting in $f_{res,a} = 281$ GHz and $f_{res,b} = 363$ GHz. The resulting simulation results are depicted in Fig. 6.3(d) and (e), showing an impedance bandwidth of 102 GHz centered around 299 GHz. Although this design comfortably covers the targeted frequency band, its antenna footprint should be reduced, as it exceeds $\frac{2}{3}\lambda \times \frac{2}{3}\lambda = 615\ \mu m \times 615\ \mu m$.

Reducing the cavity size

In order to scale down the antenna footprint, it is critical to reduce both the half-mode cavity dimensions, thereby increasing their respective resonant frequencies, and the slot dimensions. Although impedance matching can be obtained in the targeted frequency band with reduced cavity lengths, reducing the rectangular slot width and, hence, the cavity width results in a significant loss in impedance

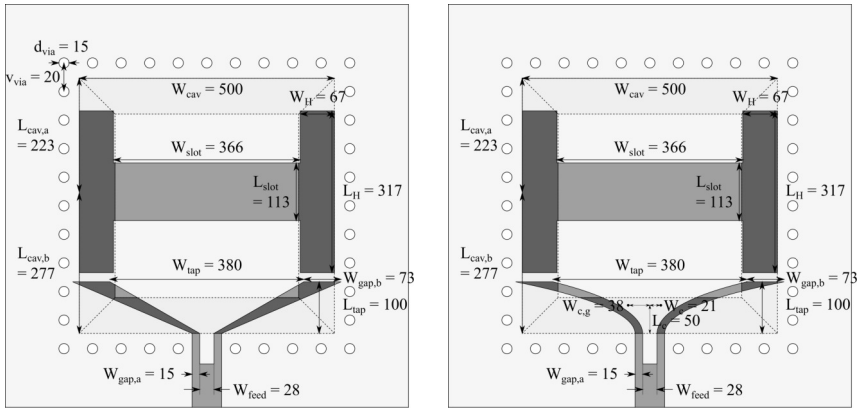

(a) (b)

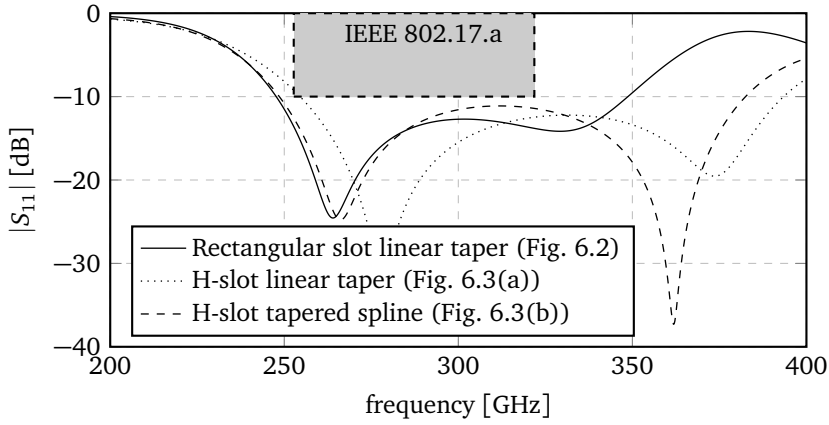

(c)

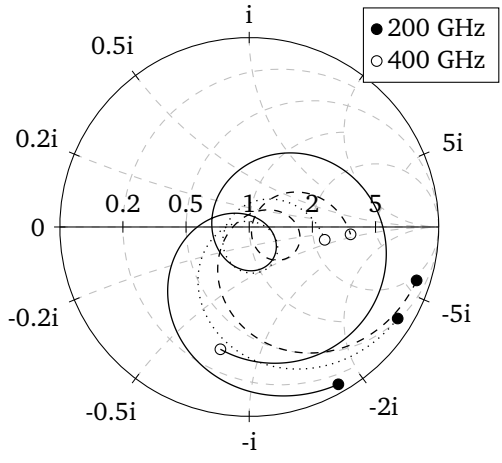

(d)

Figure 6.3: Design procedure: Reducing the cavity size.

Table 6.2: Dimensions after optimization of the initial rectangular slot antenna with linearly tapered GCPW feed.

Dimension	Value [µm]	Dimension	Value [µm]
W_{cav}	670	$L_{cav,a}$	260
W_{slot}	650	$L_{cav,b}$	390
W_{tap}	360	L_{slot}	80
$W_{gap,b}$	50	L_{tap}	280
W_{feed}	28	$L_{gap,a}$	15
h_{cav}	100	h_{BCB}	10

bandwidth. Therefore, as described in [27], the rectangular slot is replaced by an H-shaped slot to arrive at a miniaturized antenna footprint. The dimensions after optimization of the H-slot antenna with linearly tapered GCPW feed are provided in Fig. 6.3(b), with a cavity height of 90 µm and half-mode cavity resonance frequencies $f_{res,a} = 375$ GHz and $f_{res,b} = 418$ GHz, according to (6.8). The resulting simulation results are depicted in Fig. 6.3(d) and (e), showing an impedance bandwidth of 140 GHz centered around 325 GHz. As seen on the smith chart in Fig. 6.3(e), the implementation of the H-shaped slot did not only reduce the cavity size, it also decreased the coupling between both half-mode cavities. This reduction in coupling is required to compensate for the increased resonance frequencies of the half-mode cavities, ensuring that the reflection coefficient remains below -10 dB in the targeted frequency band.

Unfortunately, the H-slot antenna with linearly tapered GCPW feed fails to cover the lower frequencies of the 802.15.3d-2017 standard and, thus, a third optimization step is performed to lower its frequency band of operation. Because of the slanted cavity sidewalls, the cavity height (and thus the stack-up of BCB and air) varies as a function of the taper length. Furthermore, the reduction in taper length compared to the design represented in Fig. 6.2, changes the input impedance of the antenna, thereby requiring additional matching in the feed section. Thereto, the linearly tapered GCPW feed is replaced by a tapered spline GCPW feed, which provides more degrees of freedom during the optimization process and allows to incorporate the required impedance matching in the antenna feed. The dimensions after optimization of the tapered spline GCPW feed are provided in Fig. 6.3(c), where W_c, $W_{c,g}$ and L_c determine the position of the third control point of the second degree splines that define the tapered spline GCPW. The resulting simulation results are depicted in Fig. 6.3(d) and (e), showing an impedance bandwidth of 135 GHz centered around 315 GHz. Further analysis of the smith chart, depicted in Fig. 6.3(e), shows that the impedance transformation in the feed network does not alter the coupling or impedance bandwidth, but it shifts the input impedance such that the reflection coefficient for the lower frequencies is below -10 dB.

Improving the impedance matching

Finally, as seen in Fig.6.4(c), the H-shaped slot antenna with tapered spline GCPW feed covers the IEEE 802.15.3d-2017 frequency band, but the antenna does not fully comply with the imposed design requirements. As such, a final optimization step is required to improve the impedance matching in the complete targeted frequency band, as such, ensuring sufficient robustness against manufacturing tolerances. As shown in [28], the amount of coupling between the two half-mode cavities impacts the bandwidth and the amplitude of the reflection coefficient. Fig. 6.4(c) and Fig. 6.4(d) show that stronger coupling results in a larger separation between the two resonances and a higher reflection coefficient between them. Hence, the amount of coupling should be reduced by increasing the slot length where the coupling is strongest to improve the impedance matching. To prevent the lower resonance frequency of the antenna to increase, the slot shape is further modified by tapering the slot inward when approaching the H-section of the slot. This taper, along with the additional inductive stubs at the top and bottom parts on both sides of the H-section, increase the current path of the slot and significantly improve the impedance matching, especially at lower frequencies [29]. The final design after optimization of the modified slot is shown in Fig. 6.4(b). The resulting simulation results are depicted in Fig. 6.4(c) and (d), showing an impedance bandwidth of 108 GHz centered around 301 GHz. When analyzing the smith chart in Fig. 6.4(d), the modified slot shifts the loop area of the resonance is decreased, indicating a lower amount of coupling. Furthermore, the effect of the inductive stubs in the slot can be seen as it shifts the antenna impedance more towards the origin of the smith chart, thereby significantly improving the impedance matching.

6.2.4 Final antenna dimensions

An annotated representation of the on-chip cavity-backed slot antenna in polymer-enabled AFSIW technology, optimized using CST Microwave Studio, is provided in Fig. 6.5 and its dimensions are listed in Table 6.3.

6.3 Fabrication Process

The cavity-backed slot antenna in AFSIW technology is fabricated in nine steps, depicted in Fig. 6.6, using standard micromachining techniques. The complete fabrication process is performed in the clean room of Ghent University.

1. Cavity etching: A 600 nm Si_3N_4 hard mask is deposited on both sides of a 500µm-thick, polished, undoped (100) silicon substrate using Plasma Enhanced Chemical Vapor Deposition (PECVD). Next, the Suss Microtech MA6 mask aligner is used to pattern a soft mask on the silicon samples, which is followed by a Reactive Ion Etching (RIE) process to transfer the cavity

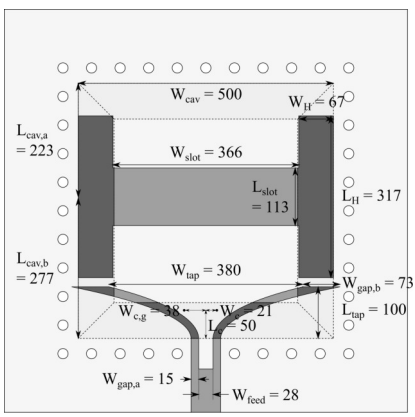

(a)

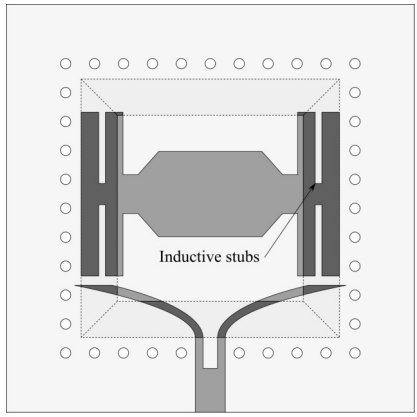

(b)

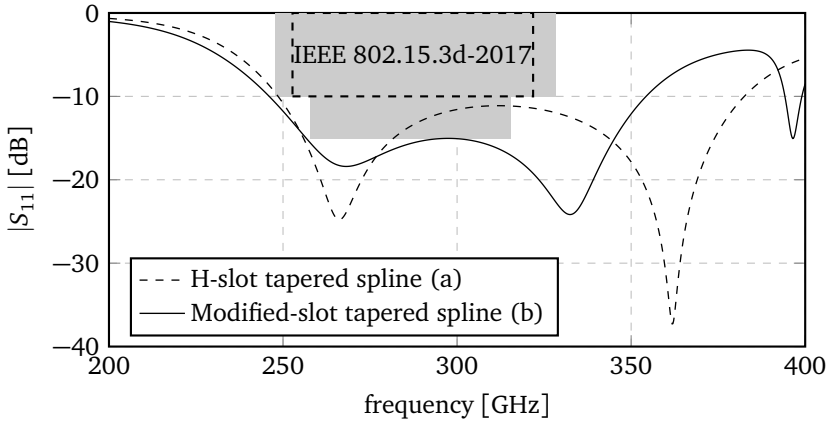

(c)

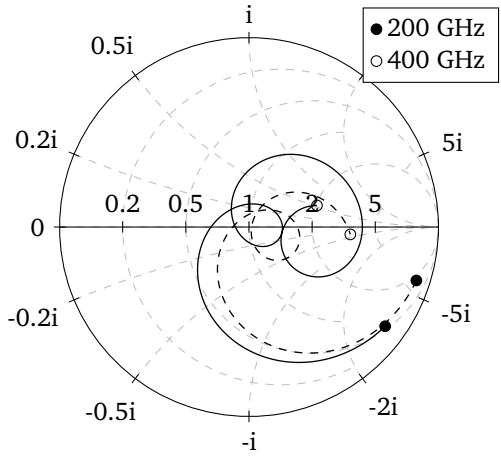

(d)

Figure 6.4: Design procedure: Improving the impedance matching.

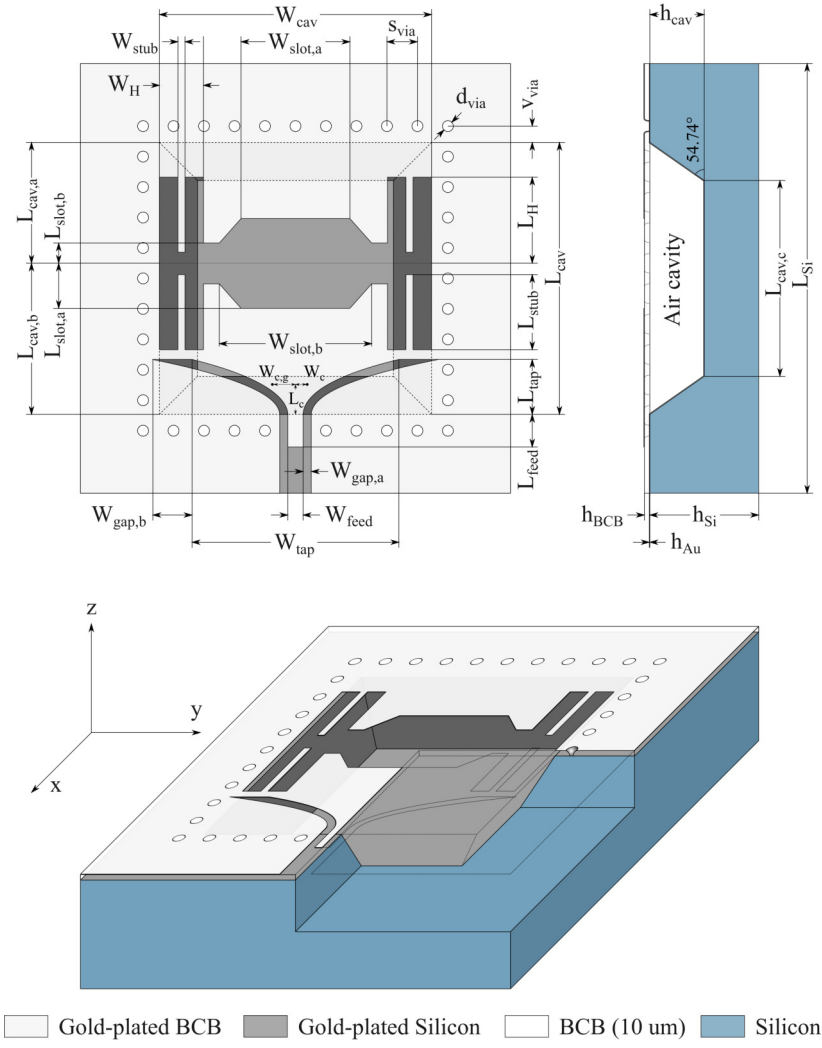

Figure 6.5: Annotated representation of the optimized on-chip cavity-backed slot antenna in polymer-enabled AFSIW technology.

Table 6.3: Final antenna dimensions in µm.

Dimension	Value	Dimension	Value	Dimension	Value
W_{cav}	500.0	L_{cav}	500.0	L_{feed}	60.0
$W_{slot,a}$	200.0	$L_{cav,a}$	222.5	L_{tap}	101.2
$W_{slot,b}$	280.0	$L_{cav,b}$	277.5	L_{Si}	700.0
W_H	80.8	$L_{cav,c}$	372.7	d_{via}	15.0
W_{feed}	28.0	$L_{slot,a}$	82.5	v_{via}	44.6
W_{tap}	380.0	$L_{slot,b}$	37.5	h_{cav}	90.0
$W_{gap,a}$	15.0	L_{stub}	137.6	h_{BCB}	10.0
$W_{gap,b}$	73.1	L_H	158.8	h_{Au}	1.0
W_{stub}	13.4	L_c	50.0	$W_{c,g}$	38.0
W_c	21.0				

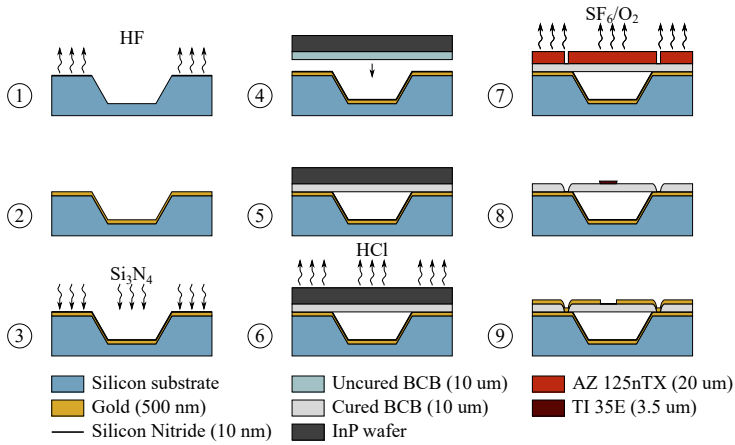

Figure 6.6: Fabrication steps for the polymer-enabled AFSIW technology for highly-efficient, broadband on-chip THz antenna systems.

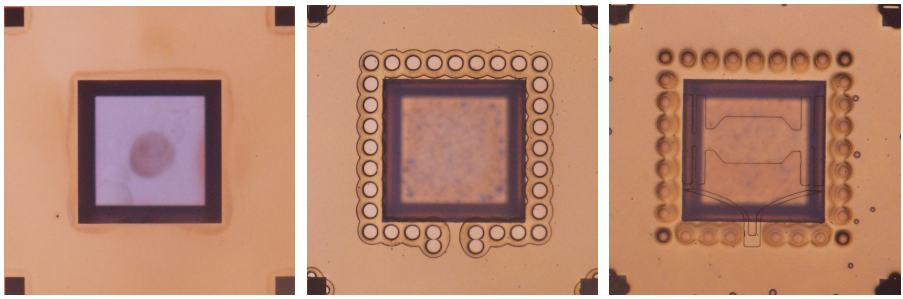

(a) (b) (c)

Figure 6.7: Microscopic view of the samples after (a) fabrication step 3, (b) fabrication step 7 and (c) fabrication step 8.

pattern onto the hard mask. Subsequently, a 95 µm-deep cavity is etched in a 20% KOH solution, heated up to 86 C° (resulting in an etch rate of 1.6 µm/min), for 56 min. Finally, the remaining Si_3N_4 is removed using a 44% HF solution.

2. Metallization I: The top side of the silicon sample (containing the cavity) is metallized by means of sputtering, depositing a 500 nm gold (Au) layer. Note that a 10 nm titanium (Ti) layer is predeposited to promote adhesion between silicon and gold.

3. Adhesion promotor: As stated in [30], BCB does not adhere well to gold, or other noble metals. Furthermore, because gold does not form a surface oxide, an adhesion promoter such as AP3000 won't provide the required bonding strength between gold and BCB. To this end, a 10 nm Si_3N_4 adhesion promoter layer is deposited using PECVD. A microscopic view of the fabricated metallized cavity with adhesion promotor is depicted in Fig. 6.7(a).

4. BCB film preparation: To create a 10 µm-thick BCB superstrate, BCB resin (Cyclotene 3022-57 [31]) is spun onto a sacrificial indium phosphide (InP) wafer at 1600 rpm. After the spin coating process, the BCB film is placed on a hotplate at 150 C°, which is ramped up to 180 C°, for 30 min. This removes solvents and avoids material flow during the next processing step.

5. BCB hard cure: As no alignment is required for the bonding process, the uncured BCB film is pushed on the metallized sample to hermetically seal the air cavity underneath. Next, the sample is placed between two glass substrates and placed inside the Suss Microtech CB6L Substrate Bonder. To minimize oxidation of and voids in the BCB superstrate, the bonding chamber is placed under high vacuum. Furthermore, a bonding force of 2 kN is applied, corresponding to a bonding pressure of 2.5 bar. Finally, a hard cure is achieved with the curing profile displayed in Fig 6.8.

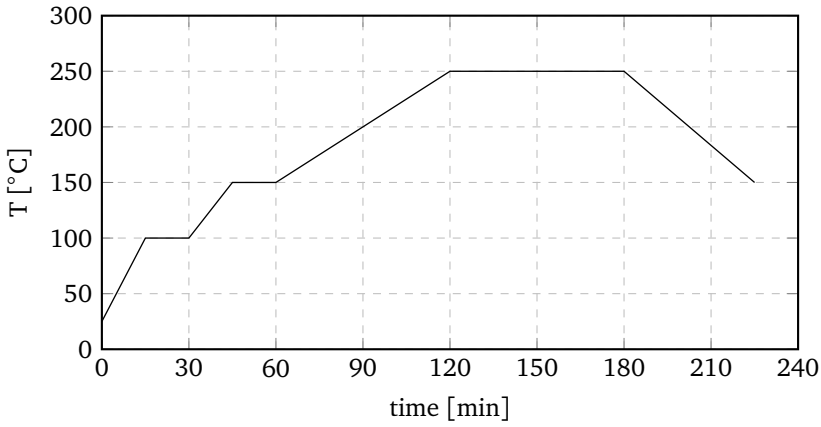

Figure 6.8: Curing profile for a hard cure of Cyclotene 3022-57.

6. InP removal: The sacrificial InP wafer is removed by submerging the sample in HCl for 30 min. While the silicon is unaffected by the HCl, the InP slowly dissolves, leading to the required air-suspended BCB superstrate.

7. Via definition: To fabricate the vias into the BCB superstrate, a SF_6/O_2 plasma anisotropic dry etch is performed in an Inductively Coupled Plasma (ICP) etcher. To transfer the via pattern, both a Si_3N_4 hard mask and a soft mask can be used. A hard mask would result in high aspect-ratio cylinders, whereas the soft mask creates an exponentially tapered sidewall profile [31]. To enhance the via metallization, a 20 µm-thick AZ 125nXT-10 [32] soft mask is applied, especially suited for high aspect-ratio features in thick layers. A microscopic view of the fabricated vias in the BCB superstrate is depicted in Fig. 6.7(b).

8. Lift-off preparation: Once the dry etching step is complete, the AZ 125nXT-10 resin is removed and the sample is cleaned. Next, a 3.5 µm-thick TI 35E [33] layer is applied and patterned using the SUSS Microtech MA6. The inverse slanted sidewalls of the developed TI 35E layer are required to facilitate lift-off. A microscopic view of the sample with TI 35E layer on top of the BCB superstrate is depicted in Fig. 6.7(c).

9. Metallization II: The top side of the sample is metallized by means of sputtering, depositing a 500 nm Au layer. Next, a lift-off procedure is performed by dissolving the TI 35E layer in acetone, thereby removing the gold layer on top of that layer and patterning the Au on the BCB superstrate. Note that, a 10 nm titanium (Ti) layer is predeposited to promote adhesion between BCB and gold.

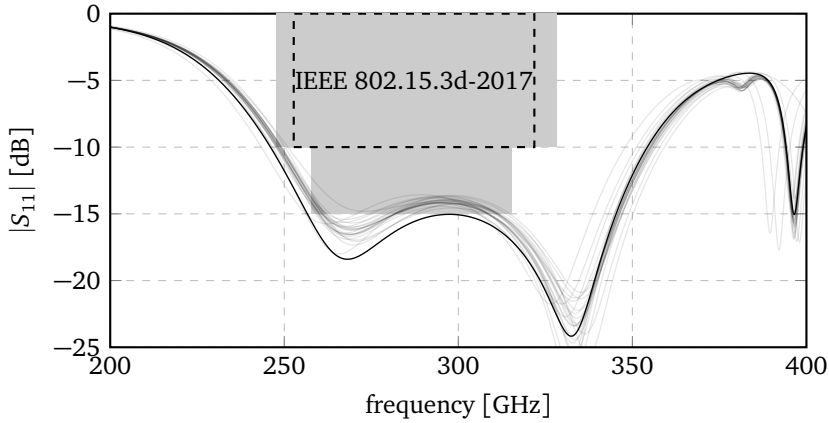

Figure 6.9: Simulated reflection coefficient $|S_{11}|$ w.r.t. 50 Ω. The gray traces represent the parameter sweep results and the gray rectangles represent the optimization criteria.

6.4 Simulation Results

The simulation results for a standalone unit element and a 1x4 linear array are discussed below. All simulations are performed using the frequency domain solver in CST Microwave Studio.

6.4.1 Unit element

The simulated reflection coefficient of the unit antenna element w.r.t. 50 Ω, depicted in Fig. 6.9, shows impedance matching below -10 dB and -15 dB in the $[248.0-355.0]$ GHz and $[260.0-290.0]$ GHz frequency band, respectively. As such, any performance degradation due to fabrication tolerances, represented by the gray traces in Fig. 6.9, or mutual coupling in array configurations is mitigated within the IEEE 802.15.3d-2017 frequency band. Furthermore, besides a facilitating a large fractional bandwidth, the effect of the polymer-enabled AFSIW technology is clear as the total antenna efficiency, depicted in Fig. 6.10, remains above 88% for all frequencies of interest. Moreover, a FTBR above 14.4 dB is obtained for all frequencies of interest, as can be seen in Fig. 6.10.

The simulated co-polarized and cross-polarized antenna gain at 252.72 GHz, 287.28 GHz and 321.84 GHz are depicted in Fig. 6.11. The maximum co-polarized gain for the azimuth plane (yz-plane), depicted on the left plot of Fig. 6.11, is 4.87 dBi, 5.69 dBi and 5.79 dBi at 252.72 GHz, 287.28 GHz and 321.84 GHz, respectively. The simulated HPBW in the yz-plane equals 81.3°, 77.1° and 75.1° at 252.72 GHz, 287.28 GHz and 321.84 GHz, respectively. In the xz-plane, depicted in the right plot of Fig. 6.11, a maximum co-polarized gain of 5.32 dBi (at $\theta = 20°$), 5.81 dBi (at $\theta = 9°$) and 5.81 dBi (at $\theta = 3°$) is obtained at 252.72 GHz, 287.28 GHz and

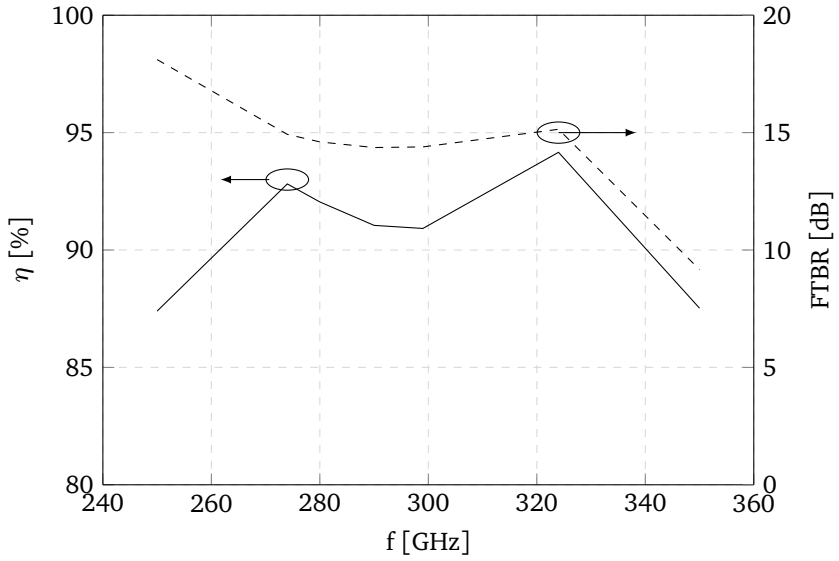

Figure 6.10: Simulated total antenna efficiency η [%] (left) and FTBR [dB] (right) as a function of frequency.

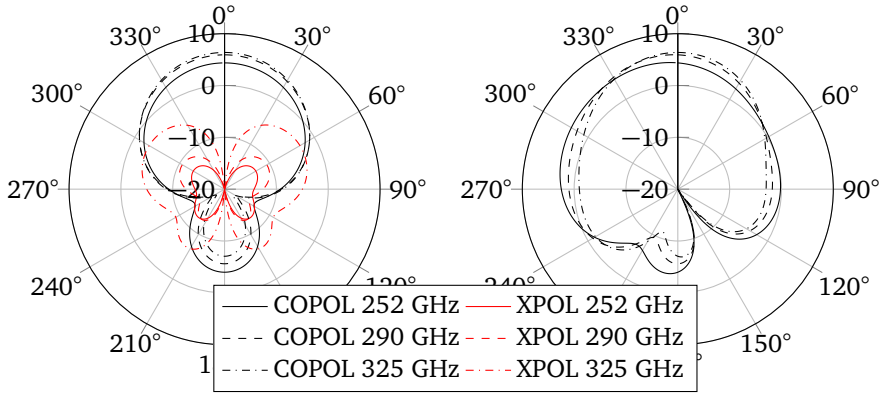

Figure 6.11: Simulated co-polarized (black) and cross-polarized (red) antenna gain at 252.72 GHz, 287.28 GHz and 321.84 GHz. (left) yz-plane, (right) xz-plane.

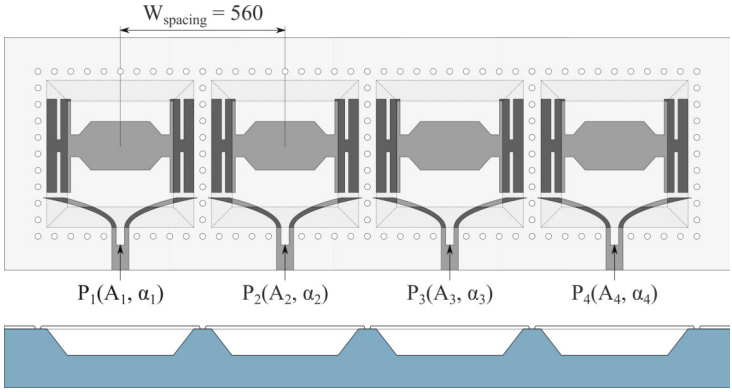

Figure 6.12: Annotated representation of the 1x4 linear on-chip cavity-backed slot antenna array in polymer-enabled AFSIW technology.

321.84 GHz, respectively. The HPBW in the xz-plane equals 111.9°, 104.4° and 92.3° at 252.72 GHz, 287.28 GHz and 321.84 GHz, respectively.

6.4.2 1x4 linear array

To demonstrate the beamsteering capabilities of the designed antenna, a 1x4 linear antenna array is designed in polymer-enabled AFSIW technology and simulated. To enable beam steering up to ±30° without grating lobes, the inter-element spacing cannot exceed 615 µm. However, the mutual coupling remains below -15 dB up to an inter-element spacing of 560 µm (0.6 λ), resulting in the array depicted in Fig. 6.12. The excitation at each antenna element, indicated by P_i, is defined by

$$A_i = 1 \tag{6.9}$$

$$\alpha_i = (1.5 - i)\Delta\alpha, \tag{6.10}$$

where A_i and α_i are the excitation amplitude and phase, respectively, and $\Delta\alpha$ is the progressive phase shift throughout the array. To assess the beam steering capabilities, the beam is steered to $\theta = 0°$ and $\theta = 30°$ by exciting the array with a $\Delta\alpha = 0°$ and $\Delta\alpha = 100°$, respectively.

The simulated embedded S-parameters, depicted in Fig. 6.13, show that the reflection coefficient at each port remains below -10 dB within the frequency band of operation. Furthermore, it can be seen that the mutual coupling levels remain below -15 dB in the complete targeted frequency band. The active reflection coefficients, represented by the active S-parameters and depicted in Fig. 6.14, remain below -10 dB in the complete frequency band of operation, for the progressive phase shifts $\Delta\alpha = 0°$ and $\Delta\alpha = 100°$, guaranteeing that the efficiency does not deteriorate when steering the beam to $\theta = \pm 30°$.

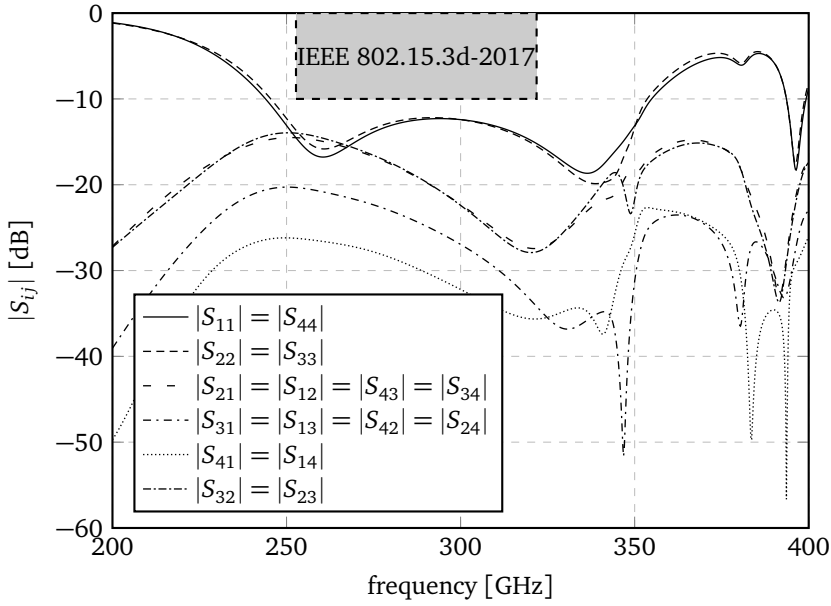

Figure 6.13: Simulated S-parameters w.r.t. 50 Ω for the 1x4 linear array with an inter-element spacing of 560 µm.

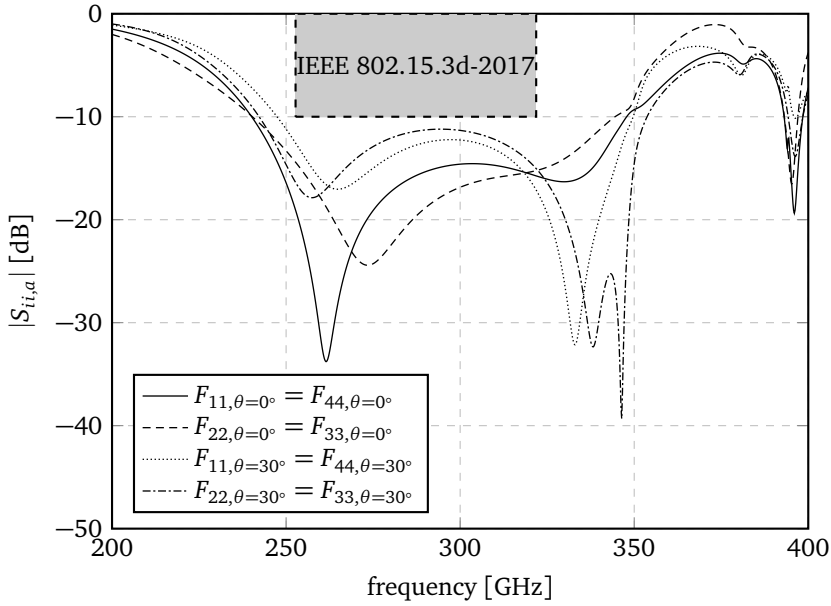

Figure 6.14: Simulated active S-parameters w.r.t. 50 Ω for the 1x4 linear array with an inter-element spacing of 560 µm.

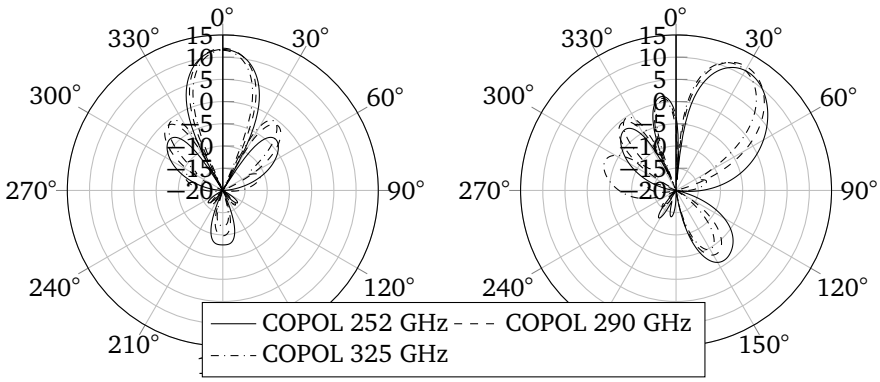

Figure 6.15: Simulated co-polarized boresight antenna array gain at 252.72, 287.28 and 321.84 GHz in the yz-plane. (left) $\Delta\alpha = 0°$, steering to $\theta = 0°$, (right) $\Delta\alpha = 100°$, steering to $\theta = 30°$.

Fig. 6.15 shows the simulated array gain in the plane defined by rotating the yz-plane around the x-axis by 40°, thereby including the boresight gain in the plot. The maximum co-polarized gain when steering the beam to $\theta = 0°$, depicted on the left plot of Fig. 6.11, equals 11.75 dBi, 12.02 dBi and 11.54 dBi (corresponding to a total antenna efficiency of 92%, 94% and 93%) for 252.72 GHz, 287.28 GHz and 321.84 GHz, respectively. Remark that the reduced inter-element spacing of 560 µm results in a reduced sidelobe level, generated by grating lobes. The simulated HPBW equals 26.2°, 23.6° and 21.7° at 252.72 GHz, 287.28 GHz and 321.84 GHz, respectively. Furthermore, a FTBR above 16.8 dB is obtained for all frequencies of interest. The maximum co-polarized gain when steering the beam to $\theta = 30°$, depicted on the right plot of Fig. 6.11, amounts to 11.26 dBi, 12.09 dBi and 11.60 dBi (corresponding to a total antenna efficiency of 90%, 90% and 93%) at 252.72 GHz, 287.28 GHz and 321.84 GHz, respectively.

6.5 Conclusion

This chapter proposed a novel polymer-enabled AFSIW technology for cost-effective, highly-efficient, broadband on-chip THz multi-antenna systems. To validate the technology, a cavity-backed slot antenna with exponentially tapered feed and modified slot was designed in both a stand-alone and 1x4 linear array configuration, optimized for compliance with the IEEE 802.15.3d-2017 standard.

By suspending a thin, low-loss polymer superstrate, containing both the radiating elements and antenna feed, on top of a metallized AFSIW cavity inside a bulk silicon substrate, a low-cost fabrication technology is obtained for highly efficient Ultra-Wideband (UWB) THz antennas. In addition to frequency-domain characterization, both a mechanical and a thermal analysis were performed to guarantee robust antenna operation. A detailed fabrication procedure, based on bulk sili-

con micromachining techniques, was discussed to facilitate the easy realization of different antenna designs in a clean room environment.

Next, a cavity-backed slot antenna with exponentially tapered feed and modified slot was designed in AFSIW technology in both a stand-alone and a 1x4 linear array configuration, for operation in the $[252.72-321.84]$ GHz frequency band of the IEEE 802.15.3d-2017 standard. Initially, a conventional cavity-backed slot antenna is reduced in size, to fit within an antenna footprint of $615\ \mu m \times 615\ \mu m$, obtained by altering the rectangular slot to a modified H-shaped slot. Next, the impedance bandwidth is improved by changing the linearly tapered GCPW feed in the initial design to an exponentially tapered GCPW feed. As a result, the final unit antenna element exhibited very high radiation efficiency over the complete targeted frequency band of operation. This unit antenna element is integrated into a 1x4 linear array configuration, demonstrating grating-lobe free beam-steering capabilities up to 30°.

References

[1] Z. Chen, X. Ma, B. Zhang, Y. Zhang, Z. Niu, N. Kuang, W. Chen, L. Li, and S. Li, "A Survey on Terahertz Communications", *China Communications*, vol. 16, no. 2, pp. 1–35, 2019.

[2] T. S. Rappaport, Y. Xing, O. Kanhere, S. Ju, A. Madanayake, S. Mandal, A. Alkhateeb, and G. C. Trichopoulos, "Wireless Communications and Applications Above 100 GHz: Opportunities and Challenges for 6G and Beyond", *IEEE Access*, vol. 7, pp. 78 729–78 757, 2019.

[3] H.-J. Song and T. Nagatsuma, "Present and Future of Terahertz Communications", *IEEE Transactions on Terahertz Science and Technology*, vol. 1, no. 1, pp. 256–263, 2011.

[4] "IEEE Standard for High Data Rate Wireless Multi-Media Networks–Amendment 2: 100 Gb/s Wireless Switched Point-to-Point Physical Layer", *IEEE Std 802.15.3d-2017 (Amendment to IEEE Std 802.15.3-2016 as amended by IEEE Std 802.15.3e-2017)*, pp. 1–55, 2017.

[5] V. Petrov, T. Kurner, and I. Hosako, "IEEE 802.15.3d: First Standardization Efforts for Sub-Terahertz Band Communications toward 6G", *IEEE Communications Magazine*, vol. 58, no. 11, pp. 28–33, 2020.

[6] X. Fu, F. Yang, C. Liu, X. Wu, and T. J. Cui, "Terahertz Beam Steering Technologies: From Phased Arrays to Field-Programmable Metasurfaces", *Advanced Optical Materials*, vol. 8, no. 3, p. 1 900 628, 2020.

[7] X.-D. Deng, Y. Li, C. Liu, W. Wu, and Y.-Z. Xiong, "340 GHz On-Chip 3-D Antenna With 10 dBi Gain and 80Radiation Efficiency", *IEEE Transactions on Terahertz Science and Technology*, vol. 5, no. 4, pp. 619–627, 2015.

[8] Y. He, Y. Chen, L. Zhang, S.-W. Wong, and Z. N. Chen, "An Overview of Terahertz Antennas", *China Communications*, vol. 17, no. 7, pp. 124–165, 2020.

[9] C. Jastrow, "300GHz Transmission System", English, *Electronics Letters*, vol. 44, 213–214(1), 3 2008.

[10] Y. Shang, H. Yu, C. Yang, Y. Liang, and W. M. Lim, "A 239281GHz Sub-THz Imager with 100MHz Resolution by CMOS Direct-Conversion Receiver with On-Chip Circular-Polarized SIW Antenna", in *Proceedings of the IEEE 2014 Custom Integrated Circuits Conference*, 2014, pp. 1–4.

[11] J. Al-Eryani, H. Knapp, J. Kammerer, K. Aufinger, H. Li, and L. Maurer, "Fully Integrated Single-Chip 305375-GHz Transceiver With On-Chip Antennas in SiGe BiCMOS", *IEEE Transactions on Terahertz Science and Technology*, vol. 8, no. 3, pp. 329–339, 2018.

[12] J. Liu, S. Chen, K. Xiao, and X. Chen, "100 GHz Silicon-based Micro-Machined Patch Antenna and Arrays", *The Journal of Engineering*, vol. 2019, no. 19, pp. 5622–5625, 2019.

[13] S. B. Yeap, Z. N. Chen, L. Rui, D. S. W. Ho, and L. T. Guan, "135-GHz Co-Planar Patch Array on BCB/Silicon with Polymer-Filled Cavity", in *2011 International Workshop on Antenna Technology (iWAT)*, 2011, pp. 344–347.

[14] J. Liu, S. Chen, K. Xiao, and X. Chen, "100GHz Silicon-based Micro-Machined Patch Antenna and Arrays", *The Journal of Engineering*, vol. 2019, no. 19, pp. 5622–5625, 2019.

[15] S. B. Yeap, Z. N. Chen, X. Qing, L. Rui, D. S. W. Ho, and L. T. Guan, "135GHz Antenna Array on BCB Membrane backed by Polymer-Filled Cavity", in *2012 6th European Conference on Antennas and Propagation (EUCAP)*, 2012, pp. 1337–1340.

[16] Q. Van den Brande, S. Lemey, S. Cuyvers, S. Poelman, L. De Brabander, O. Caytan, L. Bogaert, I. L. D. Paula, S. Verstuyft, A. C. F. Reniers, B. Smolders, B. Kuyken, D. V. Ginste, and H. Rogier, "A Hybrid Integration Strategy for Compact, Broadband, and Highly Efficient Millimeter-Wave On-Chip Antennas", *IEEE Antennas and Wireless Propagation Letters*, vol. 18, no. 11, pp. 2424–2428, 2019.

[17] R. Garg, P. Bhartia, I. J. Bahl, and A. Ittipiboon, *Microstrip Antenna Design Handbook*. Artech house, 2001, ch. 1.

[18] C. Imrak and I Gerdemeli, "An exact solution for the deflection of a clamped rectangular plate under uniform load", *Applied Mathematical Sciences*, vol. 1, no. 43, pp. 2129–2137, 2007.

[19] M. Woehrmann and M. Toepper, "Polymerization of Thin Film Polymers", *New Polymers for Special Applications*, pp. 113–138, 2012.

[20] S. Sahin, N. K. Nahar, and K. Sertel, "Dielectric Properties of Low-Loss Polymers for mmW and THz Applications", *Journal of Infrared, Millimeter, and Terahertz Waves*, vol. 40, no. 5, pp. 557–573, 2019.

[21] B. Kim and E. Meng, "Review of Polymer MEMS Micromachining", *Journal of Micromechanics and Microengineering*, vol. 26, p. 013 001, 2016.

[22] G. Di Massa, S. Costanzo, A. Borgia, F. Venneri, and I. Venneri, "Innovative Dielectric Materials at Millimeter-Frequencies", in *2010 Conference Proceedings ICECom, 20th International Conference on Applied Electromagnetics and Communications*, 2010, pp. 1–4.

[23] F. Pavanello, G. Ducournau, E. Peytavit, S. Lepilliet, and J. Lampin, "High-Gain YagiUda Antenna on Cyclic Olefin Copolymer Substrate for 300-GHz Applications", *IEEE Antennas and Wireless Propagation Letters*, vol. 13, pp. 939–942, 2014.

[24] E. Perret, N. Zerounian, S. David, and F. Aniel, "Complex permittivity characterization of benzocyclobutene for terahertz applications", *Microelectronic Engineering*, vol. 85, no. 11, pp. 2276 –2281, 2008.

[25] Q. Van den Brande, S. Lemey, J. Vanfleteren, and H. Rogier, "Highly Efficient Impulse-Radio Ultra-Wideband Cavity-Backed Slot Antenna in Stacked Air-Filled Substrate Integrated Waveguide Technology", *IEEE Transactions on Antennas and Propagation*, vol. 66, no. 5, pp. 2199–2209, 2018.

[26] D. Pozar, *Microwave Engineering*. Wiley, 2012, ch. 6.

[27] D. Pozar and S. Targonski, "Improved Coupling for Aperture Coupled Microstrip Antennas", English, *Electronics Letters*, vol. 27, 1129–1131(2), 13 1991.

[28] Q. Van den Brande, S. Lemey, J. Vanfleteren, and H. Rogier, "Highly Efficient Impulse-Radio Ultra-Wideband Cavity-Backed Slot Antenna in Stacked Air-Filled Substrate Integrated Waveguide Technology", *IEEE Transactions on Antennas and Propagation*, vol. 66, no. 5, pp. 2199–2209, 2018.

[29] R. Azim and M. T. Islam, *Printed Wide Slot Ultra-Wideband Antenna*. chapter, 2013, vol. 7.

[30] *Processing Procedures for BCB Adhesion*, CYCLOTENE Advanced Electronic Resins, DOW, Jun. 2007.

[31] *Processing Procedures for CYCLOTENE 3000 Series Resins*, CYCLOTENE Advanced Electronic Resins, DOW, Feb. 2005.

[32] *Photopolymer Negative Tone Photoresists*, AZ 125nXT Series, Microchemicals, Apr. 2016.

[33] *TI 35E*, Image Reversal Resist, Microchemicals, Aug. 2018.

7 Conclusions and future work

7.1 Conclusions

Similar to each industrial revolution throughout history, Industry 4.0 is expected to transform the factory of the future, ushering in an era of affordable hyper-personalization because of improved production transparency, productivity and efficiency. The combination of Internet-of-Things (IoT), Cyber-Physical System (CPS) and big data analytics are vital to the acceleration of this paradigm shift, facilitating high levels of virtualization, automation and production agility. In this context, next-generation wireless systems are considered key enablers for the smart factory, not only providing reconfigurable, low-latency, high-data-rate communication channels, but also highly accurate and robust location information. The use of Impulse Radio Ultra-Wideband (IR-UWB) Real-Time Locating System (RTLS) technology enables access to precise and reliable location data, while exhibiting high immunity to multipath effects and interference, commonly found in harsh Industry 4.0 environments. (Beyond) 5G multi-antenna systems are another key enabler for Industry 4.0, providing the reliable, low-latency and high capacity communication channels required for massive Machine-to-Machine (M2M) communication and interaction with large networks of CPS.

This Ph.D. dissertation focused on the development of highly efficient, Ultra-Wideband (UWB), Air-Filled Substrate-Integrated-Waveguide (AFSIW) antenna technology for robust and accurate IR-UWB RTLSs and high-data-rate (beyond) 5G applications. First, a modular and system-oriented full-wave/circuit co-optimization framework was proposed and validated with the development of highly-efficient and robust IR-UWB antennas, optimized for minimal orientation specific pulse distortion and ranging bias in realistic Industry 4.0 deployment scenarios. Second, highly-efficient and robust on-chip antenna technologies for (beyond) 5G multi-antenna systems were investigated, providing unprecedented efficiencies ($>$ 90%)

over a large impedance bandwidth within a compact antenna footprint.

In the first part of this dissertation, a novel approach was presented to develop low-cost, highly efficient IR-UWB antennas, optimized for precision indoor localization in Industry 4.0 environments. Leveraging a modular full-wave/circuit co-optimization framework, AFSIW technology and mode-bifurcation of resonant structures, resulted in robust IR-UWB antennas, exhibiting high antenna efficiencies over a large impedance bandwidth, a high System Fidelity Factor (SFF) and a minimized Distance Estimation Error (DEE). To demonstrate the potential of this approach, two novel antenna designs were proposed for indoor RTLS applications. First, a coupled half-mode cavity-backed slot AFSIW antenna was proposed, optimized for minimal pulse distortion within its Half-Power Beamwidth (HPBW). This design was fabricated using low-cost fabrication techniques, while providing robust and highly efficient antenna performance. Furthermore, a rigorous comparison was carried out to elucidate the advantages of AFSIW technology over Dielectric-Filled Substrate-Integrated-Waveguide (DFSIW) technology, both in the frequency and time-domain. Next, a coupled Planar Inverted-F Antenna (PIFA) topology was proposed as a novel sector antenna, optimized for minimal orientation specific ranging bias within its HPBW. The use of low-cost fabrication techniques and materials, while guaranteeing optimal antenna performance, demonstrates the enormous potential towards mass-deployment in Industry 4.0 applications.

In the second part, a novel AFSIW fabrication technology was proposed for low-cost, compact and highly-efficient UWB on-chip multi-antenna systems at Milimeter-Wave (mmWave) and Terahertz (THz) frequencies. Initially, a hybrid integration strategy was proposed, combining the merits of both Antenna-on-Chip (AoC) and Antenna-in-Package (AiP) technologies while mitigating their major drawbacks, being high substrate and interconnect losses, respectively. A cavity-backed stacked-patch antenna was realized on chip by suspending the stacked-patch elements, implemented on a high-frequency *RO*4350*B*® laminate, above a metalized air-filled cavity, which is micromachined into the bulk silicon substrate. In this approach, AFSIW technology and mode-bifurcation are leveraged to obtain highly efficient UWB operation within a compact footprint, especially suited for 5G multi-antenna systems. Furthermore, the microstrip feed on the antenna backside, exciting the patches through an aperture in the cavity, facilitates integration of active electronics on the chip to form a highly-integrated System-on-Chip (SoC). Next, the hybrid integration strategy was adapted to provide AFSIW technology at THz frequencies. A polymer-enabled AFSIW technology was proposed for highly-efficient, broadband on-chip THz multi-antenna systems. A thin, low-loss polymer superstrate, containing both the radiating elements and antenna feed, is suspended on top of an AFSIW cavity, similar to cavities in the mmWave design. This enables the realization of low-cost, yet highly-efficient UWB THz antennas. To demonstrate its exceptional performance, a cavity-backed slot antenna with exponentially tapered feed and modified slot was designed in both a stand-alone and 1x4 linear array configuration. Ultimately, the unit antenna element exhibited a significantly larger UWB

antenna efficiency than the state-of-the-art and grating-lobe free beam-steering capabilities up to 30° were demonstrated by the array. Furthermore, a mechanical and thermal analysis were performed to guarantee robust antenna operation.

7.2 Future work

Although the research presented in this dissertation shows great promise, many improvements and further developments can be made.

7.2.1 Robust and Highly-Efficient Antenna Systems for IR-UWB Localization in Industry 4.0 Applications

Significant advancements were generated in the field of IR-UWB antenna systems, relevant for both academia and industry. In particular, with the widespread industrial adoption of IR-UWB RTLSs, novel emerging technological concepts are being explored to enhance RTLS accuracy. In this context, multi-antenna IR-UWB systems are becoming an increasingly interesting research domain, providing opportunities to extract both location and angle-of-arrival information to further enhance localization accuracy or reduce IR-UWB RTLS infrastructure complexity. Furthermore, the application of beam-steering in multi-antenna IR-UWB systems proves promising, as it facilitates physical layer encryption to mitigate malicious sniffing attacks.

Additionally, Distributed Antenna Systems (DASs) can provide the required extreme high reliability of wireless links for automated and efficient decision making in the context of Industry 4.0. Hence, the possibility of IR-UWB DASs shows great promise in different application scenarios. Different deployment strategies can be explored, ranging from integration of DAS in mobile robotic platforms that require continuous real-time location information, to deploying a DAS in a certain sector, guaranteeing highly reliable service by a single Access Point (AP). However, the general trend to move IR-UWB RTLSs towards higher frequencies challenges the potential of the second deployment strategy as increased distribution losses limit the RTLS performance. Here, the emerging technology of IR-UWB over fiber shows great promise as optical fiber attenuation typically is in the order of magnitude of 1 dB/km. To this end, the concept of opto-electrical IR-UWB antennas deserves significant research attention.

7.2.2 Highly Efficient On-Chip Antenna Technology for 5G and beyond 5G Wireless Systems

In the context of 5G and beyond 5G, highly integrated SoC solutions provide an all-in-one solution that will accelerate the adoption of next-generation wireless systems. In this dissertation, the groundwork was laid out for a highly efficient SoC at both mmWave and THz frequencies. Further development of the hybrid

on-chip antenna is suggested, to include active electronics or photonic integrated circuits on the chip backside to create an active unit antenna element. Next, an active antenna array is to be developed, exhibiting beam-steering capabilities and demonstrating a high-data-rate wireless link in a lab environment.

In beyond 5G wireless systems, at THz frequencies, the developed polymer-enabled AFSIW technology for highly-efficient, broadband on-chip THz antenna systems shows immense potential. However, several improvements are still required to unlock its full capacity. First, the fabrication technology still requires slight optimization to enhance mechanical robustness and to facilitate three metal layers. To this end, different low-loss superstrate polymers, such as polyimide, can be explored to increase resilience against mechanical failure as a result of vibrations. Furthermore, different deposition techniques can be utilized to suspend the polymer superstrate above the AFSIW cavity. For example, developing the polymer superstrate on a glass substrate - instead of an InP wafer - would allow depositing metallic structures on one side of the superstrate while still facilitating accurate alignment with the chip. In this way, an extra metallic layer is obtained, thereby significantly increasing design flexibility.

Next, the development of efficient Uni-Traveling-Carrier Photodiodes (UTC-PDs) at THz frequencies has suddenly paved the way for high performance opto-electrical THz SoC solutions. Yet, a long road is ahead to realize a fully integrated SoC with beam-steering capabilities. To this end, the development of an opto-electrical on-chip antenna element, based on the research presented in Chapter 6, could be a potential break-through in the field of opto-electrical THz SoCs. In a first step, a discrete UTC-PD could be integrated on the standalone antenna, providing interconnection through carefully placed wirebonds. In a next step, the need for interconnects can be eliminated by directly integrating the UTC-PD onto the polymer superstrate by means of transfer printing.

Finally, this unit element can be used to construct an opto-electrical on-chip multi-antenna front-end, integrating an optical distribution network, UTC-PDs and optical true time delay units to demonstrate its beam-steering capabilities. Additionally, the system-level performance can be evaluated, pushing data rates above 100 Gbps.

Probed mmWave Antenna Impedance Measurement.